UNIVERSITY OF OKLAHOMA

GRADUATE COLLEGE

FABRICATION AND CHARACTERIZATION OF ORDERED ARRAYS OF NANOSTRUCTURES

A Dissertation

SUBMITTED TO THE GRADUATE FACULTY

in partial fulfillment of the requirements for the

degree of

Doctor of Philosophy

By

PRESTON LARSON

Norman, Oklahoma

2005

UMI Number: 3174404

UMI Microform 3174404

Copyright 2005 by ProQuest Information and Learning Company.
All rights reserved. This microform edition is protected against
unauthorized copying under Title 17, United States Code.

ProQuest Information and Learning Company
300 North Zeeb Road
P.O. Box 1346
Ann Arbor, MI 48106-1346

FABRICATION AND CHARACTERIZATION OF ORDERED ARRAYS

OF NANOSTRUCTURES

A Dissertation APPROVED FOR THE

DEPARTMENT OF PHYSICS AND ASTRONOMY

BY

____
Matthew Johnson (Chair)

____
Michael Santos

____
Kieran Mullen

____
Gregory Parker

____
Patrick McCann

© Copyright by Preston Larson 2005

All Rights Reserved.

Table of Contents

List of Tables……………………………………………………………………..x

List of Figures…………………………………………………………..……….……xi

Summary Abstract……………..…………………………………….……….......xxi

Chapter 1 Nanostructures…………………………………………………...1

1.1 Nanostructure Overview……………………………………………..1

1.2 Nanostructure Fabrication Techniques……………………………8

1.3 Thesis Overview……………………………………..……11

Chapter 2 Atomic Fluorine Beam Etching of Silicon and Related Materials…..16

2.1 Abstract…..…………………………………………..……16

2.2 Introduction…………………………………………………17

2.3 Experimental Details…………………………………….……18

2.4 Results………………………………………….....…..21

2.4.1 Bulk Etch Rates of Si and Related Materials………...21

2.4.2 Bulk-Etched Si Surface Topography………….……..23

2.4.3 Lithographically Patterned, Fluorine-Etched Si……..24

2.5 Discussion……………………………………………………..28

2.5.1 Bulk-Etched Si and Related Materials……………….28

2.5.2 Micron Scale, CaF_2-Masked Si Trenches……………29

2.5.3 Nano-Scale Si Trenches……………………………...35

2.6 Conclusion……………………………………………………36

Chapter 3 Anodic Aluminum Oxide Films……………………………38

3.1 Abstract……………………………………………………38

3.2 Background and Overview of AAO Films………………………39

3.3 Barrier-Type AAO Films……………………………………41

3.4 Porous-Type AAO Films……………………………………46

3.4.1 Structure and Composition…………………………46

3.4.2 Overview of Growth………………………………48

3.4.3 Field-Assisted Dissolution…………………………50

3.4.4 Pore Initiation…………………………………51

3.4.5 Pore Development………………………………53

3.4.6 Steady State Growth……………………………54

3.4.7 Ordered Growth…………………………………56

3.5 Experimental Results and Discussion…………………………60

3.5.1 Al Foil Pre-Treatment Study…………………………60

3.5.2 Porous AAO Film Results……………………………63

3.5.3 Low Temperature Porous AAO Film Results…………68

3.5.4 Evaporated Al on Si Porous AAO Results……………69

3.6 Conclusion……………………………………………………70

Chapter 4 Pattern Transfer with AAO Films: Nano-Dot Arrays…………72

4.1 Abstract……………………………………………………72

4.2 Pattern Transfer Technique…………………………………73

4.3 Thermally Evaporated Nano-Dot Arrays…………………………74

4.3.1 MgF_2 Nano-Dot Array using Oxalic Acid-Grown AAO Mask……………………………………..………..74

4.3.2 Other Examples of Thermally Evaporated Nano-Dot Arrays using Oxalic Acid-Grown AAO Masks……...78

4.3.3 Thermally Evaporated Nano-Dot Arrays using Sulfuric-Acid Grown AAO Masks………………………..…..81

4.4 Sputter Deposited Nano-Dot Arrays…………………………..83

4.5 UV-Vis Spectroscopy of Au Nano-Dot Arrays………………....85

4.5.1 Introduction………………………………..………85

4.5.2 Ordered and Unordered Au Nano-Dot Arrays……….85

4.5.3 Monodisperse Au Dots in Aqueous Solution………..87

4.5.4 MiePlot…………………………………….…………87

4.5.5 UV-Vis Spectroscopy………………..……………...88

4.5.6 Results and Discussion……………………………...89

4.6 Conclusion…………………………………………..……...92

Chapter 5 Pattern Transfer with AAO: Nano-Hole Arrays………………….…93

5.1 Abstract………………..……………………………………93

5.2 Ion Etched Nano-Hole Arrays…………………………………...94

5.3 Reactive Ion Beam Etched Nano-Hole Arrays…………………98

5.4 Atomic Fluorine Beam Etched Nano-Hole Arrays……………..100

5.4.1 Oxalic Acid-Grown AAO Masks………..…………100

5.4.2 Sulfuric Acid-Grown AAO Masks………………....102

5.4.3 Evaporated Al/Si AAO Masks…………………..….104

5.5 Conclusion……………………………..…………………107

Chapter 6 Fabrication and Characterization of Si Nano-Meshes……………...109

6.1 Abstract……..…………………………..………………109

6.2 Experimental Details……………………………..…..………110

6.3 Results and Discussion…………………….…..………………114

6.3.1 Electron Microscopy Results……………...……..114

6.3.2 Photoluminescence of Si Nano-meshes……………119

6.4 Conclusion…………………………………………...………123

6.5 Acknowledgments…………………………………………….123

Chapter 7 Fabrication and Characterization of Array of MOS-Type Nano-Capacitors……………………………………….……….…..…125

7.1 Abstract………………………………………………………125

7.2 Introduction……………………………...………….…..…125

7.3 Experimental Details………………………..……………..…127

7.4 Results and Discussion………………………………………129

7.5 Conclusion…………………………………………………...131

Chapter 8 Fabrication and Characterization of Nano-Ring Arrays…………..….133

8.1 Abstract………………………………………………………133

8.2 Introduction………………………………………………..…134

8.3 Experimental Details…………………………………………135

8.4 Results and Discussion……………………….…..…………138

8.4.1 Electron Microscopy Results……………...………..138

8.4.2 Magnetization Hysteresis Loops of Ni Nano-Ring and Nano-Dot Arrays……144

8.5 Conclusion……148

8.6 Acknowledgments……149

Appendix 1 Pattern Transfer with AAO: Nano-Pillar Arrays……150

A1.1 Abstract……150

A1.2 Experimental Details and Results……151

A1.2.1 GaAs Nano-Pillar Array……151

A1.2.2 Si Nano-Pillar Array……152

A1.3 Conclusion……154

Appendix 2 Carbon Nano-Tube Arrays……155

A2.1 Abstract……155

A2.2 Experimental Details and Results……156

A2.3 Conclusion……158

Appendix 3 Niobium Nano-Meshes……160

A3.1 Abstract……160

A3.2 Experimental Details……160

A3.3 Results……162

A3.4 Conclusion……163

Appendix 4 Malonic Acid-Grown AAO Films……164

A4.1 Abstract……164

A4.2 Experimental Details……165

A4.3 Results……167

A4.4 Conclusion……………………………………..…………………..171

Bibliography……………………………………………………….………..………174

List of Tables

Table 8.1 Summary of magnetization properties for the Ni nano-ring array, Ni nano-dot array and thin Ni film……………….………………………….…..……147

Table A4.1 Malonic acid-grown AAO sample growth conditions………...………….166

List of Figures

Figure 1.1 Spaceline showing the length scales associated with nano-scale structures, characterization, and technology……………………………………………….2

Figure 1.2 Surface-to-volume atomic ratio and the total number of atoms plotted as a function of cube side for Si(100) cubes……………………………………..3

Figure 1.3 Density of states for free electrons in a solid for bulk matter, one spatial dimension confined, two spatial dimensions confined, and three spatial dimensions confined…………………………………………………………….4

Figure 1.4 Bulk Fermi wavelength versus electron concentration……………………..6

Figure 1.5 Particle-in-a-box ground state energies as a function of cube length, *L*, for Si, GaAs, and InSb…………………………………………………………...7

Figure 1.6 Pattern generated using NSOM lithography on a-Si:H…………………………………………………………………………....9

Figure 2.1 Schematic of atomic fluorine beam etching apparatus……………………………………………………………………..19

Figure 2.2 (a) Etch depth vs. time for Si, Si_3N_4 and SiO_2 at T_{SUB}=120°C. Measured etch rates of resists at 200°C given in table (inset). (b) An Arrhenius plot showing silicon etch rate versus 1000/T_{SUB}……………………………………………………………….22

Figure 2.3 Top down and cross-sectional SEM views (inset) of unpatterned F-etched Si(100) at substrate temperatures of 227°C, 441°C, and 560°C……………………………………………………………..…..….24

Figure 2.4 (a) Cross-sectional SEM view of a 1 μm wide, 120 μm-deep, CaF_2-masked trench in Si(100). (b) Plot of the expected profile assuming a cosine distribution for reactive species scattered at the bottom of the trench (c) Top down SEM view of the trench and the CaF_2 mask……………………………….…………………………….……………25

Figure 2.5 Top down SEM view of fluorine etched trenches in Si fabricated using e-beam lithography on a 60-80 nm thick PMGI resist……………………………………………….……………..……..26

Figure 2.6 (a) Oblique angle SEM view of F-etched trench in Si fabricated using a double layer resist technique. (b) Cross-sectional SEM picture of a similar fluorine etched trench in Si………………………………………………………………...…………27

Figure 3.1 Simplified schematic of electrolytic cell used to produce barrier-type and porous-type alumina films...40

Figure 3.2 Schematic showing the ions involved in barrier-type oxide growth and the direction of the concentration gradients under an applied electric field…...42

Figure 3.3 Approximate potential energy curve of a mobile ion in aluminum oxide....43

Figure 3.4 Resulting potential energy curve upon application of an electric field across the oxide…………………………………………………………………....44

Figure 3.5 Schematic representation of ideal structure of porous alumina……………47

Figure 3.6 Voltage vs. time and current vs. time curves for anodizing at constant current density and constant voltage, respectively. The subsequent stages of pore growth are also shown……………………………………………..……49

Figure 3.7 Schematic representation of the field-assisted dissolution of Al_2O_3……………...…………………………………………………..……50

Figure 3.8 TEM images of porous AAO films grown at 50 Am^{-2} in 0.4 M phosphoric acid at 25°C showing initial pore initiation and development……………………………………………………...…...……51

Figure 3.9 Schematic diagrams showing the non-uniform thickening of the barrier oxide and eventual development of major pores……………………….….52

Figure 3.10 Schematic representation showing the distribution of field lines in porous AAO….……………………………………………………………….55

Figure 3.11 The theoretical dependence of cell size versus applied voltage (straight line) compared with experimental data with different electrolytes……………………………………………..…………..56

Figure 3.12 SEM micrographs of unordered and ordered porous alumina films formed in 0.3 M phosphoric acid at 0 ^{o}C for 16 hours.…………………………………………………………………57

Figure 3.13 Expansion of Al during anodic oxidation………………………………….58

Figure 3.14 Nomarski optical microscope and SEM images of pre-anodized Al foils…………………….…………………………………………………..61

Figure 3.15 Process schematic for fabricating a well-ordered AAO film…………………….……………………………………………………...62

Figure 3.16 Nomarski optical microscope and SEM images of porous AAO films after first and second anodizations..……………………………………………………….……...63

Figure 3.17 Typical current vs. time curve for a porous AAO film anodized at a constant voltage of 40 V for roughly 20 hours at 5 ^{o}C………………………………...………………………………..64

Figure 3.18 SEM micrographs of porous AAO films anodized at 40V in 0.3 M oxalic acid at 5 ^{o}C and at 27 V in 1.7 wt % sulfuric acid at 5 ^{o}C…………………………………………………………….………...64

Figure 3.19 Interpore distance versus applied voltage for porous AAO films grown in sulfuric acid, oxalic acid, and phosphoric acid electrolytes. Inset table shows the pore diameters and interpore separations for the three electrolytes under the conditions that maximizes the ordering of the pores………..…..65

Figure 3.20 Near cross-sectional SEM image of oxalic acid-grown AAO film removed from the Al foil and lifted out onto a silicon substrate. Inset shows a higher magnification cross-sectional SEM image of the barrier layer…………..……66

Figure 3.21 1 μm x 1 μm, 3D-rendered AFM images of an oxalic acid-grown AAO film porous side up (a), and barrier layer side up (b)……………………………………… ……………………….………....66

Figure 3.22 AAO film thickness vs. secondary anodization time for films grown in 0.3 M oxalic acid at 40 V and 2 ^{o}C. Images on the right show oblique angle SEM micrographs of AAO films grown for 1 minute, 5 minutes, and 8 minutes………………………………………………………………………..67

Figure 3.23 Porous AAO film grown in a 1:1 mixture of 1.2 M sulfuric acid: MeOH at 15V and -32 ^{o}C…………………………………………………………………..…68

Figure 3.24 SEM images of porous AAO film anodized from thermally evaporated Al/Si……………………………………...…………………………...…69

Figure 4.1 Process schematic for fabricating a through-hole porous AAO mask……………………………………………………………….…….73

Figure 4.2 Top down SEM micrographs of array of MgF_2 nano-dots thermally evaporated through a porous AAO mask onto a Si substrate……………….………………………………………...………76

Figure 4.3 3D rendered AFM image and line scan showing hexagonal array of thermally evaporated MgF_2 nano-dots.……………………………………...……………………………77

Figure 4.4 Top down SEM micrographs of array of Au nano-dots thermally evaporated through a porous AAO mask onto a Si substrate……………………………………………………………………78

Figure 4.5 Oblique angle SEM micrograph of Au nano-dot array thermally evaporated through a porous AAO mask onto a Si substrate……………..…………...78

Figure 4.6 Oblique angle SEM micrographs of Ni dot arrays evaporated through an AAO mask illustrating dot height and shape differences controlled through the amount of evaporation……………….………………………….………..79

Figure 4.7 SEM micrographs of Ni nano-dot array after removal of AAO mask and after an O_2 plasma etching step to remove organic materials……………………………………………..….…………80

Figure 4.8 SEM micrographs of array of Ni dots thermally evaporated onto a Si substrate through a sulfuric acid-grown AAO mask with 20 nm pore diameters spaced 60 nm apart……………………………………………………………………..82

Figure 4.9 AFM images of MgF_2 nano-dot array thermally evaporated through a sulfuric acid-grown AAO mask……………………………..…………………………….……...83

Figure 4.10 AFM image of Mo dots sputtered through an oxalic acid-grown AAO mask onto a Si substrate……..………………...…………………………….……...84

Figure 4.11 Top down SEM micrographs of ordered and unordered AAO films and Au dot arrays……………………………………………………………….………..86

Figure 4.12 (a) UV-Vis spectrum of ordered and unordered Au nano-dot array. (b) MiePlot theoretical results of Au dots of varying diameters in a fused silica environment. (c) UV-Vis spectrum of 14 and 76 nm diameter Au dots in an aqueous solution………………………………………………………….…..90

Figure 5.1 SEM micrographs of nano-hole array in GaAs fabricated by Ar^+ ion etching through a porous AAO mask.…………………………………..……………………….………..95

Figure 5.2 SEM micrographs of nano-hole array in Si and InSb fabricated by Ar^+ ion etching through an oxalic acid-grown AAO mask……………………………………………………………………..97

Figure 5.3 SEM micrographs of GaAs nano-hole array fabricated by RIBE through an oxalic acid-grown AAO mask……………………………………………………………………..99

Figure 5.4 SEM micrographs of nano-hole arrays in Si(100) and Si(111) fabricated by fluorine etching through an oxalic acid-grown AAO mask………………………….……………………………………….………..101

Figure 5.5 SEM micrographs of nano-hole arrays in Si(100) and Si(111) fabricated by fluorine etching through a sulfuric acid-grown AAO mask………………………….…………………………………….……..103

Figure 5.6 SEM micrographs of fluorine etched nano-hole array in Si(100) fabricated using an AAO mask grown directly onto Si…………………………….………………………………………………106

Figure 6.1 Schematic showing sample processing steps to fabricate a free-standing Si nano-mesh encased in SiO_2…...………………………………………………………….....111

Figure 6.2 SEM micrographs of fluorine etched and Ar^+ etched nano-hole arrays in SOI substrates…………………….………………………………….…...115

Figure 6.3 SEI and TEI images of free-standing unoxidized and oxidized Ar^+ ion etched Si nano-meshes..……………………………………………………….…………..116

Figure 6.4 Bright field TEM images of free-standing, unoxidized and oxidized Ar^+ etched Si nano-meshes…..…………………………………………….117

Figure 6.5 High resolution TEM images of free-standing, unoxidized and oxidized Ar^+ etched Si nano-meshes near a single nano-hole……………………..…………………………….…………118

Figure 6.6 (a) TEM image of oxidized Si nano-mesh indicating where CBED took place. (b) Typical CBED pattern used to calculate the thickness of the oxide encased Si wire mesh……………………………………….…….……119

Figure 6.7 Photoluminescence spectra taken at 77K of: (a) oxidized, fluorine etched Si nano-mesh (b) oxidized, Ar^+ etched Si nano-mesh (c) Un-oxidized, fluorine etched Si nano-mesh (d) oxidized SOI substrate and (e) SOI substrate……………………………………………………………..121

Figure 7.1 Cross-sectional schematic of processing steps used to fabricate MOS-type nano-capacitors……………………………………..……………128

Figure 7.2 SEM micrographs of nano-hole array in SiO_2/Si_3N_4/on Si…….……………………………………………………...……129

Figure 7.3 Room temperature Capacitance-Voltage curves taken at 100 kHz using the electrolyte contacting technique.………...…………………………….……130

Figure 8.1 Schematic views of processing steps used to fabricate nano-ring arrays using Method I and Method II……………………………………………..135

Figure 8.2 Electron microscopy results for Si nano-rings fabricated using Method I………………………………………………….……..…………139

Figure 8.3 SEM micrograph of Ni rings on SiO_2/Si substrate fabricated using Method I. Inset is a 45° oblique view showing the 50 nm tall rings……...…………………………………………….…………139

Figure 8.4 Electron microscopy results for Ni rings fabricated using Method II……………..……………………………………………………….140

Figure 8.5 Electron microscopy results for Au rings fabricated using Method II…………………………………..…………………………………141

Figure 8.6 SEM micrograph of Au nano-ring array fabricated in an AAO film on an Al foil…………………………………………………………………...142

Figure 8.7 SEM micrographs of (a) Ni nano-ring sample that magnetization hysteresis loops were obtained on. (b) Ni nano-dot sample that magnetization hysteresis loops were obtained on……………………………..……………………………...…145

Figure 8.8 Magnetization hysteresis loops for a Ni nano-ring array on Si, a Ni nano-dot array on Si, and a thin Ni film on Si……………………………………...146

Figure A1.1 SEM micrographs of GaAs nano-pillar array……………….……………………………………………...151

Figure A1.2 Cross-sectional schematic of processing steps used to fabricated Si nano-pillar array………………..……………………………………………….152

Figure A1.3 SEM micrographs of Si nano-pillar array.……………….………………153

Figure A2.1 SEM micrographs of a carbon nanotube array on an SiO_2/Si substrate grown using AAO pattern transfer methods and cobalt nano-particle catalysts……………………...………………………………………157

Figure A3.1 SEM micrographs of a Nb nano-mesh fabricated by sputter deposition of Nb directly onto an AAO film…………..…………………………………...161

Figure A3.2 (a) Magnetic scanning SQUID microscope image of Nb nano-mesh sample. (b) Susceptibility scanning SQUID microscope image of Nb nano-mesh sample……………………………………………………………….162

Figure A4.1 Schematic illustrating TEM sample preparation steps for malonic acid-grown AAO films………………………………………………………………….167

Figure A4.2 TEM images of an oxalic acid-grown AAO film and malonic acid-grown AAO films grown at different voltages…………………………..…………………………………….168

Figure A4.3 SEM images of an oxalic acid-grown AAO film and malonic acid-grown AAO films…………………………………………………………...………….169

Figure A4.4 (a) Average interpore spacing versus the anodization voltage for the malonic acid-grown films (b) Average pore diameters taken from the TEM images and SEM images as a function of the anodization voltage…………………………………………………..………………170

Figure A4.5 Auto-correlation images of the oxalic acid-grown AAO film and malonic acid-grown AAO films grown at different voltages…………………...……………..…………………………………...171

Figure A4.6 Radial distribution function for the oxalic acid-grown AAO film and the malonic acid-grown AAO films…………………………………………172

SUMMARY ABSTRACT

Nanostructures are currently of great interest because of their unique properties and potential applications in a wide range of areas such as opto-electronic and bio-medical devices. Current research in nanotechnology involves fabrication and characterization of these structures, as well as theoretical and experimental studies to explore their unique and novel properties. Not only do nanostructures have the potential to be both evolutionary (state-of-the-art ICs have more and more features on the nanoscale) but revolutionary (quantum computing) as well.

In this thesis, a combination of bottom-up and top-down approaches is explored to fabricate ordered arrays of nanostrucutures. The bottom-up approach involves the growth of self-organized porous anodic aluminum oxide (AAO) films. AAO films consist of a well ordered hexagonal array of close-packed pores with diameters and spacings ranging from around 5 to 500 nm. Via a top-down approach, these AAO films are then used as masks or templates to fabricate ordered arrays of nanostructures (*i.e.* dots, holes, meshes, pillars, rings, etc.) of various materials using conventional deposition and/or etching techniques. Using AAO films as masks allows a simple and economical method to fabricate arrays of structures with nano-scale dimensions. Furthermore, they allow the fabrication of large areas (many millimeters on a side) of highly uniform and well-ordered arrays of nanostructures, a crucial requirement for most characterization techniques and applications. Characterization of these nanostructures using various techniques (electron microscopy, atomic force microscopy, UV-Vis absorption

spectroscopy, photoluminescence, capacitance-voltage measurements, magnetization hysteresis curves, etc.) will be presented. Finally, these structures provide a unique opportunity to determine the single and collective properties of nanostructure arrays and will have various future applications including but not limited to: data storage, light emitting or sensing devices, nano-tribological coatings for surfaces, bio-sensors, filters, and more.

Chapter 1

Nanostructures

1.1. NANOSTRUCTURE OVERVIEW

Since Richard Feynmann's famous 1959 lecture [1] in which he described his vision of building and controlling matter from the bottom up utilizing atoms and molecules as the basic building blocks, scientists have pursued the goal of manipulating matter on the atomic and molecular scales. This emerging area of study, termed nanotechnology, involves the fabrication, characterization, and study of the behavior of nano-scale materials. These nano-scale materials or nanostructures are loosely defined as materials with *at least* one dimension on the order of 1-100 nm and are of great interest because of their potential use in many diverse fields ranging from opto-electronic devices to bio-medical applications. In addition, they are of fundamental physical interest since they lie in a size regime between that of bulk material and molecular-sized material. In this size regime, nano-materials behave differently from either their bulk or molecular counterparts. Current research in this area is seeking to understand and exploit the

electronic, magnetic, optical, thermal, and mechanical properties of such structures and devices.

Figure 1.1 shows the size scales involved in the materials, characterization techniques, and technologies in this area of research. For comparison, common biological materials and their characteristic sizes are also shown. For instance a blood cell with a typical size of a few microns is rather large compared to a typical virus (~75 nm) or to the diameter of a DNA helix (~ 2nm), both of which qualify as biological nanostructures.

The benefits of using nanostructured materials rather than their bulk counterparts for a variety of applications are numerous. In some cases, improvements are obtained simply by fabricating smaller devices than previous versions. As an example, the

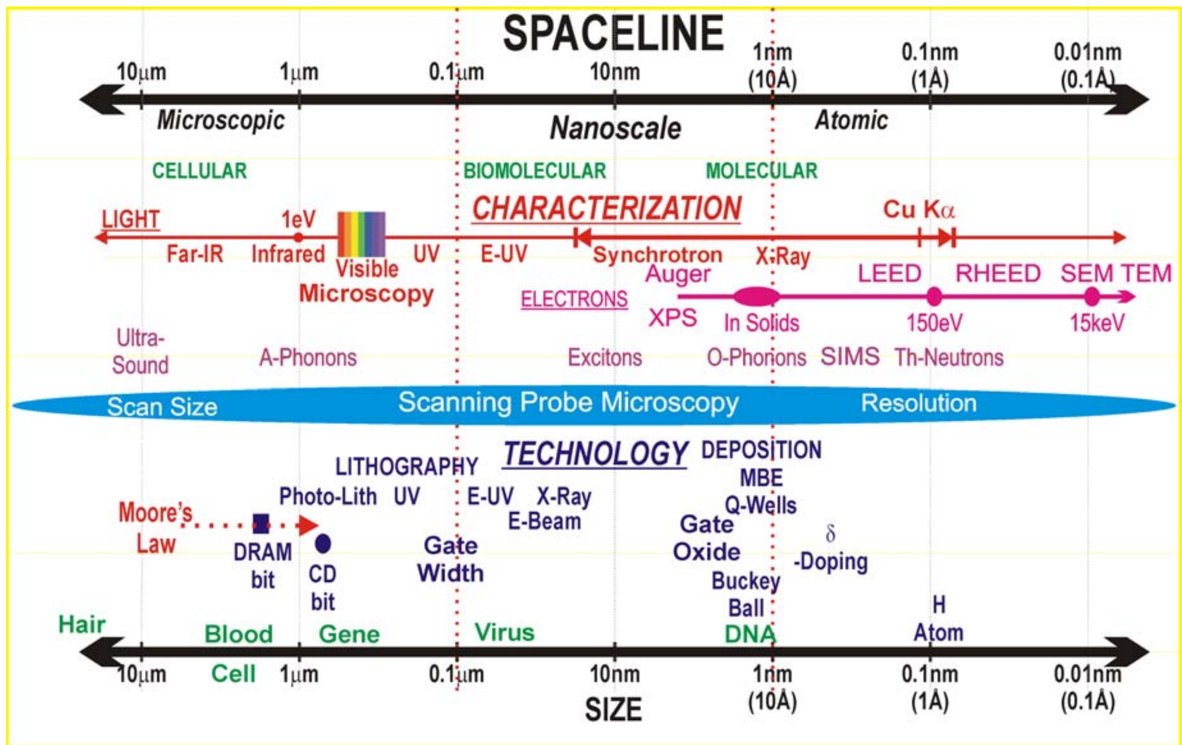

Figure 1.1. Spaceline showing the length scales associated with nano-scale structures, characterization, and technology.

ongoing trend in reducing the size of transistors (the basic operating elements in current generation integrated circuits), allows faster processing speeds, lower operating powers, and higher transistor densities (*i.e.* more memory per unit area), while still being firmly based in macroscopic classical physics. However, the benefits of using nanostructures in most applications is not in simply being small, but in the new intrinsic, and potentially advantageous properties such materials should exhibit as compared to their bulk counterparts. Unlike bulk material, the properties of nanostructured materials depend critically on the number of atoms, *N*, in the system. Properties such as atomic ionization potentials, chemical reactivities, magnetic moments, polarizabilities, and geometric structures depend critically on the number *N*, thereby opening up a whole new area of study where material properties can be engineered simply by controlling this parameter. Another important property that changes as *N* gets smaller is the surface-to-volume ratio of these nanostructures making the surface and interface properties of such materials critical. High surface area materials which can consist of either highly porous materials or solutions of small nanoparticles have emerging applications including but not

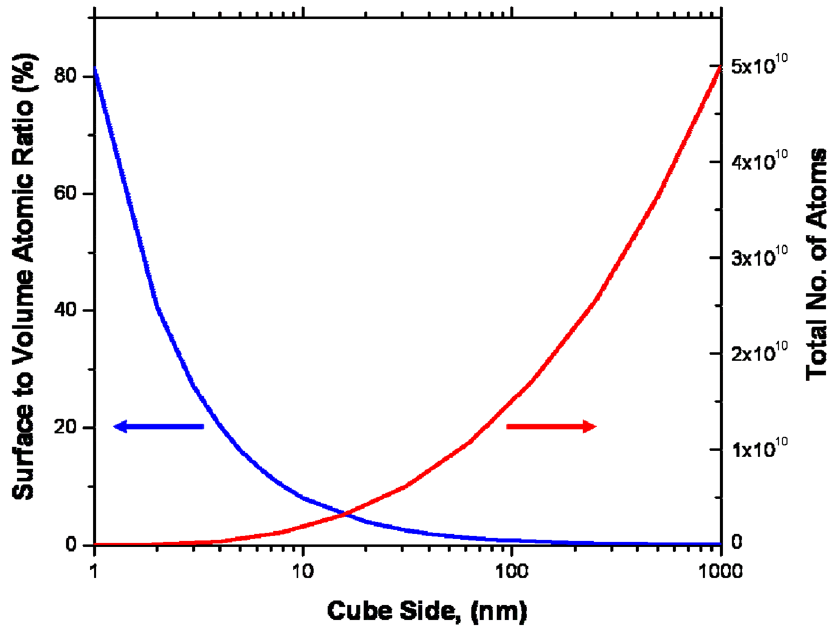

Figure 1.2. Surface-to-volume atomic ratio (blue) and the total number of atoms (red) plotted as a function of cube side for Si(100) cubes.

limited to: energy storage, battery/capacitor elements, gas separation and filtering, and bio-chemical separations [2]. To illustrate the importance of surface area properties in nanostructures, Figure 1.2 shows a plot of the surface-to-volume atomic ratios and the total number of atoms for increasingly smaller silicon cubes with (100)-directed faces. For a relatively large $(1\mu m)^3$ silicon cube only about 0.1% of the atoms lie on the surface but for a much smaller $(2\ nm)^3$ silicon cube, nearly half of the atoms (~40%) lie on the surface. At these scales, surface tension, strain, and thermal stability are all critical issues in these systems.

As alluded to above, nanostructures also lie in a regime where fundamental physics relations change from classical to quantum mechanical allowing new and interesting phenomena to take place (*e.g.* tunneling, quantum interference effects, *etc.*) For instance, confining electrons in solids to small length scales causes the continuous bulk energy bands to quantize into discrete levels. To illustrate this, Figure 1.3 shows

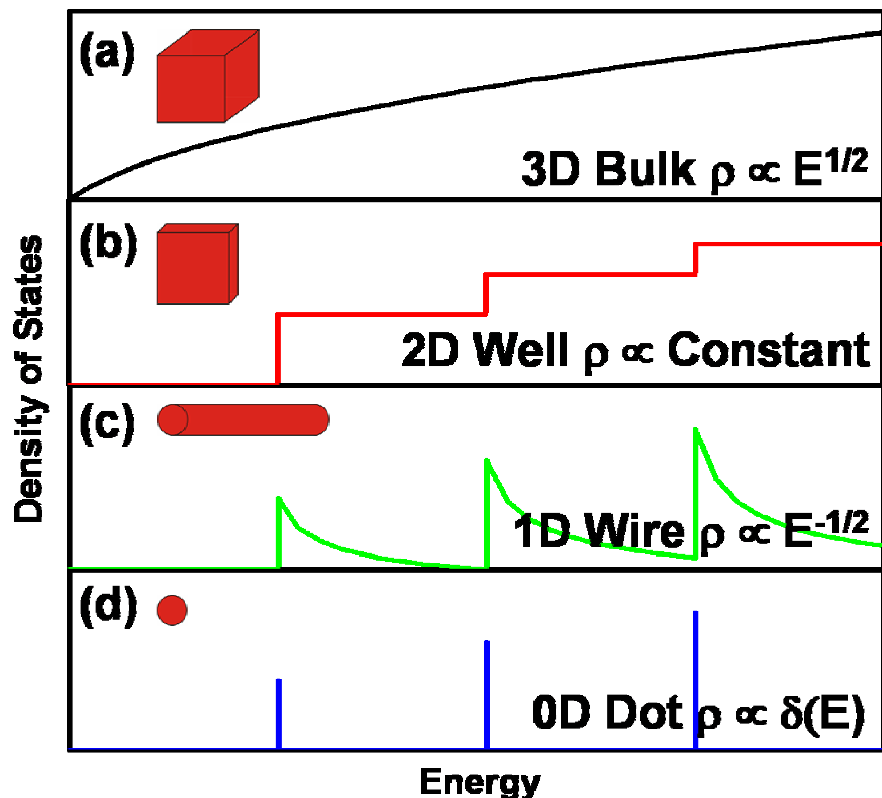

Figure 1.3. Density of states for free electrons in a solid for: (a) bulk matter (b) one spatial dimension confined (c) two spatial dimensions confined and (d) three spatial dimensions confined.

the density of states of a free electron Fermi gas for no spatial dimensions confined (3D or bulk material), one spatial dimension confined (2D or quantum wells), two spatial dimensions confined (1D or quantum wires), and three spatial dimensions confined (0D or quantum dots). For bulk materials, the density of states consists of a continuous band whereas 0D structures (often called artificial atoms) have a discrete energy spectrum much like atomic or molecular energy levels. By reducing the dimensionality of various materials, certain properties of devices become more advantageous. For example, reduced dimensionality lasers are more efficient than their bulk counterparts having lower current thresholds, less broadening, and reduced temperature sensitivities due to the more discrete density of states. In addition, the use of discrete transition energy levels dependent on the size of the structure (e.g. quantum well thickness) allows a means to tailor the output wavelength of such reduced dimensionality lasers.

At this point it becomes useful to pose the question, "How small does a structure need to be before it starts exhibiting quantum mechanical behavior?" The answer to this question is not universal and depends on the system and material properties. As a rule of thumb, electronic quantum mechanical effects start to become observable when the wavelength of the electron is comparable to the size of at least one confined dimension in the structure. In solid state systems, this corresponds to the Fermi wavelength which is dependent on the "free" electron density in the material. In most metals, the electron density is very large ($>10^{21}$ cm^{-3}) and the value of the Fermi wavelength for most metals consequently lies in the range of a few nanometers. However, in semiconductors, the much lower carrier density can give Fermi wavelengths of several tens to hundreds of nanometers. This length scale is accessible using conventional growth and patterning

techniques and makes semiconductors an attractive material to observe quantum mechanical effects since relatively larger structures can be used. In addition, carrier densities in

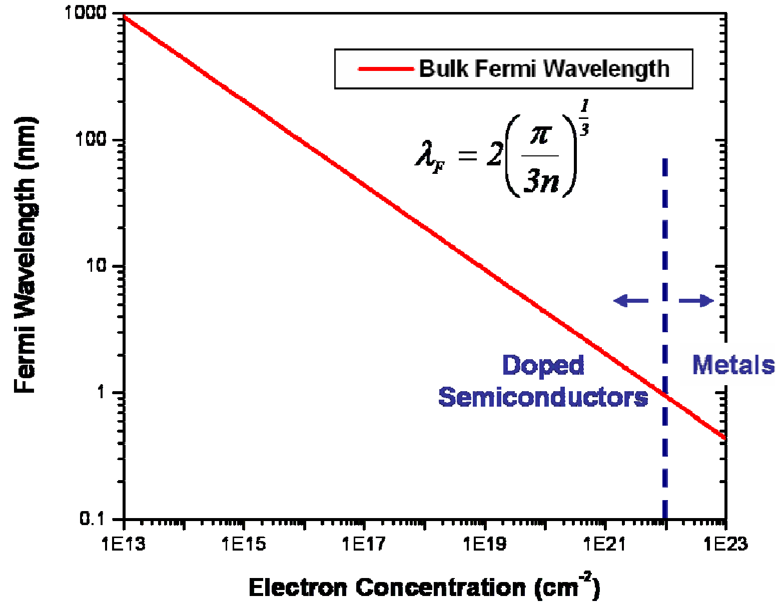

Figure 1.4. Bulk Fermi wavelength versus electron concentration.

semiconductors are adjustable via the doping of impurities and gating techniques making semiconductors a versatile material for both research and device structures. Figure 1.4 shows a plot of the free electron Fermi wavelength as a function of carrier density for bulk materials over a range including low to highly doped semiconductors (< 10^{22} cm^{-3}) and metals (> 10^{22} cm^{-3}). Note that since the Fermi wavelength depends solely on the carrier density (not the effective masses, *etc.*) it is largely independent of the semiconductor material (neglecting band structure by assuming free electrons) and is the same for silicon, gallium arsenide, indium antimonide, *etc.* at similar doping densities. However, in order to observe quantum mechanical effects in these materials, the discrete energy levels, which are size and material dependent, must be comparable to the thermal energy of the electrons so as not to be washed out. Other factors such as the mean free path of the electrons (temperature and material dependent) also need to be considered.

This leads to further criteria for approximating the length scales that need to be approached for the onset of quantum mechanical effects by comparing the low dimensional quantized energy levels of confined electrons with the thermal energy of such electrons. A rough approximation can be made by assuming a small cubic nanostructure. In this case, the well known quantum mechanical "particle-in-a-box states" for infinite potential barriers can be applied. Figure 1.5 compares the ground state energy levels of a confined electron in a box as a function of cube size ($L_x = L_y = L_z = L$) for silicon, gallium arsenide, and indium antimonide. The black horizontal lines at 26, 6.6, and 0.36 meV are the thermal energies of the electron at 300 (room temperature), 77 (liquid nitrogen), and 4.2 K (liquid helium), respectively. From the figure, it can be seen that InSb allows the largest cube size that will exhibit quantum mechanical effects at a given temperature due to its small effective mass. For example, the ground state energy of an InSb cube with sides of 50 nm is approximately equal to the

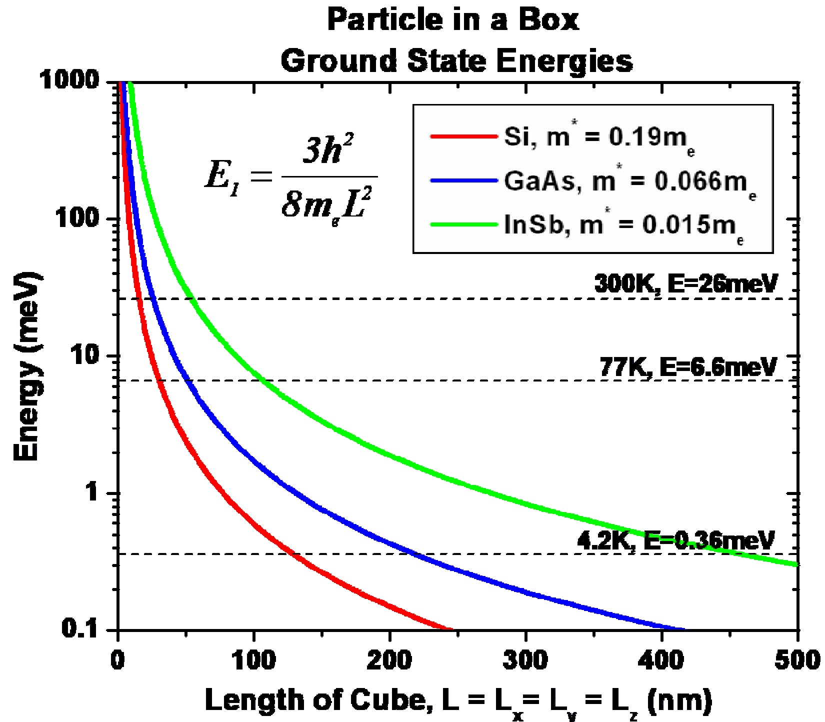

Figure 1.5. Particle-in-a-box ground state energies as a function of cube length, $L = L_x = L_y = L_z$, for silicon, gallium arsenide, and indium antimonide. The black horizontal dashed lines indicate the thermal energies at 300K, 77K, and 4.2 K.

room temperature thermal energy of 26 meV. An InSb cube with a ground state energy of twice the thermal energy (~52 meV) would need to be around 38 nm on a side. For comparison, quantum mechanical effects for silicon should be observable at room temperature for a cube 10 nm on a side which has a ground state energy of 59 meV (calculated using the transverse effective mass, $m_t = 0.19m_e$ for silicon), more than double the 26 meV thermal energy. This is certainly in good agreement with experimental and more involved theoretical results obtained for porous silicon samples which consist of a porous network or grid of silicon with dimensions in the sub-10 nm regime dependent [3, 4]. Unlike bulk silicon with its indirect bandgap, porous silicon exhibits visible photoluminescence whose central emission wavelength is size dependent. Debate continues to center on whether the observed photoluminescence is a result of quantum confinement effects due to the reduced size of the silicon or to high surface area interfacial properties [4, 5].

1.2. NANOSTRUCTURE FABRICATION TECHNIQUES

To date, the fabrication of materials on the nanoscale has focused on two basic approaches:

The "top-down" approach in which nanostructures are formed from bulk material by lithography, growth, etching, and related techniques; or the "bottom-up" approach in which nanostructures are built up from the individual atoms or molecules by self-organization of materials, electrochemical methods, or chemical synthesis.

The top-down approach has conventionally used techniques such as e-beam or photolithography combined with dry or wet etching and deposition techniques such as thermal evaporation, e-beam evaporation, sputtering, and molecular beam epitaxy (MBE). At present, the top-down approach is more developed than the bottom-up approach and is most notably used in the fabrication of current integrated circuits. An example of a more exotic top-down technique for patterning structures is shown in Figure 1.6. This approach, termed near field scanning optical microscopy (NSOM) lithography, was demonstrated by Dr. Reuben Collin's group at the Colorado School of Mines and imaged by the author using atomic force microscopy (AFM) [6]. In brief, a tapered fiber optic tip was dithered a few nanometers above the surface of amorphous hydrogenated silicon (a-Si:H) film resulting in the oxidation of the surface and hence generating an oxidized pattern wherever the tip was rastered. After patterning with the NSOM, the samples were exposed to a hydrogen plasma etch with a high etch selectivity between oxidized and hydrogen terminated silicon allowing the pattern to be "developed".

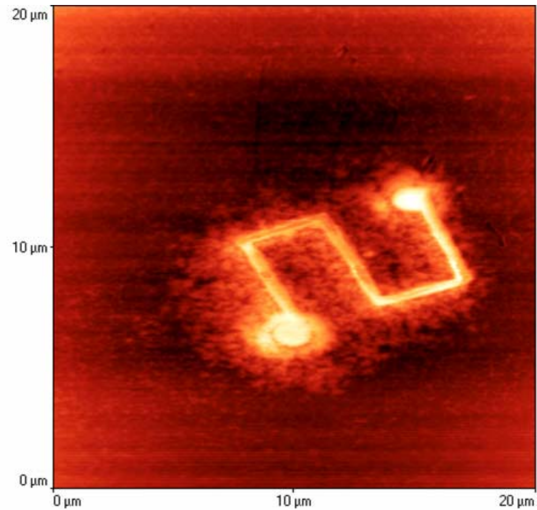

Figure 1.6. Pattern generated using NSOM lithography on a-Si:H film and developed using a hydrogen plasma etch. The pattern has linewidths of approximately 320 nm wide and 45 nm tall.

Although this technique and the other more mature technologies mentioned above are currently used for both commercial and research purposes, they suffer from several disadvantages that prevents them from being useful for the fabrication of smaller

nanostructures. One disadvantage of the top down approach is the limitation on the size of the material that can be constructed versus the processing time required to fabricate large patterns or arrays. For instance, e-beam and STM lithography can approach structures below 10 nm in size but these techniques are serial requiring large amounts of time to fabricate large arrays or patterns. Conversely, photolithography (a parallel technique) can fabricate patterns and arrays over a large area quickly, but the size of the structures, limited by the wavelength of light, currently only approaches around 65 nm using sophisticated resolution enhancement techniques such as phase-shifting lithography, *etc.*

Towards this end, recent work and research has focused on bottom-up techniques as a means to obtain well-ordered, smaller structures with less processing times. One such bottom up technique, the template method, seeks to take advantage of nano-porous materials, which are utilized as masks or templates to seed either a growth or etching type process [7]. To date, most of the work in this area has used one of two types of porous membranes as a template: track-etch polymeric membranes and anodic aluminum oxide (AAO) films. Porous membranes fabricated by the track-etch method are prepared by bombarding of film of nonporous polymeric material with nuclear fission fragments. This creates damage tracks in the material which are then chemically etched into pores. The resulting material consists of randomly distributed cylindrical pores of uniform diameter anywhere from a few microns down to 10 nm. Conversely, AAO films, often called porous alumina, are formed by anodizing an aluminum foil in an electrolytic cell. The resulting material consists of cylindrical pores surrounded by an aluminum oxide backbone. The pore diameters are tunable anywhere from 5 nm to 500 nm depending on

the applied voltage, and in addition, it has recently been discovered that under the appropriate anodizing conditions, the pores self order into a hexagonal close packed array. Of these two membranes, AAO films have a distinct advantage over track-etch membranes for use in lithography or pattern transfer applications due in large part because AAO films have more stable chemical and mechanical properties, are easier and cheaper to fabricate, and can have very well-ordered arrays.

For these reasons, the bulk of this thesis will focus on the fabrication and characterization of well-ordered arrays of nanostructures (dots, holes, rings, and pillars) fabricated using AAO films. The following section describes the organization of this thesis.

1.3. THESIS OVERVIEW

The chapter progression of this thesis is based partially on a historical approach (*i.e.* in the order that the work was done) while maintaining some sense of logical flow. The remainder of this thesis is composed as follows:

2: Atomic Fluorine Beam Etching of Silicon and Related Materials

Here a novel atomic fluorine beam technique is used to etch Si-related materials and potential mask materials. Temperature dependent bulk etch rates were determined and show an Arrhenius-type behavior with the substrate temperature. Using a CaF_2 mask, record high aspect ratio trenches (1 μm wide by 120 μm deep) were fabricated in Si. Unfortunately, this project was discontinued because our collaborator, Dr. Keil, did not remain at OU and initial work at reproducing high aspect ratio trenches on the

nanoscale proved problematic. Finally, work on fluorine beam etching through AAO films was carried out and is discussed in Chapters 5 and 6.

3: Anodic Aluminum Oxide Films

This chapter is intended as a guide for future experimentalists on the growth and fabrication of AAO films specifically for use as templates or masks. To start, a historical review of AAO films is presented discussing details of the growth mechanism. It is interesting to note that the growth and ordering mechanisms of porous AAO films is, at present, still not fully understood. The next part of this chapter presents work on optimizing the growth of AAO films specifically for use as templates or masks for the fabrication of arrays of nanostructures (i.e. tailoring the pore dimensions, spacings, AAO thickness, *etc.*).

4: Pattern Transfer with AAO Films: Nano-Dot Arrays

Here work on the fabrication of nano-dot arrays of various materials by evaporating or sputtering material through AAO films is presented. UV-Vis absorption spectroscopy of 50 nm diameter Au nano-dots, fabricated in this manner, show peaks qualitatively consistent with Mie scattering and absorption phenomena for Au nano-dots of this size.

5: Pattern Transfer with AAO Films: Nano-Hole Arrays

Nano-hole arrays fabricated by dry etching through AAO films into underlying substrates (Si, GaAs, and InSb) are discussed. In particular, results are shown for Ar^+ ion etching, chlorine-based reactive ion beam etching, and neutral atomic fluorine beam etching. All three etching techniques show characteristic nano-hole geometries and profiles.

6: <u>Fabrication and Characterization of Si Nano-Meshes</u>

Characterization of free-standing silicon nano-meshes fabricated using a combination of photolithography, wet-anisotropic etching, AAO films, and dry etching techniques are discussed. These Si nano-meshes were further downshifted in size by the use of a pattern dependent and self-limiting oxidation step, which oxidizes the outer Si matrix, leaving behind sub-15nm silicon cores. Photoluminescence (PL) spectra taken on these structures at 77 K reveal broad peaks in the 600-1000 nm wavelength range, possibly indicative of quantum confinement effects in the nanostructured Si.

7: <u>Fabrication and Characterization of Array of MOS-Type Nano-Capacitors</u>

Capacitance-voltage (*C-V*) characterization of a nano-array of metal-oxide-semiconductor (MOS) capacitors in Si is discussed. The nano-capacitor array was fabricated using AAO masks, etching techniques, and oxide growth in collaboration with researchers at the University of North Carolina. The conducting contact is achieved by using either poly-silicon or an electrolyte. In both cases, room temperature C-V measurements indicated little leakage. In the electrolyte case, capacitance values indicate only the thin gate oxide at the bottom of the nano-holes contributes to this capacitance.

8: <u>Fabrication and Characterization of Nano-Ring Arrays</u>

In this chapter, the fabrication and characterization of ordered arrays of Au, Ni and Si nano-rings fabricated using Ar^{+} sputtering and AAO templates is described. Two methods are presented, both relying on the re-deposition of sputtered material inside the pores of an AAO mask. Ring diameter, height, and spacing are controllable by varying the process conditions. In addition, magnetization hysteresis curves were taken on a Ni nano-ring array and compared with a Ni nano-dot array and a bulk thin film Ni layer.

This is followed by four appendices detailing related projects that were undertaken during the course of this research. These were not included in the main section of the thesis because they are either still ongoing or are not directly related to the main topic of this thesis. The appendices include:

A1: Pattern Transfer with AAO: Nano-Pillar Arrays

This appendix describes work performed in fabricating nano-pillar arrays using AAO masks to define an array of dots that was subsequently used as a mask for a dry etching process. Two related methods are described and results from each are shown.

A2: Pattern Transfer with AAO: Carbon Nano-Tube Arrays

This appendix describes work on fabricating a carbon nanotube array upright on a SiO_2/Si substrate by using an AAO template to seed an array of cobalt catalysts for a carbon nanotube growth step. The resulting nanotubes were not as well ordered as the initial AAO templates most likely due to catalyst migration under the high temperature growth step.

A3: Niobium Nano-Meshes

This appendix describes work on Nb nano-meshes fabricated by Nb sputter deposition directly onto AAO films. Preliminary characterization of these films using a scanning superconducting quantum interference device (SQUID) microscope shows the presence of vortices and indicates that the nano-meshes are superconducting. Future work will involve characterization of these films by magnetization/susceptibility measurements as well as with a low temperature scanning magnetic force microscope with a spatial resolution comparable to the 50 nm hole diameters in these nano-meshes to

determine the location of the vortices when the magnetic field is commensurate with the diameter of the nano-holes.

A4: Malonic Acid-Grown AAO Films

This appendix describes work on the growth of porous AAO films using malonic acid-based electrolytes. Electron microscopy techniques were used to determine the dependence of the pore diameters and spacings on the growth conditions and to confirm that malonic acid-grown AAO films follow the same growth mechanism as other porous AAO films. In addition, a preliminary study was conducted to determine the feasibility of finding appropriate growth conditions for the self-ordering of the pores into a hexagonal close-packed array. This initial study proved inconclusive but suggests that malonic acid-grown films may self-order into a hexagonally close-packed array at higher anodization voltages than presented here.

Chapter 2

Atomic Fluorine Beam Etching of Silicon and Related Materials

2.1 ABSTRACT

A neutral atomic fluorine beam was shown to produce etch rates in Si and related materials as high as 1 μm/min. Etch rates were dependent on the substrate temperature and exhibited an Arrhenius-type behavior with the substrate temperature with an activation energy of 0.1 eV. Room temperature etching of Si was initially not observed until a carbon contamination layer was removed from the Si surface by an initial heating step, at which point etching was observed at the expected rate. Using a CaF_2 resist layer, 120 μm deep by 1 μm wide trenches (aspect ratio of 120:1) were fabricated in Si with little sidewall taper (slopes of about 1000:1) or aspect-ratio dependent etching effects. However, trying to reproduce these results on the nano-scale led to less impressive results, *e.g*. Si trenches 3.4 μm deep by 300 nm wide (aspect ratio

of 11:1) with sidewall tapers of about 10° were fabricated using e-beam lithographically defined Cr masks. This is thought to be due to the lack of a good high temperature fluorine resist as well as the anisotropic nature of the F-Si etching dynamics which is exhibited at length scales on the order of the width of the e-beam lithography defined trenches. Work on fluorine beam etching through AAO films is discussed in Chapters 5 and 6. Finally, much of this chapter was published with minor changes [8]:

P. R. Larson, K. A. Copeland, G. Dharmasena, R. A. Lasell, M. Keil, and M. B. Johnson, "Atomic Fluorine Beam Etching of Silicon and Related Materials", *J. Vac. Sci. Technol. B* **18**, 307 (2000).

2.2. INTRODUCTION

The ability to etch highly anisotropic features in silicon has been, and will continue to be, a crucial requirement for the size reduction of devices in integrated circuits. Currently, dry etching techniques such as plasma etching and reactive ion etching are used to transfer patterns into device substrates. These techniques have had remarkable success in fabricating highly anisotropic features, but they suffer from several disadvantages affecting their ability to etch such features on a still smaller scale. These disadvantages include: substrate damage due to charging and ion bombardment, feature-size dependence on the etch rate, and undercutting due to sidewall charging and scattering of reactive species [9, 10]. Recently, atomic beam techniques have been developed [11-15] that have the ability to etch anisotropic features into substrates [13]. With their relatively simple chemistry and use of low energy neutral atoms, these techniques do not suffer from several of the disadvantages listed above.

In this chapter, an application of an intense atomic fluorine beam to rapidly etch silicon and related materials is described. In addition, experiments were conducted that utilize the inherently collimated nature of atomic beams to fabricate extremely anisotropic etching features.

2.3. EXPERIMENTAL DETAILS

Figure 2.1 shows the atomic fluorine beam etching apparatus, which has been described elsewhere in detail [11]. The apparatus consisted of an atomic fluorine source connected via differential pumping to a target chamber. Diffusion pumps using fully fluorinated Fomblin oils evacuated both vacuum chambers. The target chamber pump is lN_2 baffled, and the pressure in this chamber was about $2x10^{-5}$ Torr ($5x10^{-6}$ Torr) while the beam is on (off). To generate a well-collimated, intense beam, a high-pressure (2000-3000 Torr) gas mixture of 5 % F_2 in He flowing through a ~150 μm-diameter nozzle at the tip of a MgF_2 tube was thermally dissociated. Heating the nozzle to ~900 ^oC resulted in a measured dissociation yield of about 70 % [11]. The kinetic energy of the atomic F beam was measured to be 1.0±0.1 eV. Downstream, the jet was collimated by a 750 μm-diameter skimmer before reaching the sample target. Beam intensities are difficult to measure directly [16], however, based on flow measurements for the He beam component, an estimate (within a factor of 2) of $1x10^{18}$ $cm^{-2}s^{-1}$ was made for the F intensity. Samples were cleaned using a standard degreasing treatment (acetone, methanol, and DI water) and in the case of Si samples this was followed by a dilute HF etch to remove any surface oxides. The samples were then mounted onto a resistively heated copper target assembly and loaded into the etching chamber.

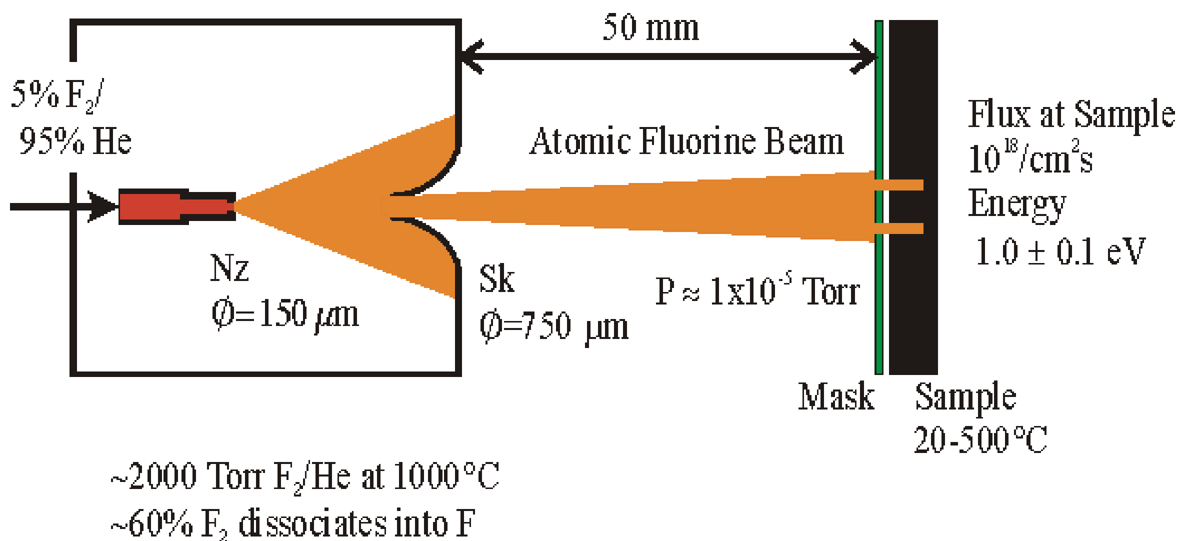

Figure 2.1. Schematic of atomic fluorine beam etching apparatus. A high-pressure (2000-3000 Torr) gas mixture of 5 % molecular fluorine in helium is introduced into a MgF_2 tube heated to 900 °C. At this temperature approximately 70% of the molecular fluorine dissociates into atomic fluorine. The gas mixture then expands through the 150 μm-diameter nozzle (Nz). The 750 μm-diameter skimmer (Sk) collimates the gas into a beam, which impinges on the masked sample in the target chamber. The energy of the atomic fluorine in the beam is about 1.0±0.1eV, and the flux at the target is about $1x10^{18}$ $cm^{-2}s^{-1}$. Based on the diameter of the source nozzle and target position, the angular dispersion is 0.1°.

It is useful to comment on the effects that the very-high, rather than ultra-high, vacuum conditions may have on the etching process. In general, vacuum conditions affect an etching process either by: 1) the continual contamination of the etching surface, while etching is taking place; or 2) the initial build-up of a contamination layer before the etching process has been started. The effect that the non-UHV conditions have through mechanism 1) may be estimated by comparing the atomic fluorine beam flux on the sample to the flux of other vacuum constituents. Residual gas analysis of the $5x10^{-6}$ Torr background vacuum indicated it was nearly entirely composed of water and air. Using the usual monolayer (ML) formation rate of one ML per second at $1x10^{-6}$ Torr, we find that the flux associated with water and air is $1x10^{16}$ $cm^{-2}s^{-1}$, or the flux ratio of atomic fluorine to water and air is 100:1. Regarding oil backstreaming from the cold-trapped diffusion pump, the Fomblin oil partial pressure is about 10^{-8} Torr, as given by the vapor

pressure of Fomblin oil at the chamber temperature of about 25 ^{o}C [17]. Thus the flux ratio of atomic fluorine to Fomblin oil is $5x10^4$:1. Such large flux ratios are due to the highly directional nature of the intense atomic fluorine beam. These flux ratios imply that *once etching begins* the effect of water and air in direct etching will be small and the effect of Fomblin vapor will be negligible. On the other hand, through mechanism 2), a thin layer of Fomblin oil initially present on the sample at room temperature may protect the substrate and partially inhibit etching until the oil is removed by heating the sample to some threshold temperature, that depends on the vacuum conditions. Such behavior is supported by the fact that the vapor pressure of Fomblin oil at 100 ^{o}C is about four orders of magnitude larger than at room temperature, so that at elevated sample temperatures one expects the layer of Fomblin oil to reduce in thickness or disappear entirely. In fact, evidence of the presence of a contamination layer was directly observed in two ways. First, as the vacuum conditions were improved (*e.g.,* by using a cold-trap on the diffusion pump and using sorption pumps to rough the etching chamber, rather than a mechanical pump) a reduction of this threshold temperature from about 150 ^{o}C to below 80 ^{o}C was observed. Second, by initiating etching with a sample temperature at 120 ^{o}C and quickly reducing this temperature to 25 ^{o}C, while continuing to etch the sample, room temperature etching was *directly* observed at the expected rate. (This result is discussed in more detail in the Results Section.) In summary, the only effect of the very-high vacuum conditions that was observed is a thin contamination layer that initially inhibits etching. To eliminate the effect of this layer, unless otherwise stated, all of the results reported here are for substrate temperatures at or above 120 ^{o}C, where the observed effect was negligible and for the best possible very-high vacuum conditions.

2.4. RESULTS

2.4.1 Bulk Etch Rates of Si and Related Materials

Figure 2.2 (a) shows etch depths versus time for silicon and related materials at a substrate temperature (T_{SUB}) of 120 ^{o}C. Etch depths were measured by etching through a nickel grid, with 0.5 mm openings and 0.75 mm period, using a Tencor Profilometer to measure step heights. Etch rates were determined by etching samples for various time intervals. The spread in the data is due to run-to-run variations in the atomic flux arising from changes in the beam-source nozzle temperature and pressure. (Thermal dissociation of F_2 is highly sensitive to both temperature and pressure.) Typical run-to-run etch-rate variations for the same nominal conditions were about 20 %, while variations within the same run were lower.

Measured etch rates for silicon, silicon nitride, and silicon dioxide for a substrate temperature of 120 ^{o}C are 0.2, 0.08, and 0.03 μm/min, respectively [18]. Typical photoresist materials etch at the rates shown in the table inset in Figure 2.2 (a), which also shows their etch selectivities compared to silicon. Fully fluorinated bulk materials such as Teflon and CaF_2, and materials such as bulk Ni that form non-volatile fluorides, do not etch even at temperatures well above 100 ^{o}C. It is important to make the distinction between bulk materials and thin films as further experiments indicated a temperature dependent threshold thickness below which materials such as Ni would etch. Above this threshold thickness for Ni, it was found that the thickness of the film actually slightly increased presumably due to the buildup of a nickel fluoride layer.

Figure 2.2 (b) shows a plot of etch rate versus sample temperature, for temperatures from 80 to 500 ^{o}C (solid squares), plotted in the usual Arrhenius form. The good straight-line fit (solid line) through the data indicates a substrate-temperature-activated process with activation energy of 0.1 eV as given by the slope. An etch rate as high as 1 μm/min for silicon is observed for T_{SUB}=500 ^{o}C. For a substrate temperature of 25 ^{o}C and etch time of 15 minutes, the etching rate directly measured was 9×10^{-4} μm/min, two orders of magnitude lower than the etch rate expected for Arrhenius behavior. This is most likely explained by a thin protective layer of Fomblin oil

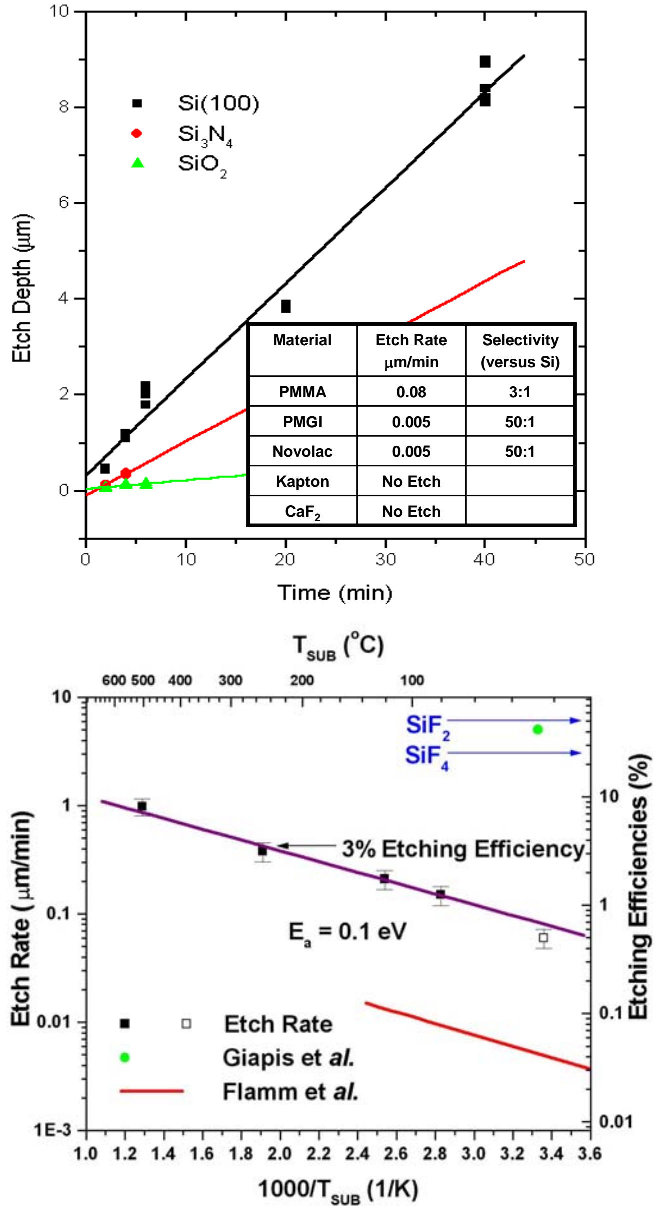

Material	Etch Rate μm/min	Selectivity (versus Si)
PMMA	0.08	3:1
PMGI	0.005	50:1
Novolac	0.005	50:1
Kapton	No Etch	
CaF_2	No Etch	

Figure 2.2. (a) Etch depth vs. time for silicon, Si_3N_4 and SiO_2 at T_{SUB}=120°C. Measured etch rates of resists at 200°C given in table (inset). (b) An Arrhenius plot showing silicon etch rate versus 1000/T_{SUB}. Our results are shown with a solid line through solid squares. Room temperature etch rate is shown as an open square. The arrows indicate etch efficiencies for silicon assuming two (four) fluorine atoms for every silicon atom removed, *i.e.* SiF_2 (SiF_4). Results shown for Flamm *et al.*[11] (dashed line) and Giapis *et al.*[5] (solid circle) are normalized to our flux in order to compare etching efficiencies.

that inhibits the etching. To demonstrate the existence of a contamination layer and that this layer can be removed effectively by heating the sample to 120 ^{o}C, a silicon sample was first etched for 5 minutes at 120 ^{o}C, then cooled to 25 ^{o}C in about 2.5 minutes with the fluorine beam still on, and finally, continued etching for one hour. For this procedure, the cumulative etch depth was found to be 4.6 μm, much deeper than expected if only the etching at 120 ^{o}C was effective. The depth attributable to room temperature etching was determined by subtracting the known depth for etching at 120 ^{o}C for 5 min. (1.1 μm, as measured in this run), and the depth for etching during the 2.5 min. cool down (0.3 μm, using etch rates at three intermediate temperatures determined by extrapolation). This gives a room temperature etch rate of 0.06 μm/min which agrees well with the Arrhenius behavior, as shown in Figure 2.2 (b). The difference between the two room-temperature measurements directly indicates the presence of a thin layer of contamination that inhibits etching during direct room temperature etching, which however, is removed by first initiating etching at 120 ^{o}C. Finally, for comparison, on the Arrhenius plot in Figure 2.2 (b), results are shown from Flamm *et al*. [19] (dotted line) for atomic fluorine gas etching, and Giapis *et al*. [13] (solid circle) for atomic fluorine beam etching. All these results have been normalized to the flux in this work to compare etching efficiencies. Detailed comparisons of these different etching techniques are left to the Discussion Section below.

2.4.2 Bulk-Etched Si Surface Topography

The roughness of etched surfaces was measured by atomic force microscopy using a Topometrix TMX 2000 AFM. A Si(100) sample etched for 5 minutes at 200°C (about 1.3 μm of Si removed) had an RMS roughness of about 30 nm. This roughness is

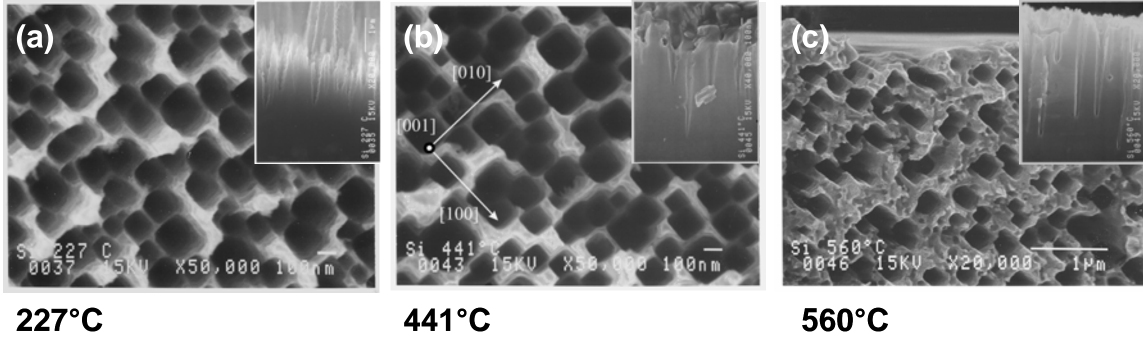

Figure 2.3. Top down and cross-sectional SEM views (inset) of unpatterned F-etched Si(100) at substrate temperatures of 227 °C, 441 °C, and 560 °C. Note the anisotropy in the [100] and [010] directions in the top down views. Also, note how the sidewall taper angle gets smaller as the temperature increases in the cross-sectional views.

similar to that observed using other fluorine-based etching techniques [20, 21]. In addition, the etched surfaces of Si(100) samples were further investigated with scanning electron microscopy (SEM) at different temperatures. Figure 2.3 shows top down SEM micrographs for bulk Si(100) etched at 227 °C (a), 441 °C (b), and 560 °C (c). The insets in the upper right hand corner show the corresponding cross-sectional views. Looking at the top down images, the surface was seen to consist of roughly square-shaped natural trenches. Note the anisotropy in the [100] and [010] directions in the top down SEM images implying an anisotropy in the etching dynamics between F and Si. From looking at the cross-sectional views of the bulk etched Si, it appears that substrate temperature plays an important role in the sort of taper angle formed. Qualitatively, a higher the temperature leads to a smaller taper angle implying that higher temperatures are necessary for high aspect ratio structures.

2.4.3 Lithographically Patterned, Fluorine-Etched Si

To investigate the anisotropic nature of etching Si with this atomic fluorine beam, CaF_2 was used as an etch-resistant mask. For the CaF_2-masked Si(100) substrates, 1 μm-wide slots were opened in molecular-beam-epitaxially grown 20 nm-thick CaF_2 layers

using electron-beam lithography following the procedure of Hirose *et al.* [22]. In this case, a standard SEM (JEOL JSM-880) with a 20 keV, 1 nA electron beam was used to write lines with a dose of 2.5 Ccm^{-2}. CaF_2 under direct electron-beam exposure dissociates leaving Ca, which oxidizes in air. The resist layer was then developed in water (CaO is 100 times more soluble in water than CaF_2) leaving 1 μm-wide openings to the underlying silicon. Figure 2.4 (a) shows a cross-sectional SEM view of a 1 μm-wide, 120 μm-deep trench in Si(100) fabricated by etching for 100 minutes with T_{SUB}=500 °C. This trench is extremely anisotropic, with an aspect ratio of about 120:1 and a sidewall slope of about 1000:1 over nearly the entire depth. These aspect ratios and sidewall slopes were directly measured from SEM micrographs of samples cleaved along a plane intersecting the etched trench at a right angle and are comparable or higher than those currently achievable by reactive ion etching [23, 24]. Another notable feature is that the

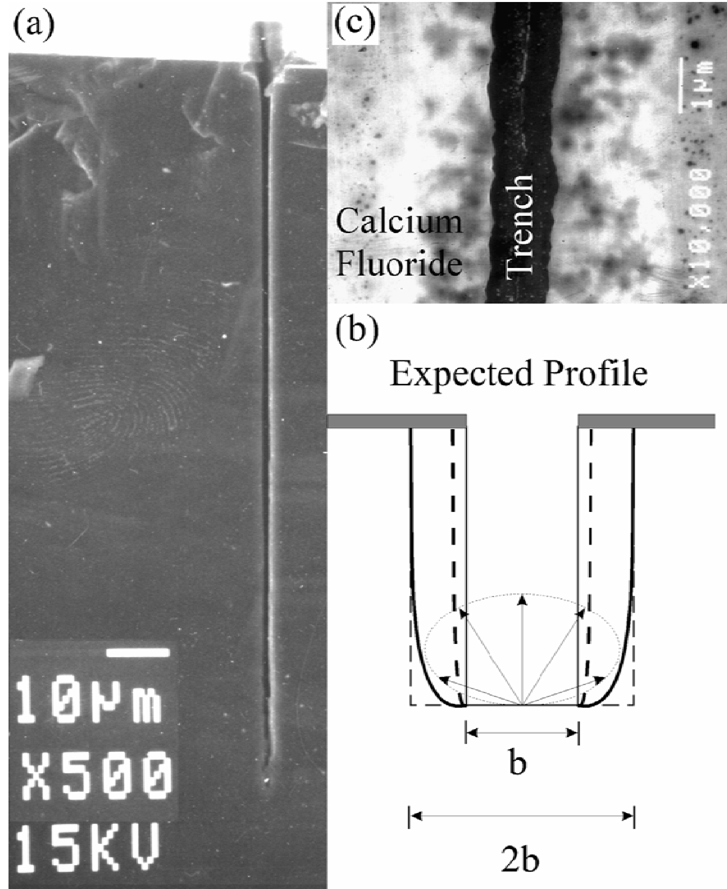

Figure 2.4. (a) Cross-sectional SEM view of a 1 μm wide, 120 μm-deep, CaF_2-masked trench in Si(100). (b) Plot of the expected profile assuming a cosine distribution for reactive species scattered at the bottom of the trench with the solid (dotted) line for full (20%) reactivity. (c) Top down SEM view of the trench and the CaF_2 mask, as labeled. Note the pinholes in the CaF_2 mask.

1.2 μm/min etch rate observed for the trench is within 20 % of the open-area etch rate of 1.0 μm /min at 500°C (Figure 2.2 (b)). Since this is comparable to the run-to-run error of the experiments (see above), it was concluded that this atomic beam does not exhibit appreciable aspect-ratio dependent etching (ARDE) effects [9], for the conditions presented here.

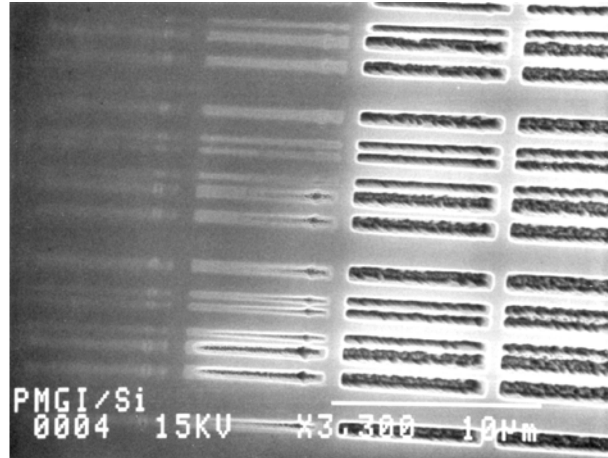

Figure 2.5. Top down SEM view of fluorine etched trenches in Si. The pattern was produced using e-beam lithography on 60-80 nm thick PMGI resist. The Si was then fluorine etched for 10 minutes at 190 °C. The areas that were not etched through are due to varying exposures of the e-beam.

ARDE effects were seen however as patterned structures with smaller dimensions were etched. In an effort to go to nanometer scale geometries (i.e. same high aspect ratios but nanometer size openings), e-beam patterned photoresists were used as masks to etch Si. Figure 2.5 shows a top down SEM view of some typical results using e-beam lithography on 60-80 nm thick PMGI resist. The Si was fluorine etched for 10 minutes at a substrate temperature of 190 °C. The areas that were not etched through are due to varying exposures of the e-beam. The problem with this technique is that the fluorine etches most organic photoresists, and this limits the ultimate depth attainable using this technique. Another problem with organic photoresists is their inability to withstand temperatures above about 200 °C. The inset table in Figure 2.2 (a) shows etch rates and selectivities (compared to Si) of some more common photoresist materials.

The results obtained with organic photoresists indicated that another more suitable high temperature fluorine resist was needed. With this idea in mind, a double resist

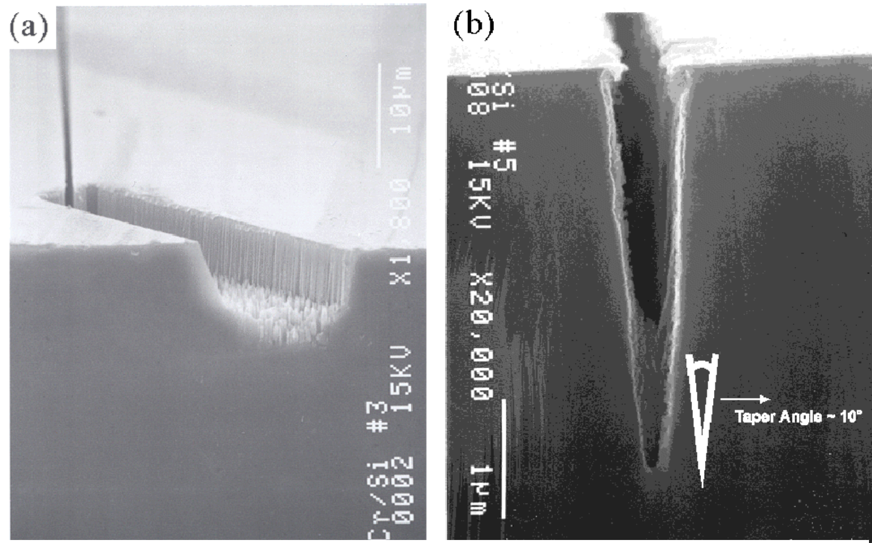

Figure 2.6. (a) Oblique angle SEM view of F-etched trench in Si fabricated using a double layer resist technique. The sample consisted of 60 nm e-beam patterned PMMA on 50 nm evaporated Cr. The pattern was transferred to the Cr layer by means of a Cr wet etch. The sample was then etched in the fluorine beam for 17 minutes at 250 ^{o}C. (b) Cross-sectional SEM picture of fluorine etched trench in Si. The sample was fabricated in the same manner as (a). The resulting trench is 300 nm wide and 3.4 μm deep. Note the sidewall taper of about 10°.

transfer technique was attempted using e-beam patterned photoresists to define the pattern, with an underlying Cr layer providing the mask to the fluorine. The patterned was transferred from the photoresist to the Cr layer by means of a Cr wet etch, before the sample was exposed to the fluorine beam. Figures 2.6 (a) and (b) shows SEM views of trenches fabricated in this way. The samples consisted of ~ 60 nm e-beam exposed PMMA on ~ 50 nm evaporated Cr on Si(100). The sample in the cross-sectional SEM in Figure 2.6 (b) was fluorine etched for 17 minutes at a substrate temperature of 250 ^{o}C. The width of the trench is about 300 nm and the depth is roughly 3.4 μm, giving an aspect ratio of around 11. The Cr etched at a rate of about 8 nm/min at 250 ^{o}C which once again limited the ultimate depth attainable for the trench. Another important point to note about the trench etched using the Cr mask is the sidewall taper of about 10°. This was not observed in the original results using CaF_2 masked trenches etched at a substrate temperature of 500 ^{o}C. As discussed in the next section, it is thought that ARDE effects

begin to show up when the width of the patterned structures starts to approach the width of the naturally occurring etched trenches in unmasked Si (Figure 2.3) due to the anisotropy in the F-Si etching mechanism.

2.5. DISCUSSION

In this section, the open-area etch results are discussed first followed by a discussion on the extremely anisotropic trenches obtained by etching through 1 μm wide CaF_2 slot masks. In both cases the results of this work are compared to results obtained using other related techniques. Finally, the results in attempting to etch nanoscale trenches while still maintaining high aspect ratios are discussed.

2.5.1 Bulk-Etched Si and Related Materials

In this work, it was found that the Si etch rate dependence on sample temperature and the etch selectivity to SiO_2 and Si_3N_4 are in qualitative agreement with those observed elsewhere [19]. Returning to the Arrhenius plot of Figure 2.2 (b), it is noted that the activation energy of 0.1 eV is in good agreement with Flamm *et al*. [19]. However, it should be observed that there is a large disparity between the etch efficiencies for the different etching techniques. The right axis of the Arrhenius plot directly indicates the efficiency of Si removal by fluorine. (The arrows at 50 % and 25 % indicate an etch rate assuming unit efficiency for producing SiF_2 and SiF_4, respectively.) Based on the atomic fluorine flux, the etching efficiency for fluorine beam in this work is 3 % for T_{SUB}=250 ^oC, *i.e.*, one Si atom is removed for every 30 incident fluorine atoms. This is much higher than the 0.25 % efficiency determined by Flamm *et al*. [19] (extrapolated to T_{SUB}=250 ^oC) for etching with room-temperature atomic fluorine gas.

Conversely, the results of Giapis *et al*. [13] demonstrate much higher efficiencies for an energetic fluorine beam generated by pulsed laser-induced dissociation of SF_6, even though this beam is incident upon a room-temperature substrate. It is therefore concluded that the etching rate is strongly dependent upon the incident kinetic energy of the atomic fluorine, [25] which averages 0.025 eV for Flamm *et al*. (0.25 % efficiency), 1 eV for the present work (3% efficiency), and 5 eV for Giapis *et al*. (40 % efficiency at room temperature). As discussed below, this energy dependent etch efficiency is important for the anisotropic etching results achieved in this work.

2.5.2 Micron-Scale, CaF_2-Masked Si Trenches

As noted in the Results Section associated with the highly anisotropic trench, two important features are observed: 1) a lack of aspect ratio dependent etching (ARDE) and 2) a lack of sidewall etching. To understand this behavior the anisotropic etching process is discussed and modeled in terms of a highly collimated beam incident through a slot into the trench and the transport of the reacted and unreacted gas products out of the trench. Below this process is discussed and modeled to explain, first the lack of ARDE, and second the lack of sidewall etching.

The lack of observation of ARDE, even for the high aspect-ratio trench, may at first be surprising because ARDE is often observed for the usual medium-vacuum plasma techniques. However, in this beam technique, the incoming atoms in the beam will have little or no interaction with the trench walls. This is a consequence of the mask geometry and the fact that the beam is very well collimated. (This is in contrast to other gas-phase techniques where the interactions of the incident (uncollimated) reactive species with the trench walls are very important.) In the atomic beam case, it is the gas-gas phase

interaction of the incident reactive F atoms with the effusive gas load from the trench bottom, which ultimately limits the depth of the trench for a given width. As shown below, this lack of observation of ARDE in the CaF_2-masked etch experiment is indicating that the mean-free-path length of the atomic F in the incident atomic beam in the trench (including the build up of pressure at the bottom of the trench) is larger than the depth of the trench itself. Adapting the procedure of Coburn and Winters [26], the pressure at the trench bottom is determined in accordance with Knudsen transport by treating the trench bottom as a gas source and the trench itself as a conductance to the vacuum chamber at base vacuum. Note that implicit in considering Knudsen transport for the gas scattered from the trench bottom is the assumption that this gas will be randomly distributed in both energy and direction, in sharp contrast to the incident beam. This assumption is reasonable given that Hwang *et al.* [27] observed a largely cosine distributed scattered flux in their atomic F scattering experiments associated with both trapping desorption and indirect inelastic scattered fluorine [28]. In this case, because the trench bottom is not smooth, as discussed in the Results Section, even the direct scattering will tend to be random implying a cosine angular distribution. Using Q as the mass flow, or throughput, from the trench bottom that arises from the scattered incident beam, taking into account that by far the greatest contribution to this gas throughput is from the 95 % He in the beam (the etch products themselves having negligible effect), we find that

$$Q = C\Delta p \approx kT\,\Phi_{He}\,ab, \qquad (2.1)$$

where Φ_{He} is the incident beam flux, a and b are the length and width of the trench, respectively, C is the trench conductance, Δp is the pressure difference between the

trench bottom and outside the trench, and kT is included to convert from atoms/s to Torr-liter/s. The conductance for a slot with rectangular cross-section in the Knudsen flow regime is

$$C = K\frac{8}{3}\left(\frac{kT}{2\pi m}\right)^{1/2}\frac{ab^2}{L} \text{ for } a >> b, \tag{2.2}$$

where L is the trench depth, T and m are the temperature and mass for the gas species, and K is an experimental geometry-dependent correction factor [29]. Using Eqns. (2.1) and (2.2) and rearranging, one finds

$$\Delta p = \frac{3}{8K}\left(2\pi mkT\right)^{1/2}\frac{\Phi_{He}L}{b}. \tag{2.3}$$

Using K=2, Φ_{He}=1.3x10^{19} cm^{-2}s^{-1}, and m and T for He at the source temperature of 900 ^{o}C (1173 K) equation (2.3) gives a pressure difference of about 70 Pa or 500 mTorr [30]. This pressure difference, Δp, is essentially the pressure build-up at the bottom of the trench, p_t, because the pressure outside the trench (2x10^{-5} Torr) is negligible in comparison. Using the relationship between mean-free path length, λ, and pressure from Ref. 31, and Eqn. (2.3), it is found that

$$\lambda = \left(1+\frac{M_F}{M_{He}}\right)^{-1/2}\frac{kT}{p_t\sigma_{He-F}} \propto \frac{b}{\Phi_{He}L}, \tag{2.4}$$

where M_F and M_{He} are the atomic masses of F and He, respectively, and σ_{He-F} is the Helium-Fluorine cross section [32]. Using M_F/M_{He}=19/4, T=1173 K, p_t=500 mTorr and σ_{He-F} = 0.2 nm^2, it is found that the mean free path of the incident atomic fluorine in the beam is about 500 µm. (Note that in this calculation the gas temperature of He in the source was used and all scattering except F-He scattering was neglected, however, taking

T equal to the sample temperature, and including the other gas species has little effect on this outcome.) This mean-free-path length exceeds the trench depth by a factor of four, which explains the absence of gas-gas interactions leading to ARDE. Alternatively, by considering the probability of an incident F atom to undergo a collision as given by the mean-free-path length above, one finds that the probability of an incident F atom reaching 120 μm depth *without* collision is about 90 %. The ultimate depth attainable for a given trench width can be estimated by determining the depth at which this collision probability is about 50 %. Under the conditions of the present experiment, this depth is about 250 μm for a 1 μm-wide opening of the trench. In addition, as indicated from Equation (2.4) the ultimate depth of a trench, L, scales with its width, b. In other words, for this analysis the critical parameter for attaining a trench of a certain depth is its aspect ratio, L/b. For the beam flux used in this work, the ultimate aspect ratio is about 250:1, however, by reducing the incident flux, even higher aspect ratios should be possible. Finally, based on this analysis, such high aspect ratios should be possible for much smaller trench openings, however this was not seen experimentally.

Regarding the observed lack of sidewall etching, for a collimated neutral beam, undercutting results from reactive species scattering within the trench and then striking and etching the sidewalls. As discussed above, for the pressure regime and geometry in this work, gas phase interactions within the trench are not important. Only reactive species scattered from the trench bottom will contribute to sidewall etching. Given the relatively low efficiency of etching (7 % at 500 ^{o}C), it is expected that there is substantial backscattered atomic fluorine. Again, as discussed above, as observed by Hwang *et al.* [27] and because the trench bottom is not smooth, it is a reasonable assumption that the

reactive backscattered flux comes off with a cosine distribution. Therefore one can model the effect of this backscattered atomic fluorine by: treating *each* element of area on the trench bottom as a cosine distributed source of fluorine, $\Phi_F dxdy$; integrating over the trench width, x from 0 to b, and length, y from $-\infty$ to ∞ (a very long trench is being considered) to determine the flux density of atomic fluorine at a point z on the sidewall as

$$P(z) = \frac{\Phi_F}{2}\left(1 - \frac{z}{\sqrt{z^2 + b^2}}\right), \tag{2.5}$$

where $z=0$ is the bottom of the trench. Finally, (assuming a uniform etch rate, μ, so that the depth of the trench, z, is given by $z=\mu t$, where t is the etch time) by integrating over the time corresponding to the time to etch from position z on the side wall to the final bottom of the trench, it is found that the number density of fluorine atoms that hit the sidewall at a position z on the trench wall is

$$Q(z) = \frac{\Phi_F}{2\mu}\left(z + b - \sqrt{z^2 + b^2}\right). \tag{2.6}$$

The solid curve in Figure 2.3 (b) shows the trench profile calculated using this model with the assumption that the reactivity of backscattered fluorine is undiminished from that of fluorine incident upon the bottom of the trench. This profile shows a trench twice as wide as the mask opening with substantial curvature at the trench bottom. The dotted profile, calculated by assuming reduced reactivity of the scattered species by a factor of five, still shows widening, again with curvature at the bottom. The form of sidewall curvature given by this model is absent in our trenches. Etching of the sidewall at the top of the trench is seen within about 3 μm of the mask, but this is clearly not of the form expected from scattered reactive species. In fact, the top feature appears to be

the result of fluorine atoms that pass through pinholes in the CaF_2 mask near the trench opening and etch the Si. These pinholes are shown in the SEM micrograph in Figure 2.3 (c).

This lack of sidewall etching observed in our trench is both qualitatively and quantitatively different from that observed by Giapis *et al.*, who use atomic F with much higher incident kinetic energies [13, 27]. For F atoms incident at 5 eV, they see sidewall etching of about 14%, while this is reduced to about 3 % for F atoms at 18 eV. Interestingly, much less sidewall etching is observed in this case even though the etch rate indicates a lower fluorine reaction efficiency. This implies that the large number of F atoms scattering from the bottom do not significantly etch the sidewalls in this case. Thus the observed lack of sidewall etching must result from reduced etching efficiency for F atoms scattered from the trench bottom, or to build-up of a passivation layer due to residual vacuum constituents, or to both. It is thought that the former is much more likely, as is now discussed.

In order for atomic F to contribute to sidewall etching, the fluorine atoms incoming from the highly collimated beam must first strike the trench bottom, since the role of gas-gas collisions in the trench is negligible. Even partial energy accommodation with the surface will then deprive most of these F atoms of a considerable fraction of their incident 1 eV kinetic energy, so that subsequent collisions with the sidewall will occur with much lower kinetic energy and at very large incident angles. Both these conditions would reduce sidewall etching efficiency. For example, based on the work of Flamm *et al.* [19], extrapolated using Figure 2.2 (b), thermalized F atoms would etch Si at a rate of only about 0.1 μm/min (at 500 ^{o}C), which is a factor of ten lower than our

observed (downward) etching rate (thermalization at the substrate temperature of 500 ^{o}C implies an average kinetic energy of 0.07 eV). Thus, from kinetic energy arguments alone, one would expect diffusively scattered fluorine to etch at a much slower rate than the atomic fluorine incident at 1 eV directly from the beam. Indeed, the magnitude of this variance in etch rates can by itself explain the sort of anisotropy observed. The alternative possibility that sidewall etching is inhibited by build-up of a passivation layer from the non-UHV background is unlikely because, as discussed earlier, the ratio of background flux to the atomic fluorine beam flux is very low. Furthermore, this flux ratio on the sidewalls becomes even smaller as the trench gets deeper due to the slowness of Knudsen transport of background constituents down the trench. If the background vacuum was important, passivation would be more complete higher up the trench, and one would expect to see the trench widen as it goes deeper, which is not observed at all.

2.5.3 Nano-Scale Si Trenches

The above analysis suggests that the etching process is aspect ratio dependent with very little sidewall etching making this process ideally suitable for etching high aspect ratio nanoscale features. However, this was not observed experimentally as seen in the trench widening and sidewall taper observed in the cross-sectional SEM in Figure 2.6 (b) and also in anodic aluminum oxide (AAO)-masked trenches shown and discussed in Chapter 5. This is due to the lack of a suitable high temperature fluorine mask as well as the possible failure of the trench model and analysis developed in the proceeding section at these length scales. The preceding model and analysis does not take into account the anisotropic F-Si etching mechanism that can be directly observed in the SEM images shown in Figure 2.3. The top down images suggest that F etches different Si

planes at different rates. In addition, these different plane etch rates are highly dependent on temperature and thus affect the sidewall taper angles as seen in the inset cross-sectional images. In the model and analysis discussed above, a uniform etch rate, $\mu = z/t$, was assumed which was a valid for the large trench widths being discussed, since in this case the anisotropic F-Si etching mechanism could be essentially ignored. However, at length scales approaching the naturally occurring trenches in unpatterned Si (typical trench widths are around 100-300 nm) this assumption is no longer valid and the anisotropy in the etching dynamics can no longer be ignored. In fact, when trying to etch patterned structures approaching the scale of the naturally formed trenches in unpatterned Si, trench widening and increased taper angles are observed consistent with the naturally formed trenches. This etching anisotropy along with the lack of a suitable high temperature F mask led to trenches with aspect ratios limited to around 10 with taper angles of approximately 10°. In contrast, the high aspect ratio trench shown in Figure 2.4 is a direct result of the large width of the trench (essentially a bulk material size of 1 μm) where the highly anisotropic nature of the F-Si etching mechanism could be ignored.

Trenches of the width and depth demonstrated here may be useful to micro-electro-mechanical-systems (MEMS) applications, as well as isolation trenches in integrated circuits. Of course this will require uniform etching over realistic wafer dimensions. This can be attained through a combination of increasing the beam size and rastering the wafer under the enlarged beam. The former can be accomplished by enlarging the skimmer, or by moving the sample further from the nozzle (Figure 1), or both. Increasing the nozzle-sample distance increases the beam flux, which can be compensated by increasing the gas flow.

2.6. CONCLUSION

A neutral atomic fluorine beam was shown to produce etch rates in silicon as high as 1 μm/min. Using a CaF_2 resist layer 120 μm deep by 1 μm wide trenches (aspect ratio 120:1) were fabricated in silicon with no appreciable sidewall taper (slopes of about 1000:1) or ARDE effects. Achieving such anisotropic etching suggests that scattered species do not contribute significantly to sidewall etching, *i.e.* the vast majority of etching is caused by the highly directional incident atomic-fluorine beam. Although sidewall passivation caused by background vacuum constituents could be inhibiting sidewall etching, it is shown that this is unlikely due to the much larger flux directed at the substrate by the collimated atomic fluorine beam. It was calculated that the ultimate depth attainable for a 1 μm wide trench is about 250 μm, and it was shown that that the critical parameter for the ultimate depth of a trench is its aspect ratio with the caveat that the width of the trench be larger than the naturally occurring trenches in unpatterned Si so as to not be affected by the anisotropic F-Si etching dynamics. Because of this anisotropy and the lack of a good high temperature thin film fluorine resist, extending this work to the nanoscale lead to structures with aspect ratios of around 11:1 for a 300 nm wide trench with a taper angle of 10°.

Chapter 3

Anodic Aluminum Oxide Films

3.1. ABSTRACT

This chapter focuses on the growth and characterization of anodic aluminum oxide (AAO) films and is intended as a guide for future experimentalists working with AAO films. To start, a general review of the history and growth mechanisms of AAO films (both barrier- and porous-type) will be presented. Like porous films, barrier-type films are grown from an aluminum foil in an electrolytic cell, but the resulting film is nonporous. However, because the growth mechanism involved in barrier-type oxides also plays an integral part in porous oxide growth, understanding this process is essential for understanding the growth of porous films. Next, the growth of porous alumina films will be discussed including the processes involved in the ordering of the resulting pores into a hexagonal close packed array under the appropriate anodizing conditions. Finally, work done on optimizing the growth of porous AAO films specifically for use as templates or masks for the fabrication of nanostructures will be

presented. This includes preparing the Al foil growth substrate, finding suitable anodization conditions for maximizing the ordering of the AAO nano-pores, and tailoring the pore dimensions, spacings, and AAO thickness.

3.2. BACKGROUND AND OVERVIEW OF AAO FILMS

It has long been known that the surface of aluminum has a high affinity for oxygen. As such, the metal is covered with an oxide film about 1-2.5 nm thick that forms immediately upon exposure to air [33]. Anodic oxidation, or anodizing, is an electrolytic process for improving this natural oxide to produce a thicker, more resistant oxide film on aluminum. The aim of this process is to produce an oxide film which has excellent corrosion resistance, is attractively finished, and possesses other commercially desirable qualities. As such, anodic aluminum oxide (AAO) films have been fabricated commercially for corrosion resistant applications since approximately the 1930s [33].

In general, the type of AAO film that can be grown on aluminum can be broken up into two distinct categories: barrier-type and porous-type films. Barrier-type films consist of a relatively thin compact layer of alumina grown on an aluminum substrate, whereas porous-type films consist of an outer layer composed of a thick porous film structure of alumina on top of an inner compact layer of alumina on an aluminum substrate. Because of its similar properties to barrier-type oxide films, the inner compact layer in a porous-type film is termed the barrier layer. Figure 3.1 shows a simplified schematic of an electrolytic cell used for the growth of anodic oxide films and a cross-sectional view of the typical structure of a barrier-type and porous-type film. The type of oxide produced depends upon several factors, the most important of which is the nature

of the electrolyte. Barrier-type films are formed in nearly neutral electrolytes (pH values of 5-7) in which the formed oxide film is completely insoluble. Electrolytes of this type include neutral boric acid solution and ammonium tetraborate in ethylene glycol along with several organic electrolytes such as citric acid. Electrolytes in which the anodically formed oxide film is slightly soluble form porous-type films. The most common electrolytes of this type include sulfuric acid, oxalic acid, phosphoric acid, and chromic acid.

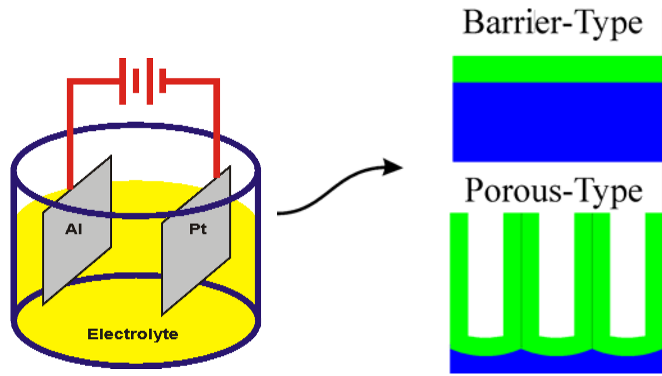

Figure 3.1. Simplified schematic of electrolytic cell (shown left) used to produce both barrier-type and porous-type alumina films (shown in cross-section on the right).

Apart from the different structural morphology of the two types of films, the other major difference is in the thickness of the film that can be produced. The thickness of barrier-type films is controlled by the applied voltage and is limited to a voltage below that corresponding to dielectric breakdown of the oxide which is around 500-700V [34]. The corresponding maximum thickness attainable for a barrier-type film is around 0.7-1.0 μm. These films are typically characterized by a parameter called the anodizing ratio given in terms of nm V^{-1} which specifies the approximate thickness of the film formed under a specific applied voltage. Typical values of the anodizing ratio for aluminum are 1.2-1.4 nm V^{-1}. In contrast, the thickness of the outer layer of porous-type films is time dependent, has no such limitations on the applied voltage, and can grow to be hundreds of microns thick. However, similar to barrier-type films, the thickness of the inner

compact layer of porous-type films is voltage dependent and can be described by an anodizing ratio that is typically smaller that that given for corresponding barrier-type films.

Barrier-type films are currently of commercial use in the field of dielectric capacitors and in the protection of thin, vacuum deposited aluminum. Conversely, porous-type films, which can be grown much thicker, offer excellent corrosion and abrasion resistance for bulk aluminum. In addition, due to their high porosity, they make an excellent base for paints and dyes. Therefore, porous-type films are often used in applications where the aluminum surface is to be protected from corrosion and also decorative applications where the normally transparent alumina film is dyed the appropriate color and sealed. Sealing is a process wherein the porous films are immersed in hot water. This process seals or closes up the pores which results in a nonporous film whose thickness is many times higher than those attainable in barrier-type films. The chemical process involved in sealing or closing up the pores is thought to be the formation of boehmite by partial hydration of alumina [35]:

$$Al_2O_3 + H_2O \rightarrow 2AlO(OH) \quad (3.1)$$

3.3. BARRIER-TYPE AAO FILMS

Although the bulk of this chapter is concerned with porous-type AAO films, the growth mechanism involved in barrier-type AAO films should be considered first before a more complete understanding of porous films can be obtained. As previously mentioned, barrier-type films are generally grown in an electrolytic cell with nearly

neutral electrolytes. The grown film is insoluble in the electrolyte and consists of a thin compact layer of aluminum oxide.

It should be noted that these anodic films are not pure oxides, since they contain varying amounts of impurities, such as water and the forming anion. X-ray and electron diffraction techniques along with infrared spectroscopy indicate that the resulting structure of barrier-type films is comprised mostly of amorphous material surrounded by microcrystallites of γ–Al_2O_3 with the amount of crystalline material increasing with increasing formation voltage and temperature [34, 35]. The intercrystallite regions contain amorphous alumina, molecular water (usually in the form of boehmite, (AlO(OH)), hydroxyl groups, and some anion species incorporated from the electrolyte solution. The amount of anion incorporation in barrier-type films is usually low (<10%) and depends on the electrolyte, voltage, and temperature.

Evidence found employing inert gas markers suggests that oxide growth proceeds at the metal/oxide interface as well as the oxide/electrolyte interface by the migration and subsequent reaction of oxygen containing anions and Al^{3+} cations under the applied field [33]. The oxygen containing anions are comprised mainly of OH^- ions and O^{2-} ions with the remainder being oxygen-containing anions from the electrolyte. There is then a

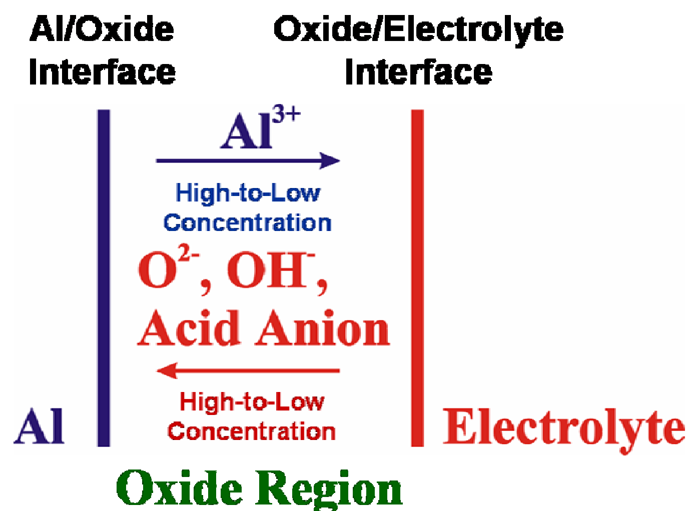

Figure 3.2 Schematic showing the ions involved in barrier-type oxide growth and the direction of the concentration gradients under an applied electric field.

concentration gradient of OH^-, O^{2-} and other oxygen-containing anions throughout the barrier-layer oxide with the highest concentration at the outer surface next to the oxide/electrolyte interface. The relative proportions of the migrating anions will depend on their charge and size as well as the local conditions at the oxide/electrolyte interface. Similarly, there is a concentration gradient of Al^{3+} cations throughout the film with the highest concentration gradient at the inner surface next to the metal/oxide interface. This situation is shown schematically in Figure 3.2. The overall electrochemical reaction occurring is:

$$2Al + 3H_2O \rightarrow Al_2O_3 + 3H_2 \qquad (3.2)$$

The underlying oxidation reactions occurring at the Al anode are:

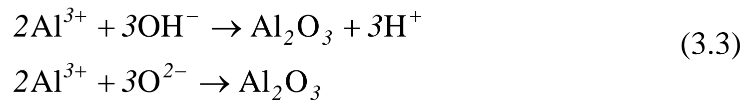

$$\begin{aligned} 2Al^{3+} + 3OH^- &\rightarrow Al_2O_3 + 3H^+ \\ 2Al^{3+} + 3O^{2-} &\rightarrow Al_2O_3 \end{aligned} \qquad (3.3)$$

Finally, the reduction reaction occurring at the inert cathode is the evolution of hydrogen gas bubbles:

$$2H^+ + 2e^- \rightarrow H_2 \qquad (3.4)$$

To better understand ionic migration across the oxide film, Figure 3.3 shows a simplified and approximate potential energy

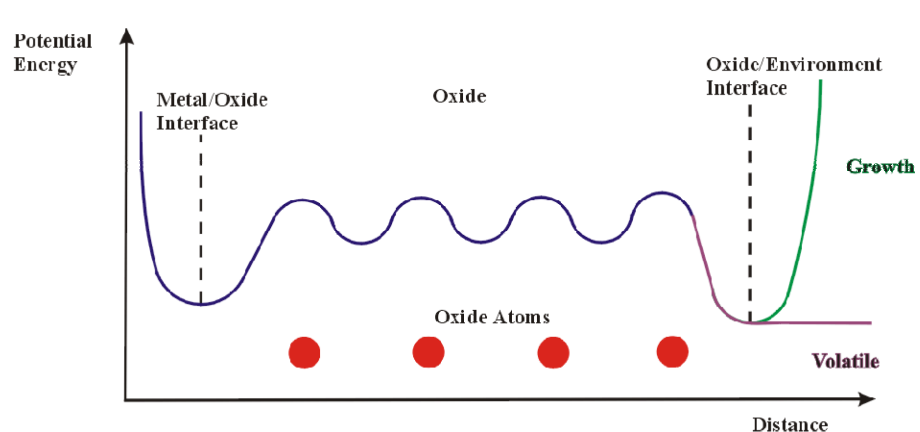

Figure 3.3. Approximate potential energy curve of a mobile ion in aluminum oxide

curve of a mobile ion in the oxide region. In order for a mobile ion to reach either the metal/oxide interface (in the case of oxygen containing anions) or the oxide/electrolyte interface (in the case of Al cations), it is necessary for the ions to "hop" over potential diffusion barriers. In the figure, the barriers correspond to the position of the atoms in the oxide and migration occurs by ions moving from one interstitial site to the next. It should be noted that the dominant mechanism of transport could also occur by vacancies or a place-exchange mechanism, but the qualitative nature of the potential energy curve would remain the same.

Application of an electric field, E, across the oxide results in an overall raising or lowering of the potential barriers by an amount qEa as shown in Figure 3.4 where a is half the interatomic distance and q is the charge on the mobile ion. From this and the use of elementary rate theory, the ionic current density, i, across a diffusion barrier at position x under the influence of an applied field can be expressed as [34]:

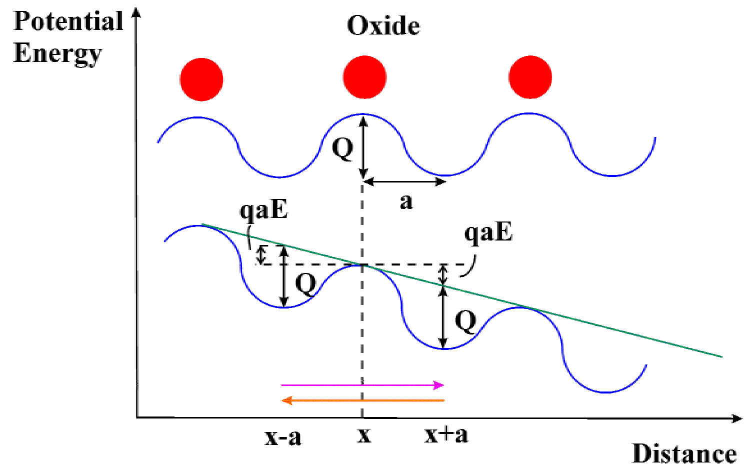

Figure 3.4. Resulting potential energy curve upon application of an electric field across the oxide.

$$i = 2a\nu \exp(-\frac{Q}{kT})\left\{n_{x-a} \exp(\frac{qEa}{kT}) - n_{x+a} \exp(-\frac{qEa}{kT})\right\} \tag{3.5}$$

where ν is the atomic frequency of vibration, Q is the height of the potential barrier, k is Boltzmann's constant, T, is the absolute temperature, and n is the concentration of the

mobile ions where the subscript indicates whether it is evaluated at *x-a* or *x+a.*

By converting the difference equation for i in expression (3.5) into a differential equation, and solving this equation for i and E independent of position (i.e. neglecting space charge effects), an expression for the concentration, n, can be solved for. Utilizing this expression, the current density can then be expressed as [37]:

$$i = -\frac{Dn}{kT}\frac{\partial \mu}{\partial x}\frac{\sinh(qaE/kT)}{qaE/kT} \tag{3.6}$$

where,

$$D = 4a^2 \nu \exp(-\frac{Q}{kT}) \tag{3.7}$$

and,

$$\mu = \mu^o + kT\ln(n) + qV \tag{3.8}$$

Here we see that D corresponds to the intrinsic diffusion coefficient for this model while μ is the chemical potential of the ionic species in the dilute approximation where μ^o is the intrinsic chemical potential.

At this point it is useful to look at two limiting regimes, namely the thin film, high E regime and the thick film, small E regime. For the previous case, if the thickness, d, of the oxide film is small, then $E=V/d$ is large and one exponential term in the $sinh(qaE/kT)$ expression of equation (3.6) dominates. Combining this with the assumption that $\partial n/\partial x=0$, the current density reduces to the well-known Mott-Cabrera conduction equation [38]:

$$i = 4a\nu n\exp(-\frac{(Q-qaE)}{kT}) \tag{3.9}$$

This equation simply describes the ionic conduction in terms of an effective activation

energy, $Q-qaE$, for migration across the thin oxide layer.

This can be contrasted with the thick film limit where d is large and hence, $E=V/d$ is small. In this case, the term $sinh(qaE/kT)$ in equation (3.6) can be replaced by its argument and making use of the Einstein relation, $\sigma/D=q/kT$, the current density can be expressed as [37]:

$$i = -D\frac{\partial n}{\partial x} + n\sigma E \tag{3.10}$$

where σ is the mobility of the ionic species. This simply considers the current density to consist of two parts, one due to diffusion and the other to the electric field. This familiar expression is probably encountered more often in the case of electronic conduction, but here it should be kept in mind that for this particular case it refers to ionic conduction.

In conclusion, oxide growth in barrier-type films proceeds by the ionic conduction and subsequent reaction of oxygen containing anions and Al cations at both the metal/oxide and oxide/electrolyte interfaces under the applied field. This same mechanism is responsible for the oxide growth in porous-type AAO films as well. However, as shown in the next section, there is also a field-assisted dissolution process present in porous oxide growth that is primarily responsible for the production of the pores. These two growth and etching processes work together to produce the unique structure of porous alumina.

3.4. POROUS-TYPE AAO FILMS

3.4.1 Structure and Composition

The structure of porous alumina has been obtained from secondary electron

microscope (SEM) and transmission electron microscope (TEM) techniques [34, 35, 39-43]. It has been shown to consist of a thin, compact, scalloped layer (called the barrier layer) next to the aluminum substrate with a thick, porous structure on top consisting of arrays of cylindrical shaped pores surrounded by an alumina backbone. The alumina surrounding the pores can be broken up to represent a hexagonal cell structure with each cell containing one pore. Figure 3.5 shows a schematic of the ideal structure of porous alumina. Under the most general fabrication conditions, the pores are not ordered as shown in the figure, but instead display a more random arrangement. Under these conditions, the pores are not necessarily circular and the cell structure can be quite distorted. However, as shown in a later section, under the appropriate anodizing conditions, porous alumina membranes can approach the ideal ordered structure as shown in Figure 3.5.

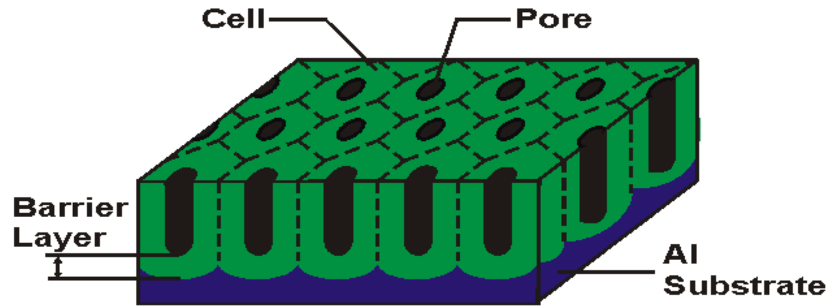

Figure 3.5. Schematic representation of ideal structure of porous alumina.

As in the case of barrier-type films, the grown oxide consists of regions of microcrystallites of pure alumina and amorphous regions containing alumina, water, and the acid anion [34, 35]. Recent studies have shown that the amorphous regions containing the acid anion are located around the pores with the barrier layer consisting of mainly crystalline alumina [44, 45]. In addition, the amount of incorporation of the acid anion into the structure depends highly on the electrolyte itself, with films grown in sulfuric acid electrolytes having the highest incorporation of acid anions followed by

oxalic, phosphoric, and chromic acid which contains practically no anion incorporation. In the latter case at least, this is thought to be due to the rather large size of the chromic acid anion.

3.4.2 Overview of Growth

As previously mentioned, porous-type alumina films are formed in essentially the same manner as barrier-type films except the nature of the electrolyte is such that the grown oxide is slightly soluble in it. There are many electrolytes that meet this criterion, but the most common and commercially important are phosphoric, oxalic, chromic, and sulfuric acids at varying concentrations [36]. The growth of porous-type alumina films proceeds by oxide growth at the metal/oxide and oxide/electrolyte interfaces in the same manner as described for barrier-type films. However, because the oxide is slightly soluble in the electrolyte, a competing process termed field-assisted dissolution takes place at the oxide/electrolyte interface. It is this process that is responsible for the generation of the pores at random positions throughout the oxide. If the anodizing conditions are right (*i.e.* appropriate electrolyte concentration, voltage, and to a secondary extent, temperature) then a steady state condition is soon setup in which the two predominately different reactions are occurring at about the same rate. This allows the propagation of the pores to continue along with the oxide growth. If however, one or the other of these two mechanisms dominates, then porous-type growth will not occur. For example if, as we've already seen, electrochemical oxidation leading to oxide growth dominates, then the film formed is a barrier-type oxide film. If, however, field-assisted chemical dissolution dominates, then a situation is setup where the oxide is dissolved nearly as fast as it is formed with the result that, at the end of the treatment, only a very thin oxide coating

remains. The simultaneous formation and rapid dissolution of the oxide tends to smooth out surface irregularities and produces a very smooth, mirror-like finish. This process is termed electropolishing [33]. The growth of porous alumina is therefore an intermediate case where oxide growth and the subsequent dissolution of this oxide are both occurring at roughly the same rate under steady state conditions.

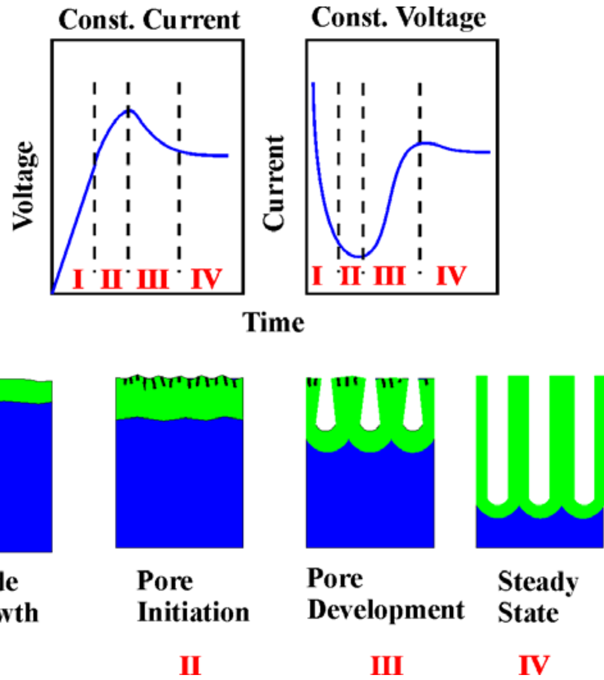

Figure 3.6. Voltage vs. time and current vs. time curves for anodizing at constant current density and constant voltage, respectively. The subsequent stages of pore growth are also shown.

Figure 3.6 shows voltage vs. time and current vs. time curves for anodizing at constant current and constant voltage respectively. It also shows the subsequent stages of development of the porous alumina films. The development of porous films under constant voltage anodizing will be described here although a similar situation occurs for constant current anodizing as well. Initially, when the voltage is first applied, the current starts out very high due to the fact that there is only a very thin oxide layer present and hence very little impedance for ionic migration. As the oxide film thickens, the current starts to fall as shown in region I of the curve. At this point, the current goes through a shallow minimum as pores start to initiate and hence more current pathways start to open up as shown in region II. It is during this region that field-assisted dissolution starts

becoming competitive with oxide growth. In region III, major pores are starting to develop and the current rises again due to the thin barrier layer at the base of the pores allowing current pathways for oxide growth. Finally, in region IV, the pores are fully developed, and a steady state situation is developed where the current density takes on a roughly constant value throughout the rest of the anodizing process. In this region, the growth and dissolution are occurring at roughly the same rate.

The oxide growth mechanism due to ionic migration has already been discussed in the previous section dealing with barrier-type AAO. The field-assisted dissolution process responsible for the production of the pores will now be examined in more detail before going on to discuss pore initiation, pore development, the steady state regime, and the special case of pore ordering.

3.4.3 Field-Assisted Dissolution

Figure 3.7 shows a schematic representation of the field-assisted dissolution process occurring at the oxide/electrolyte interface of porous alumina taken from reference [40]. For simplicity, the schematic assumes a NaCl-type arrangement of the aluminum oxide atoms, although in reality the bonding is more complex. Figure 3.7 (a) shows the oxide before application of an electric field. Due to the ionic nature of the aluminum

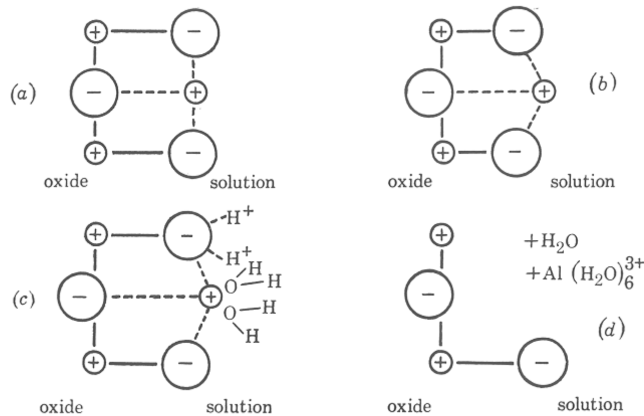

Figure 3.7. Schematic representation of the field-assisted dissolution of Al_2O_3 (a) before polarization, (b) after polarization, (c) removal of Al^{3+} and O^{2-} ion, and (d) the remaining oxide. Figure taken from Ref. [40].

oxide bonds, applying a field across the oxide polarizes the atomic structure of the material as shown in Figure 3.7 (b). This process effectively lowers the activation energy for dissolution of the oxide (Figure 3.7 (c)), allowing this process to occur much more rapidly than would occur without the field. This facilitates the solvation of Al^{3+} ions by water molecules and the removal of O^{2-} ions by H^+ ions giving water as shown in Figure 3.7 (d). One important consequence of this process is that essentially all of the Al^{3+} ions that migrate to the oxide/electrolyte interface do not contribute significantly to growth but are ejected into the electrolyte.

3.4.4 Pore Intiation

Early electron microscopy work performed in the 1970s by researchers at the University of Manchester Institute of Science and Technology helped to elucidate the process of pore initiation [40]. Figure 3.8 shows their transmission electron microscope (TEM) images of porous alumina films anodized at 50 A/m^2 in 0.4 M phosphoric acid at

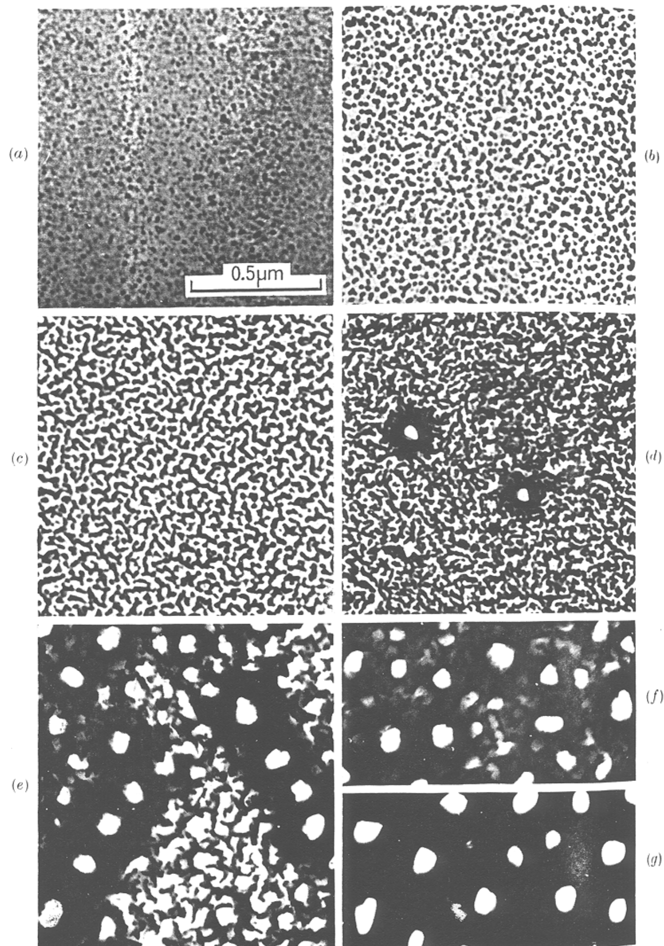

Figure 3.8. TEM images of porous AAO films grown at 50 Am^{-2} in 0.4 M phosphoric acid at 25oC for (a) 40 s, (b) 80 s, (c) 120 s, (d) 160 s, (e) 200s, (f) 280 s and (g) 330 s showing initial pore initiation and development. Images taken from Ref. [40].

various stages of development [40]. Bright regions in the images represent thinner areas of the oxide while the darker regions represent thicker areas. Initially, as shown in Figure 3.8 (a), regions of locally thicker oxide islands roughly tens of nm in diameter nucleate at random positions. Through Figures 3.8 (b)-(c), these islands increase in size and number. By Figure 3.8 (d), the onset of major pores is starting to develop due to the merging of these islands leaving thin areas of oxide in between. Figures 3.8 (e)-(f) show this trend continuing until all of the major pores are mostly developed by Figure 3.8 (g).

To explain this behavior, researchers at Keio University in Japan proposed a model to explain the development of pore initiation [46]. Figure 3.9 shows a cross-sectional schematic illustrating their model for the initiation of the pores [46]. Figure 3.9 (a) shows the roughness and non-uniform thickness of the initial barrier-type oxide layer. This results from the roughness of the initial aluminum surface as well as the induced stress in the oxide layer resulting from the difference in the density of the aluminum in the oxide compared to that of bulk aluminum. Furthermore, this stress causes cracks (Figure 3.9 (a)) in the oxide which then rapidly "heal" by enhanced oxide

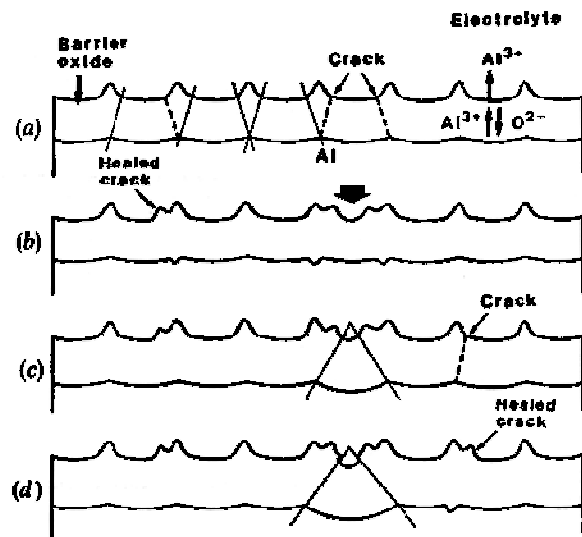

Figure 3.9. Schematic diagrams showing the non-uniform thickening of the barrier oxide and eventual development of major pores. Through the development of tensile stresses, cracks in the barrier oxide develop in the regions associated with pre-existing ridges at the metal/oxide interface. Current concentration results in the development of protuberances of locally thicker film at the oxide/electrolyte interface. Eventually, current concentrates in the locally thinner regions of the oxide on either side of the protuberances. Schematic taken from Ref. [46].

growth due to the increased ionic mobility in the cracks. This leads to even further surface roughening as shown in Figure 3.9 (b). The current is then enhanced in the thin oxide regions between the ridges, which exhibit distorted semi-spherical curvatures of varying radii as shown in Figures 3.9 (b)-(c). This curvature increases the local electric field at the oxide/electrolyte interface, which in turn increases the oxide dissolution rate in this area. This leads to pore initiation as shown in Figures 3.9 (c)-(d).

3.4.5 Pore Development

At this stage, the pores consist of semi-spherical thin regions of oxide nucleating at random positions on the surface in between regions of thicker oxide. An important point to make is that the oxide growth kinetics requires the oxide to be of a uniform thickness in a direction perpendicular to the local surface. This can be seen by reviewing the thin film, high field limit for the current density in Eqn. 3.9 earlier in this paper. Essentially, Eqn. 3.9 can be rewritten as $i=A\exp(BV/d)$, where A and B are constants, V is the applied voltage and d is the oxide thickness perpendicular to the local surface. If a certain region of oxide is thinner than the rest (*i.e.* d is small), there will be less resistance to ionic migration and hence a faster growth rate will occur in this region until the oxide thickness catches up to the surrounding areas. A consequence of this is that the local geometry of the metal/oxide interface is then determined by the corresponding oxide/electrolyte interface. Therefore, a semi-spherical curvature at the oxide/electrolyte interface develops a semi-spherical curvature at the metal/oxide interface. At this point, the nucleated pores continue to widen and the radius of curvature at the bottom of the pores gets bigger due to a substantial lateral component of the electric field [36, 40]. This continues until the major pores meet their neighbors and the lateral fields cancel as

the scalloped areas merge. The steady state pore diameter and cell size are now established, and the pores can continue to propagate into the substrate by oxide growth at the metal/oxide interface and field-assisted dissolution of the oxide at the oxide/electrolyte interface. The cell walls no longer play a part in the growth process since the voltage drop (and hence all the growth and dissolution) takes place at the respective interfaces at the base of the pores. As the pores propagate into the substrate, the new material can only expand in the vertical direction, so that the existing cell walls are pushed upwards.

3.4.6 Steady State Growth

Under steady state conditions, when the voltage doesn't change with time, the resultant film parameters (pore diameter, cell size, etc.) do not change. Figure 3.10 shows a schematic illustrating the distribution of the electric field lines or equivalently the current lines in a pore. It can be seen that the field increases on passing from the cell base to the pore base. By assuming that the base of the pore is hemispherical, the amount the field increases from the cell base to the pore base can be measured approximately by the ratio of the cell base area to the pore base area [40]:

$$\sim \frac{(r+b)^2}{r^2} \qquad (3.11)$$

where r is the radius of curvature of the pore base and b is the barrier layer oxide thickness.

From this expression, it is possible to understand why the pore diameter remains stable under steady state conditions. For example, any tendency for the pore diameter to increase diameter as a result of an increased dissolution rate will result in the radius of

curvature of the pore base becoming larger. This increased radius of curvature then results in a decrease in the local field at the pore base and hence a reduced dissolution rate. Likewise, a decreased dissolution rate will result in a smaller radius of curvature. This smaller radius of curvature results in a larger electric field at the pore base, and increases the dissolution rate. Hence, a self-adjusting situation is set up where any tendency for the pore diameter to increase or decrease is held in check by a consequent increase or decrease in the radius of curvature at the pore base which determines the local field [36, 40]. Essentially, for a given voltage in steady state, oxide growth occurs at a constant rate determined by the average field. It is balanced by field-assisted dissolution, whose rate is determined by the local field, which in turn is determined by the radius of curvature of the pore base.

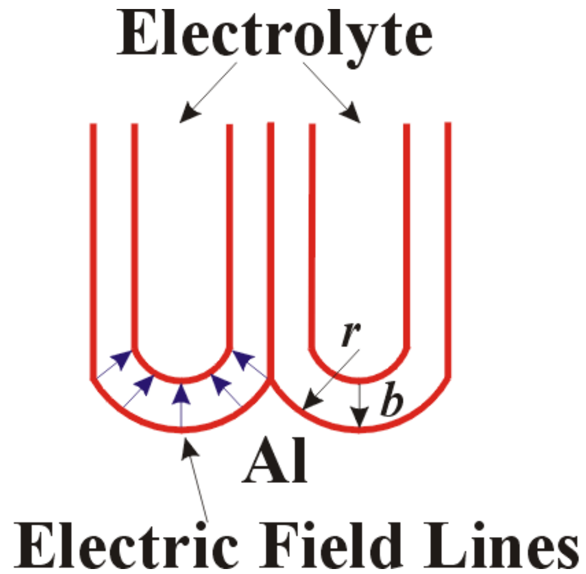

Figure 3.10. Schematic representation showing the distribution of field lines in porous alumina.

A theoretical modeling of porous oxide growth on aluminum was first attempted in a 1992 paper by V. P. Parkhutik and V. I. Shershulsky [47]. To start, equations are set up for the current density and hence the propagation rates at the two interfaces, taking into account the growth and dissolution of the oxide. To analyze the steady state condition at the bottom of the pores, they assume that the barrier layer thickness remains constant and the radius of curvature at the base of the pore remains unchanged. This analysis enables them to plot a function of the radius of curvature of the pores versus the

electric field at the oxide/electrolyte interface. The result is that for very large changes in the pore geometry, the surface electric field is practically unchanged during steady state pore growth. Next, by assuming that both of the oxide boundaries at the bottom of the pore can be represented as concentric hemispheres, an expression relating the cell size (and pore radius) to the applied voltage can be found. The cell size and radius are both found to be linearly dependent on the applied voltage In accordance with experimental results where it is found that the pore diameters can vary from about 5 nm to 500 nm by varying the forming voltage. Figure 3.11 shows a plot of the cell size or interpore distance versus the applied voltage [47]. The straight line is the theoretical fit from their model while the points are experimental data from films grown in various electrolytes. The agreement is found to be quite good. Their conclusions are that the proportionality between the pore size and the voltage is of a quite general nature and is not sensitive to the particular features of pore shape.

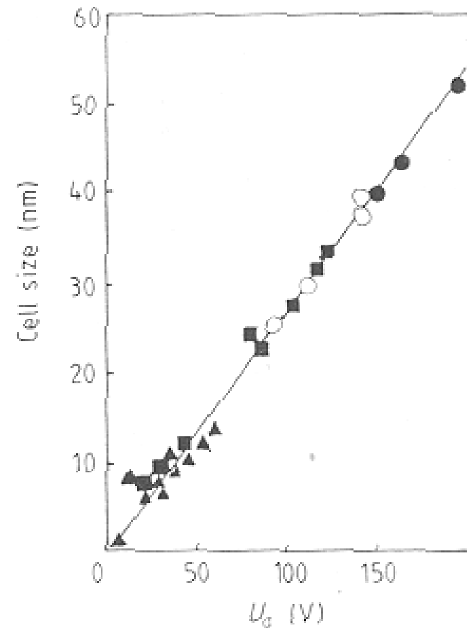

Figure 3.11. The theoretical dependence of cell size versus applied voltage (straight line) compared with experimental data of different electrolytes (triangle, oxalic acid; square, phosphoric acid; open circle, glicolic acid; closed circle, tartaric acid). Graph taken from Ref. [47].

3.4.7 Ordered Growth

For the most general processing conditions of porous alumina, the resulting structure is a random array of pores. Examples of unordered films grown in 0.3 M phosphoric acid are shown in the secondary electron microscope (SEM) images in

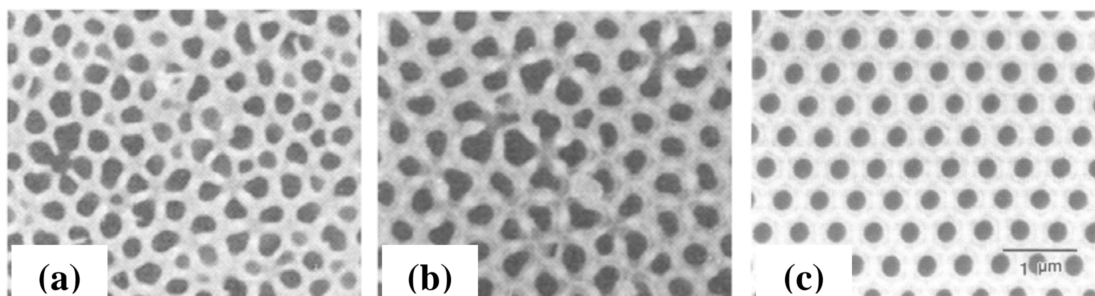

Figure 3.12. SEM micrographs of porous alumina films formed in 0.3 M phosphoric acid at 0°C for 16 hours. The unordered films in (a) and (b) were formed in 150 V and 180 V, respectively. The ordered film shown in (c) was formed in 195 V. The scale for all three micrographs is given in (c). Images taken from Ref. [48].

Figures 3.12 (a) and (b) for forming voltages of 150 V and 180 V, respectively [48]. However, in 1995, a Japanese group found that under the right processing conditions, namely the appropriate forming voltages (specific for each electrolyte) and very long anodization times, the pores would self order into a hexagonally close packed array with well ordered domains several microns in size [49, 50]. Figure 3.12 (c) shows an SEM micrograph of an ordered porous alumina film formed in 0.3 M phosphoric acid at 195 V for 16 hours [48].

While it is not yet known what causes the alumina membranes to spontaneously order under the right processing conditions, there are a number of conditions that are known to affect the degree to which the films will order. In addition to the two most important parameters (voltage and time), the electrolyte concentration, stirring of the electrolyte, temperature, and substrate preparation all play an important part in the ordering process [51-54]. When these conditions are suitable, the result is a stable anodic state, i.e., stable voltage and current, which is found to be an essential requirement for the ordering process to occur [51].

One possible explanation for the ordering of the pores was put forward by a German group in 1998 [55]. They state that the self-organized arrangement of

neighboring pores can be explained by a repulsive interaction between the pores. A possible origin of the forces between neighboring pores was proposed to be the mechanical stress associated with the expansion during oxide formation at the metal/oxide interface. Figure 3.13 shows a schematic depicting the expansion of aluminum during oxidation [55]. While all the O^{2-}/OH^- ions reaching the metal/oxide interface are involved in growth processes, the Al^{3+} ions reaching the oxide/electrolyte interface are all ejected into the electrolyte. By varying the voltage and electrolyte, the amount of aluminum going into forming the oxide can be varied. Essentially, the relative transport numbers of Al^{3+} and O^{2-}/OH^- ions through the film is a function of the voltage and electrolyte, which varies the stress at the metal/oxide interface. To measure this experimentally, films were grown for long anodization times in various voltages and electrolytes, and the volume expansion was measured. The volume expansion factor was simply calculated by measuring the ratio of the relative thickness of the alumina layer grown to the aluminum consumed, and was found to vary from about 0.8 to 1.7 by varying the anodization conditions. It was found that maximum ordering was achieved whenever the anodization conditions lead to moderate volume expansion factors of 1.4. The primary parameter found to give this expansion factor was a narrow range of

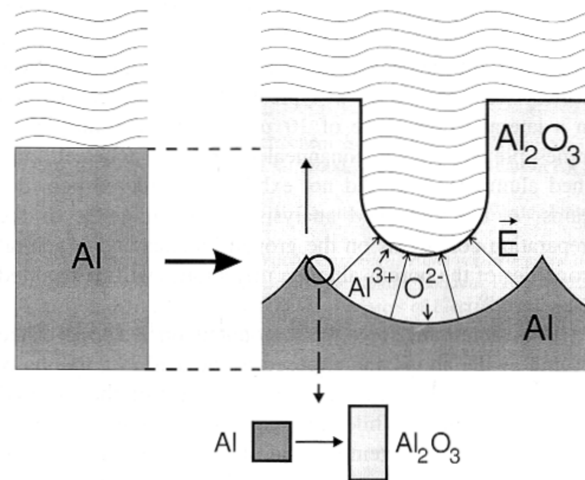

Figure 3.13. Schematic of the expansion of Al during anodic oxidation. On the left, the level of the unoxidized metal surface is depicted. Schematic taken from Ref. [55].

anodizing voltage which was dependent on the electrolyte and electrolyte concentration used.

In the case of contraction (i.e. volume expansion factors less than one), no repulsive forces between the pores are expected, and experimentally no ordered domains were observed. As the volume expansion rose above one, small ordered domains were observed. At moderate volume expansion factors of about 1.4, maximum ordering was observed with ordered domains of about a micron in size separated by grain boundaries where a large amount of defects also occurred. It was found that for larger volume expansion factors, structural defects and irregular pore growth occurred, which were often characterized by unstable currents. In addition, large volume expansion factors were associated with high anodizing voltages and large growth rates which serve to reduce the interaction between the neighboring pores.

It is important to note that ordering of the pores occurs through time at the metal/oxide interface. Under the appropriate anodization conditions leading to a moderate expansion of the oxide, the pores still initiate at random positions on the oxide surface and only became progressively ordered at the metal-oxide interface through time. As mentioned above, the appropriate anodization conditions for good ordering of the pores is mainly determined by the anodization voltage specific to the electrolyte and electrolyte concentration. When these parameters are chosen such that they give expansion factors between 1.2-1.4, or equivalently a porosity of about 10%, well ordered pore arrays result after long anodization times. This observation has lead to the so called "10% porosity rule" [56] which states that the self-ordering of the AAO pores with any interpore spacing is possible as long as the anodization voltage combined with the pH of

the electrolyte is tuned to give an AAO film with 10% porosity.

As a final comment, it should be noted that very well ordered arrays with no grain boundaries can be fabricated over large areas (~ 5 mm^2 or larger) by texturing the surface of the starting Al foil with an array of concave pits and anodizing under the appropriate conditions [57, 58]. These dimples serve as ordered nucleation sites for the pores rather than the random pore initiation sites that occur without texturing.

3.5. EXPERIMENTAL RESULTS AND DISCUSSION

The following section presents work on optimizing the growth of AAO films specifically for use as templates or masks for the fabrication of arrays of nanostructures To start, the Al foil growth substrates were subjected to various pre-growth processes to optimize the growth of the AAO films. Following this, examples of porous AAO films obtained under different growth conditions (various electrolytes, low temperature growth, and evaporated Al on silicon substrates) are reported and discussed with an emphasis towards tailoring the pore dimensions, spacings, thickness, etc.

3.5.1 Al Foil Pre-Treatment Study

High purity (99.999%), 0.25 mm thick aluminum foils were degreased in tetrachloroethylene (TCE), acetone, methanol, and DI water, followed by a cleaning step consisting of a 1:10:20:69 mixed solution of hydrofluoric acid (HF), nitric acid (HNO_3), hydrochloric acid (HCl), and water (H_2O) at 25 ^oC for five minutes. Figure 3.14 (a) shows a Nomarski optical microscope image of a cleaned Al foil while Figure 3.14 (b) shows an SEM image of the same sample. Note the presence of square defects in the SEM image. Following the degreasing, the Al foils were annealed under forming gas

(80% N_2, 20% H_2) at 550 ^oC for three hours to remove mechanical stresses in the film and increase grain sizes. Figure 3.14 (c) shows a Nomarski optical microscope image of an annealed Al foil while Figure 3.14 (d) shows an SEM image of the sample. Note the density of square defects in the annealed foil is smaller than in the unannealed foil. To further reduce the surface roughness of the films, the Al substrates were electropolished in a 1:3 mixture of perchloric acid ($HClO_4$) and ethanol (C_2H_5OH) for three minutes at a constant current density of 100 mA/cm^2 and a temperature of 2 ^oC. This was accomplished using a temperature-controlled anodization cell similar to the schematic in Figure 3.1 using a Pt cathode. The back and sides of the Al foils were coated in black wax to prevent any back side electropolishing or anodizing as well as to eliminate any edge effects. The electropolishing step produced a mirror surface as shown in the Nomarski optical microscope and SEM images, Figures 3.14 (e) and (f), respectively.

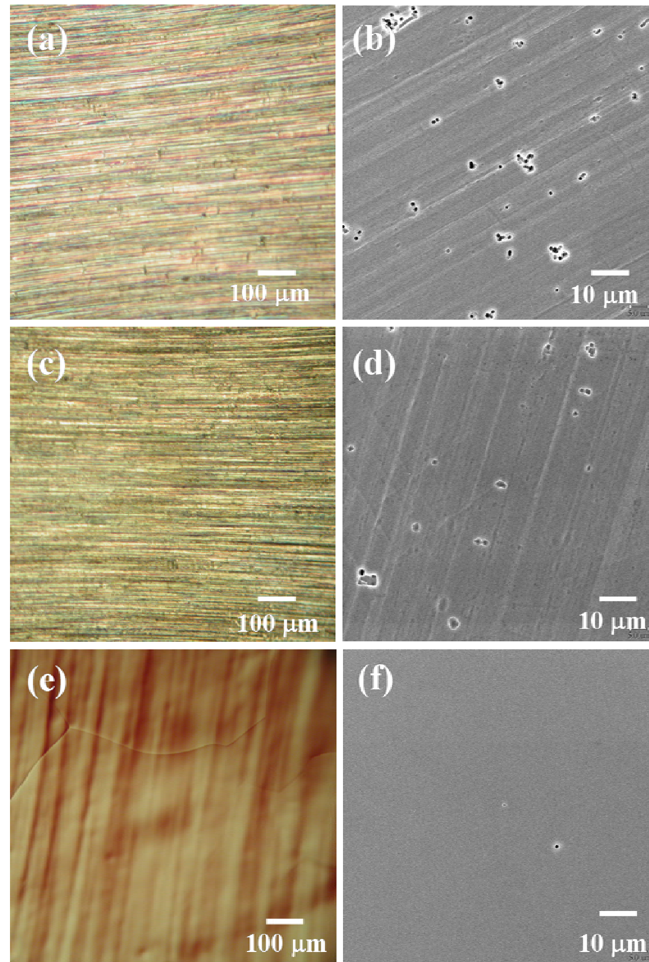

Figure 3.14. (a) Nomarski optical microscope image of degreased and acid cleaned, high purity Al foil. (b) SEM image of degreased and acid cleaned, high purity Al foil. (c) Nomarski optical microscope image of annealed Al foil. (d) SEM image of annealed Al foil. (e) Nomarski optical microscope image of annealed and electropolished Al foil. (f) SEM image of annealed and electropolished Al foil.

Note that the electropolishing step has clearly defined the grain boundaries as seen in the optical microscope image while the SEM image indicates that most of the square defects are gone.

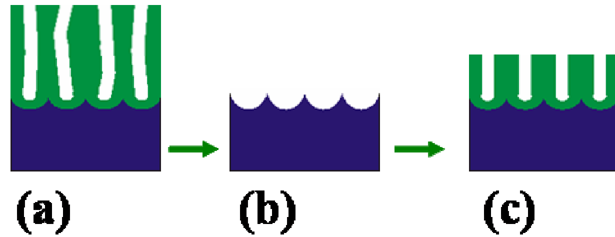

Figure 3.15 Process schematic for fabricating a well-ordered AAO film. (a) Long period anodization of Al foil to obtain well-ordered pores at the metal/oxide interface. Pore initiation on the top surface of the AAO film is random. (b) Etch off resulting AAO film leaving behind pore base replica in Al foil (c) Short period re-anodization of Al foil to fabricate well-ordered, thin film with straight pore channels.

At this point, the pre-treatment of the Al foils was complete and they were ready for anodization. To maximize ordering of the pores in the AAO, a two step anodization process similar to that reported by Masuda was used [59]. In this process, a long first anodization step (generally greater than 12 hours) at the appropriate constant voltage that maximizes the self-organization process (specific to each electrolyte) is performed to insure good ordering at the metal-oxide interface. As previously mentioned, the pores initiate at random positions and self-order at the metal-oxide interface through time. This is shown schematically in Figure 3.15 (a). The porous AAO film is then stripped off leaving behind periodic concave patterns in the Al surface as depicted in Figure 3.15 (b). These ordered arrays of dimples serve as nucleation sites for the second anodization step insuring maximum ordering from the outset. This allows the growth of a porous AAO film with uniform and straight pore channels (Figure 3.15 (c)), a requirement if the film is to be used as a mask or template for pattern transfer.

Figures 3.16 (a) and (b) show Nomarski optical microscope and SEM images of the top surface of a porous AAO film after a first anodization at a constant voltage of 40 V in 0.3 M oxalic acid ($C_2H_2O_4$) for 15 hours at 5 ^oC. The anodization conditions were

designed to maximize the ordering at the metal-oxide interface as determined by previous researchers [49, 52]. Note the random orientation of the pores and the large variation in both pore diameter and spacing in the SEM image reflecting the random pore initialization at the start of the anodization. Next, the porous AAO film was etched off in a 1:1 mixture of 6 wt % phosphoric acid and 1.6 wt % chromic acid at 60 ^{o}C. This left behind periodic concave patterns in the Al surface that served as nucleation sites for the second anodization step to insure maximum ordering from the outset. The second anodization step was conducted at a constant voltage of 40 V in 0.3 M oxalic acid for five minutes at 5 ^{o}C. Figures 3.16 (c) and (d) show Nomarski optical microscope and SEM images of the top surface of the porous AAO film after the second anodization step. Note the very well ordered hexagonally close packed array of pores in the SEM image. The pores have an average diameter around 40 nm with 100 nm pore-to-pore separation.

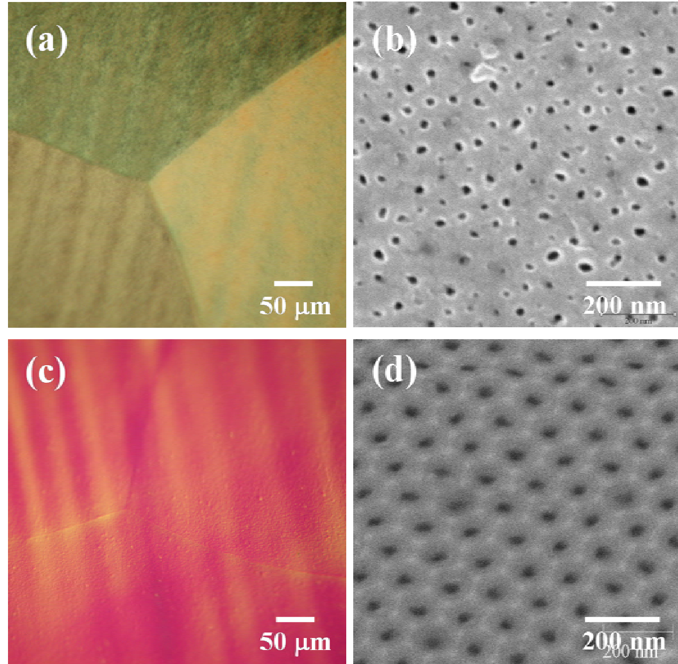

Figure 3.16. (a) Nomarski optical microscope image of porous AAO film after first anodization. (b) SEM image of porous AAO film after first anodization. (c) Nomarski optical microscope image of porous AAO film after second anodization. (d) SEM image of porous AAO film after second anodization.

3.5.2 Porous AAO Film Results

Anodization of films in both 0.3 M oxalic acid and 1.7 wt % sulfuric acid were conducted under constant voltage conditions. Unless otherwise specified, the pre-

treatment of the Al foils was identical to that described above. Figure 3.17 shows a typical current vs. time curve for a first anodization of an 8 mm x 8mm AAO film anodized at a constant voltage of 40 V in 0.3 M oxalic acid for roughly 20 hours at 5 °C. The current initially starts our high, immediately decreases, goes through a minimum, climbs to a local maximum at around 5 minutes, and remains relatively constant for the rest of the anodization. Note that this curve agrees qualitatively with the constant voltage curve typical for porous AAO films as shown in Figure 3.6.

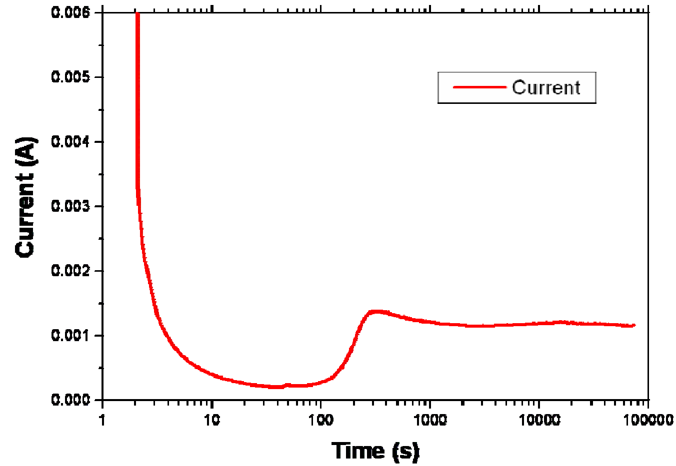

Figure 3.17 Typical current vs. time curve for a porous AAO film anodized at a constant voltage of 40 V in 0.3 M oxalic acid for approximately 20 hours at 5 °C.

Figure 3.18 shows SEM images of two films anodized in oxalic acid, and sulfuric acid. Figure 3.18 (a) shows a top down SEM image of a film anodized at 40 V in 0.3 M

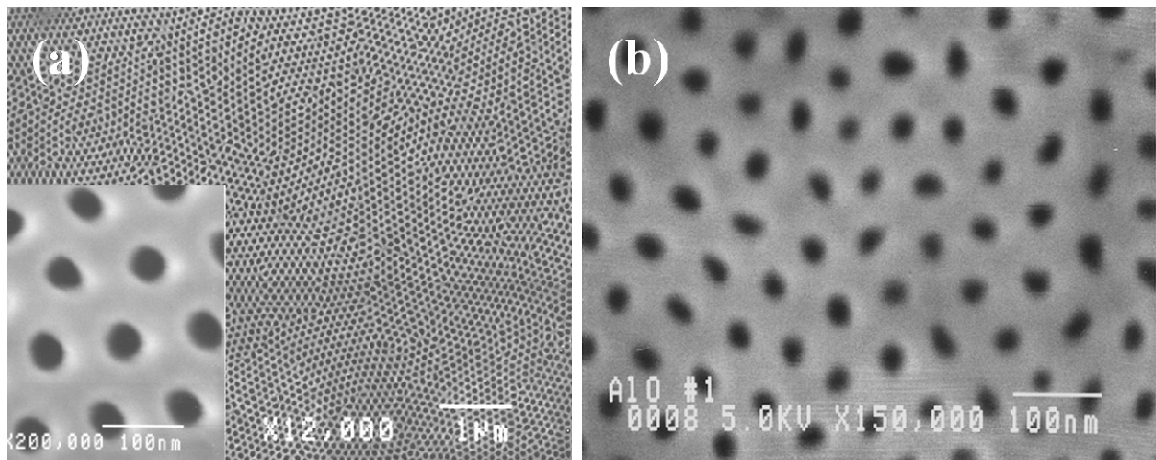

Figure 3.18. (a) SEM micrograph of porous AAO film anodized at 40V in 0.3M oxalic acid at 5°C. Inset shows higher magnification SEM image. (b) SEM micrograph of porous AAO film anodized at 27 V in 1.7 wt% sulfuric acid at 5°C.

oxalic acid at 5 °C for approximately 20 hours. After anodization, the AAO film was removed from the Al foil in a saturated mercury chloride solution, and the barrier layer was removed in a 5 wt % phosphoric acid solution for 35 minutes. The SEM image shows the well-ordered side of the AAO film after the first anodization. The inset shows a higher magnification SEM image. The AAO film has an average pore diameter of 40 nm with a pore-to-pore spacing of 100 nm. Note that the film has a polycrystalline structure with micron-sized domains. Figure 3.18 (b) shows a top down SEM image of a film anodized at 27 V in 1.7 wt % sulfuric acid (H_2SO_4) at 5 °C for approximately 20 hours. Like the oxalic acid-grown sample, the AAO was removed from the Al foil in a saturated mercury chloride solution, and the barrier layer was removed in a 5 wt % phosphoric acid solution for 35 minutes. This film has an average pore diameter of 20 nm with a pore-to-pore spacing of 60 nm.

The average diameters and pore-to-pore spacings agree well with the work of others as seen in Figure 3.19 which plots the linear relationship between the interpore spacing and the applied voltage for films grown in different electrolytes [52].

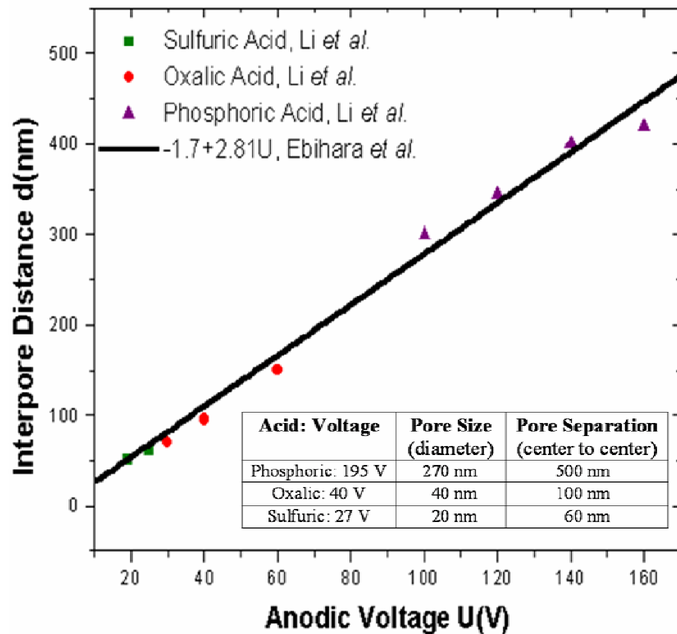

Acid: Voltage	Pore Size (diameter)	Pore Separation (center to center)
Phosphoric: 195 V	270 nm	500 nm
Oxalic: 40 V	40 nm	100 nm
Sulfuric: 27 V	20 nm	60 nm

Figure 3.19. Interpore distance versus applied voltage for porous AAO films grown in sulfuric acid, oxalic acid, and phosphoric acid electrolytes. Inset table shows the pore diameters and interpore separations for the three electrolytes under the conditions that maximizes the ordering of the pores. Data taken from Ref. [52].

The inset table shows the pore diameters and interpore spacings for the three most common electrolytes centered around the narrow voltage window that maximizes ordering.

The use of these porous AAO films as templates or shadow masks for the fabrication of arrays of nanostructures requires that the pore channels be straight and uniform (no kinks,etc.) and that the AAO film thickness be small enough to allow pattern transfer to occur. The use of a two step anodization process [59] insures the uniformity of the pore channels and allows the thickness to be tailored to the desired value by the second anodization time. Figure 3.20 shows a near cross-sectional SEM image of a 40 V, 0.3 M oxalic acid-grown AAO film after a second anodization time of 5 minutes. The AAO was removed from the Al substrate by a saturated mercury chloride

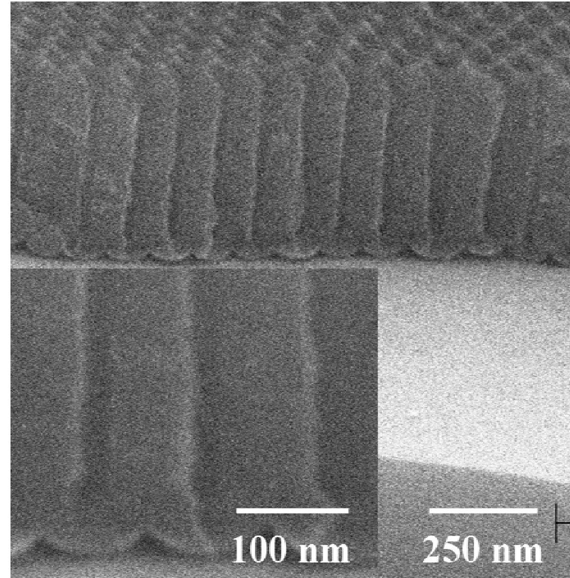

Figure 3.20. Near cross-sectional SEM image of oxalic acid-grown AAO film removed from the Al foil and lifted out onto a silicon substrate. Inset shows a higher magnification cross-sectional SEM image of the barrier layer.

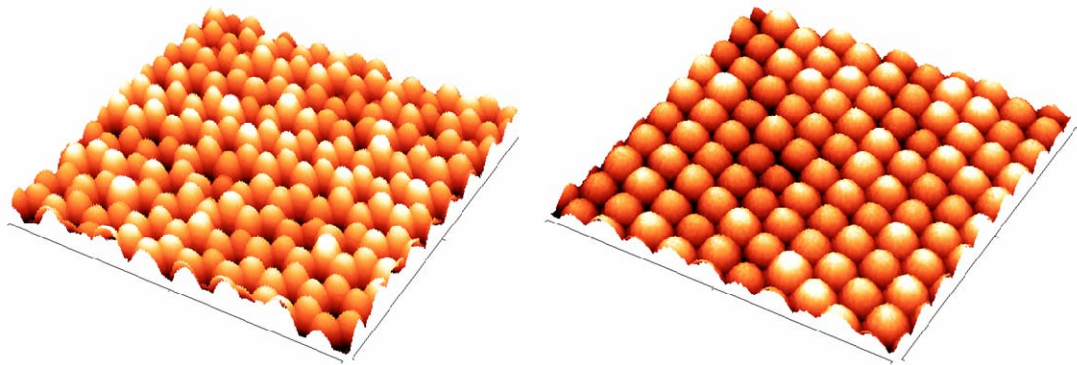

Figure 3.21. 1 μm x 1 μm, 3D-rendered atomic force microscopy images of an oxalic acid-grown AAO porous side up (a) and barrier layer side up (b). Color scale for both images is approximately 15 nm.

solution and lifted out onto a silicon substrate. Note the straightness and uniformity of the pores. The inset of Figure 3.20 shows a higher magnification cross-sectional SEM image of the barrier layer. For comparison, Figures 3.21 (a) and (b) show 1 μm^2, 3D rendered, non-contact atomic force microscopy (AFM) images taken with a Topometrix TMX 2000 Explorer system of the top side of a porous AAO film (a) and the bottom barrier layer side (b) of an AAO film grown under similar conditions to the film shown in Figure 3.20. The color scale for both of the images is 15 nm. To use these porous AAO films as through-hole masks, the barrier layer needs to be removed from the bottom side of the film. This will be discussed in detail in Chapter 4.

Control over the thickness of the AAO films is also a requirement for the use of these films as templates or shadow masks. For a given a temperature and anodization voltage, the AAO thickness depends on the anodization time of the second anodization.

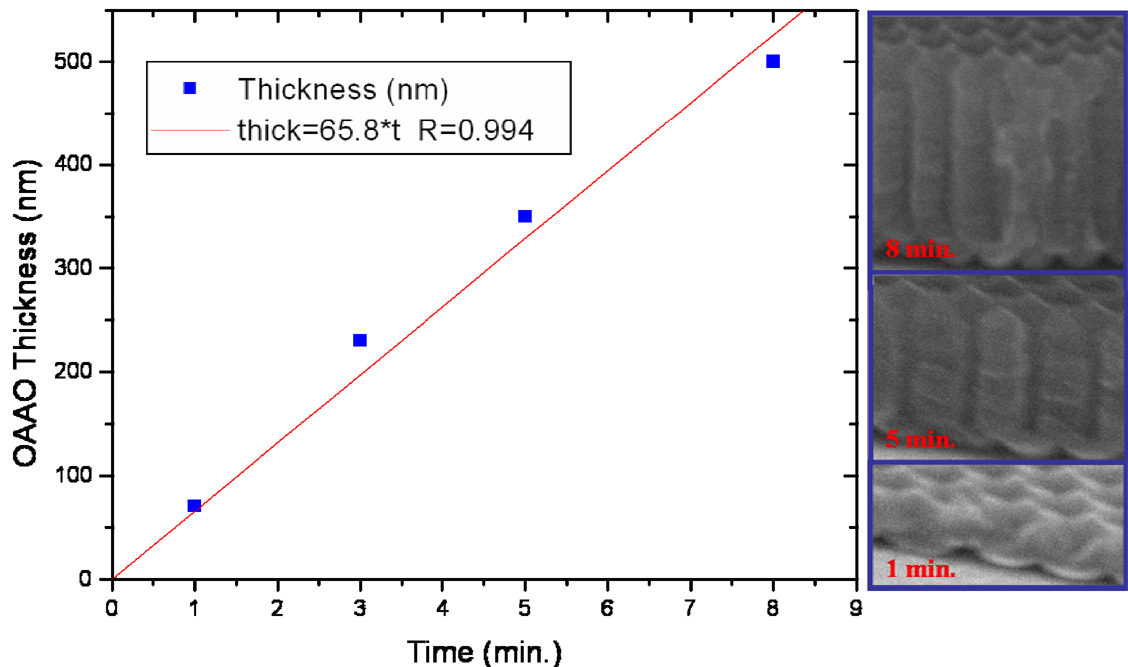

Figure 3.22. AAO film thickness vs. secondary anodization time for films grown in 0.3 M oxalic acid at 40 V and 2 °C. Images on the right show 60° oblique angle SEM micrographs of AAO films grown for 1 minute, 5 minutes, and 8 minutes.

Figure 3.22 shows the thickness versus anodization time for secondary anodizations performed at 40 V in 0.3 M oxalic acid at 2 ^{o}C. A straight line fit through the data gives a growth rate of approximately 66 nm/min under these conditions. The right hand side shows oblique angle SEM views (60° from normal) of AAO films for second anodization times of 8 minutes, 5 minutes, and 1 minute. Note that the 1 minute film has very little thickness other than the barrier layer thickness. These results are specific to the anodization conditions, *i.e.* 0.3 M oxalic acid at 40 V and a temperature of 2 ^{o}C. These results would vary for other anodization conditions.

3.5.3 Low Temperature Porous AAO Film Results

It has previously been reported that anodization of Al carried out at low temperatures (~0 to -80 ^{o}C) in sulfuric/methanol electrolytes can produce unordered pore arrays with smaller pore diameters and spacings than those found in AAO films carried out above 0 ^{o}C [60]. Towards this end, an anodization of Al was performed at 15V and -32 ^{o}C in a 3:1 mixture of 1.2 M H_2SO_4 and water for 48 hours. The addition of methanol in the electrolyte was to insure that the electrolyte did not freeze during the low temperature anodization and a long anodization time was required because of the much

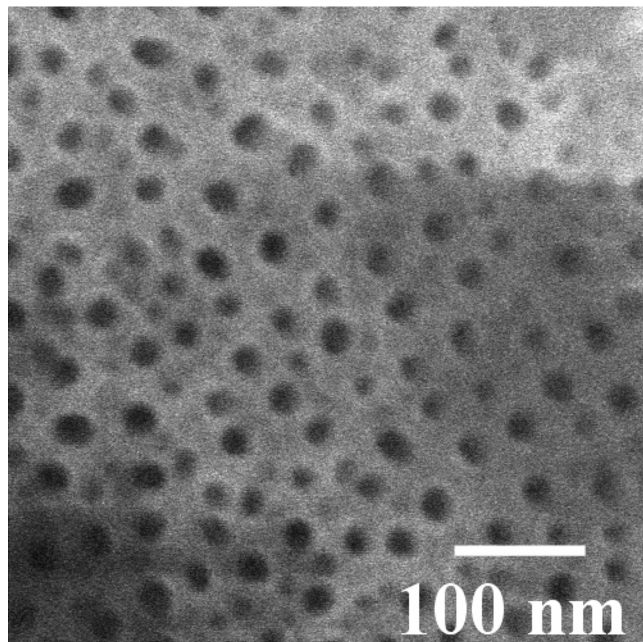

Figure 3.23. Porous AAO film grown in a 1:1 mixture of 1.2M sulfuric acid: MeOH at 15V and -32°C.

slower growth rate at low temperatures. Figure 3.23 shows an SEM image of the resulting porous AAO film. Note that the pores are not well ordered and the pore diameters, ranging from about 10-22 nm, are not uniform. At this time, it is unknown if low temperature anodization of Al can lead to a well ordered pore array and if possible, what conditions are required. Although the pore sizes are smaller than room temperature anodizations, this line of research was abandoned due to the disordered array and impracticality of anodizing for several days to achieve an AAO film for pattern transfer.

3.5.4 Evaporated Al on Si Porous AAO Results

As a means of exploring a way to produce a porous AAO film on a silicon substrate, work was performed on anodizing thermally evaporated Al on Si films following the work of Crouse et al [61]. First, a 2 μm thick film of 99.99% Al was thermally evaporated in a vacuum of 8 x 10^{-7} Torr on a 1-10 ohm cm n-type Si substrate. The Si backside and edges were coated in black wax and the Al film was anodized in 0.3 M oxalic acid at 40 V at 5 °C. After roughly 13 minutes, the Al film was seen to change color and the current decreased substantially. The film was then subjected to a pore widening etch consisting of a 5 wt % solution of phosphoric acid at 30 °C for 1 hour. Figure 3.24 (a) shows an 11° from normal SEM image of the porous AAO film. The

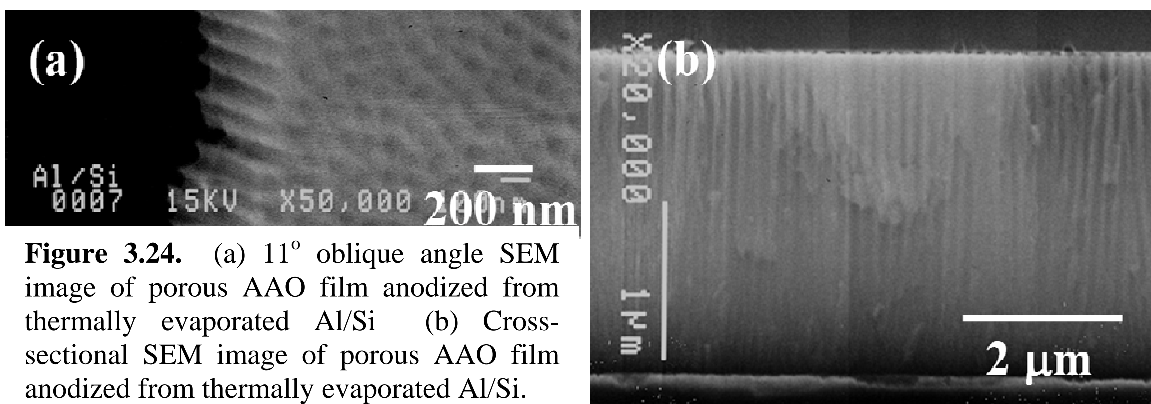

Figure 3.24. (a) 11° oblique angle SEM image of porous AAO film anodized from thermally evaporated Al/Si (b) Cross-sectional SEM image of porous AAO film anodized from thermally evaporated Al/Si.

pores are roughly 80 nm in diameter (due to the pore widening step) spaced 100 nm apart. Figure 3.24 (b) shows a cross-sectional SEM image of the porous AAO film. As can be seen from Figure 3.24 (a), the pores were not very well ordered due to the use of only one short period anodization step (limited by the thicknesss of the evaporated Al film). To obtain better ordering, it is possible to utilize a two step anodization on a thicker evaporated Al film or to imprint the Al film prior to anodization. In fact, both of these techniques have been used by research groups to achieve better pore ordering [62, 63].

3.6. CONCLUSION

The growth mechanisms and previous work regarding AAO films was reviewed. Essentially, the growth of porous alumina proceeds by oxide growth at the metal/oxide interface dictated by the average field, and field-assisted dissolution at the oxide/electrolyte interface dictated by the local field which is influenced by the radius of curvature at the pore base. The constant pore diameters, which are proportional to the applied voltage, result from the equilibrium barrier layer thickness and the pore base radius of curvature subsequently established. As a result, pore diameters are proportional to the applied voltage and are tunable anywhere from about 5 nm to 500 nm. In addition, ordering of the pores into a hexagonal close packed array can occur under the appropriate anodizing conditions, the most important of which are narrow voltage windows specific to the electrolyte and long anodization times. Although at present, the mechanism of ordering has not been fully elucidated, it is thought to result from repulsive forces between neighboring pores as a result of stress at the metal/oxide interface.

Because of the unique structure of porous alumina membranes, many applications of this film are possible, including its use as a nano-template to create ordered arrays of nanostructures. Towards this end, porous AAO films designed to maximize its use as a nano-template were grown and characterized. AAO films grown in oxalic acid (40 nm pore diameters, 100 nm interpore spacing), and sulfuric acid (20 nm pore diameters, 60 nm interpore spacing) were fabricated at the appropriate voltages to maximize the self-ordering of the pores. In addition, low temperature anodizations were carried out in sulfuric acid to produce unordered arrays of pores with pore diameters ranging from 10-20 nm. Finally, anodizations were carried out on thermally evaporated Al/Si to produce AAO templates grown on silicon substrates.

Chapter 4

Pattern Transfer with AAO: Nano-Dot Arrays

4.1. ABSTRACT

Nano-dot arrays of a wide range of materials have been fabricated onto various substrates by evaporating or sputtering material through AAO films. Depending on the dot and substrate materials, nano-dot arrays could have a wide variety of applications such as data storage (*i.e.* magnetic memory storage), or nano-tribological coatings to improve the friction, lubrication, or wear of surfaces. In addition, the fabrication technique presented allows large areas to be patterned (~ mm x mm) which is essential for certain characterization techniques (*i.e.* optical and magnetic measurements, *etc.*) First, the pattern transfer technique using AAO films as masks will be described. In short, the AAO films, after removal from the Al foil and removal of the thin barrier layer, are placed directly onto substrates and used as shadow masks or templates during an evaporation or sputter-deposition step. After material deposition and upon removal of the AAO film, a well-ordered hexagonal array of nano-dots with lateral dimensions

comparable to the pore dimensions of the AAO is obtained. Next, various examples of dot arrays both evaporated and sputter-deposited will be presented. Finally, characterization by UV-Vis absorption spectroscopy on Au nano-dot arrays showed peaks in the 500-600 nm region, qualitatively consistent with Mie scattering and absorption phenomena for nano-dots of this size.

4.2. PATTERN TRANSFER TECHNIQUE

As discussed in the previous chapter, sample processing starts with an AAO template fabricated using a two-step anodization process on a pure (99.999%) Al foil following the work of Masuda et *al.* [59]. Figure 4.1 shows a schematic of the processes involved in fabricating a through-hole mask from a porous AAO film. First, a long period anodization step on the order of 15 hours is performed on an Al foil as shown in Figure 4.1 (a). The purpose of this step is to insure maximum ordering of the pores since, as shown in Chapter 3, the base of the pores become more ordered in time under the appropriate electrolyte-specific anodization voltage. This step is followed by etching off the AAO film in a 1:1 mixture of 6 wt % phosphoric acid: 1.8 wt %chromic acid at 60 ^{o}C for two hours. This leaves behind a replica of the pore bottoms in the Al foil as shown in Figure 4.1 (b). The aluminum foil is then re-anodized under identical conditions as the

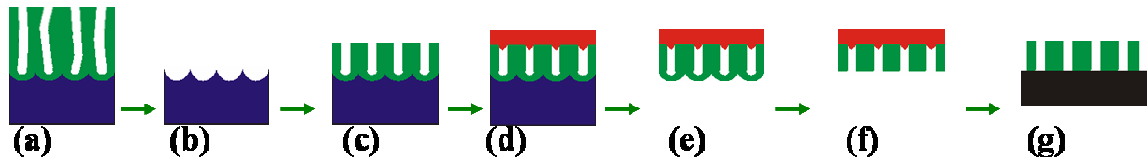

Figure 4.1. Process schematic for fabricating a through-hole porous AAO mask. (a) Long period anodization of Al foil (b) Etch off resulting AAO film leaving behind pore base replica in Al foil (c) Short period reanodization of Al foil (d) Spin on collodion coating to protect top surface of AAO (e) Remove Al foil in saturated $HgCl_2$ solution (f) Etch away barrier layer in 5 wt% phosphoric acid (g) Lift off AAO film onto desired substrate and remove collodion in acetone.

first anodization but for a much shorter period (~5 minutes), giving a thin porous AAO film with maximized pore ordering and straight pore channels as shown in Figure 4.1 (c). This completes the growth of the AAO film and it is now ready to be lifted off and further processed into a through-hole mask following the procedure first laid out by Masuda et *al.* [59]. First, a thin polymer film consisting of collodion in amyl acetate is spun onto the surface of the AAO film to protect it from further processing steps. This is shown in Figure 4.1 (d). Next, a saturated $HgCl_2$ solution is used to separate the AAO from the Al foil as depicted in Figure 4.1 (e). The remaining AAO barrier layer is then removed in a 5 wt % solution of H_3PO_4 at 30 ^oC for 35 minutes leaving a through-hole mask as shown in Figure 4.1 (f). The resulting AAO through-hole mask, which was roughly 3 mm by 3 mm in size for the work performed here, is then placed on the desired substrate and the collodion layer is removed in acetone. The resulting sample is then ready for subsequent pattern transfer (e.g. deposition or etching processes) as shown in Figure 4.1 (g).

4.3. THERMALLY EVAPORATED NANO-DOT ARRAYS

4.3.1 MgF_2 Nano-Dot Array using Oxalic Acid-Grown AAO Mask

An AAO film was fabricated by a two step anodization process as described above. First, the film was anodized in 0.3 M oxalic acid at 40 V and 10 ^oC for 15 hours. The AAO film was stripped from the Al foil and a secondary anodization in 0.3 M oxalic acid at 40 V and 10 ^oC for 5 minutes was carried out. This resulted in an AAO film approximately 500 nm thick with 50 nm pore diameters spaced 100 nm apart. Next, the processing steps shown in Figure 4.1 (d)-(g) were carried out to make a through-hole

mask. In particular, a thin layer of collodion was spun onto the AAO film and the film was separated from the Al foil in a saturated $HgCl_2$ solution. Next, the barrier layer was removed in a 5 wt % solution of H_3PO_4 at 30 ^oC for about 35 minutes. This was followed by lifting off the AAO film onto a Si substrate and allowing the film to dry before immersing the sample in acetone to remove the collodion layer. This resulted in a through-hole AAO mask approximately 3 mm x 3 mm in size weakly bonded by van der Waal forces to a Si substrate.

Next, a 50 nm layer of MgF_2 was deposited onto the Si through the AAO mask by thermal evaporation using an Edwards E306A in a vacuum of ~ 10^{-6} Torr. The source material, consisting of a 5 mm x 5mm x 2mm piece of MgF_2, was placed directly underneath the sample with a sample-to-source distance of approximately 10 cm. This allowed a significant fraction of the evaporated MgF_2 (with an estimated angular dispersion of ~ 100 mm/5 mm = 20:1) to travel down the pores of the mask (which had an aspect ratio of 500 nm/50 nm = 10:1 and hence could accept angular dispersions up to 10:1). Unless otherwise stated, all other evaporations used to create nano-dot arrays as described later in this chapter were performed under identical conditions. After evaporation, the AAO film was removed by mechanical means (i.e., double-side carbon tape was used to removed the AAO) although it should be noted that chemical wet etching compatible with the dot material was also used to remove AAO films from other samples.

Figure 4.2 shows SEM micrographs taken with a JEOL 880 SEM of the resulting MgF_2 dot array on the Si substrate. The dots have an average diameter of 50 nm with an average center-to-center spacing of 100 nm. From the low magnification SEM image in

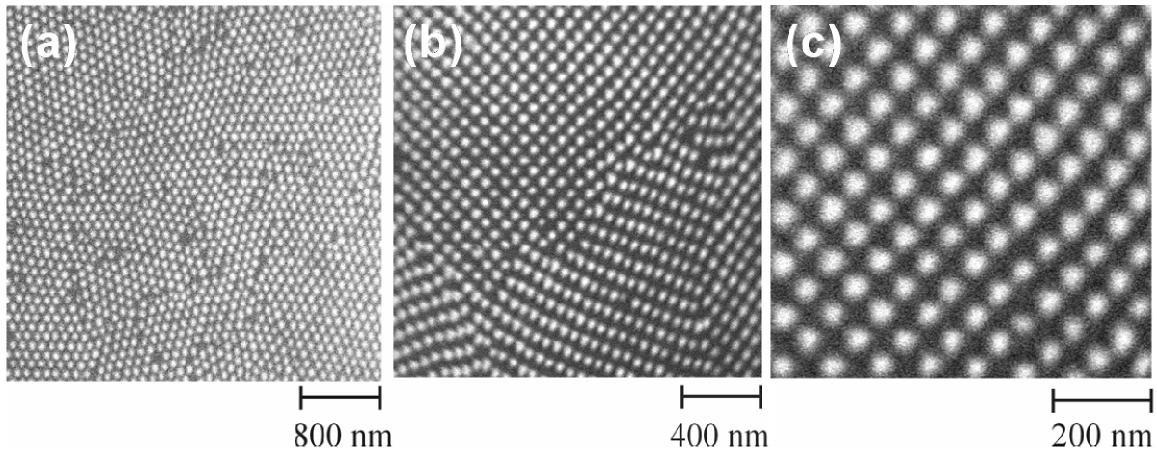

Figure 4.2. Top down SEM micrographs of array of MgF_2 nano-dots thermally evaporated through a porous AAO mask onto a Si substrate. (a) Low magnification SEM showing presence of grain boundaries and missing dots (b) Medium magnification SEM (c) High magnification showing a very well-ordered region.

Figure 4.2 (a), it can be seen that the hexagonal arrangement of the dots corresponds well with the hexagonal arrangement of the pores in the AAO mask. The regularity or degree of ordering of the dots depends on the degree of ordering of the pores in the AAO film and as discussed in the last chapter is highly dependent on the anodization conditions. As seen in both Figures 4.2 (a) and (b), grain boundaries separate the well-ordered micron-sized regions. In addition, point defects and missing dots can be seen. The missing dots are most likely due to the presence of dust or particles blocking the pores in the AAO mask during the evaporation or MgF_2 clumping or balling up on the surface of the AAO mask and subsequently blocking the pores during the evaporation step. Figure 4.2 (c) shows a close-up SEM in a region exhibiting very good order.

Figure 4.3 (a) shows a 500 nm x 500 nm 3D-rendered non-contact AFM image taken with a Topometrix TMX 2000 Explorer system of the MgF_2 dot array while Figure 3 (b) shows a line scan taken through the black line crossing the AFM image. A bulk evaporation of 50 nm (as determined by a crystal monitor and bulk step height measurements) of MgF_2 yielded an average dot height of 12 nm +/- 11%. The difference

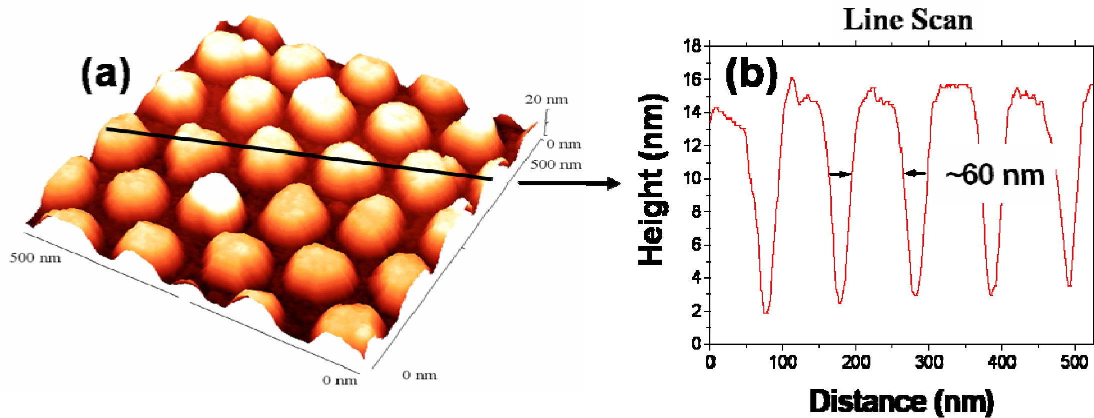

Figure 4.3. (a) 3D rendered AFM scan showing hexagonal array of thermally evaporated MgF_2 nano-dots. (b) Line scan of dots taken from the black line crossing the AFM scan in (a).

in the deposition thickness and the dot height is assumed to be due to MgF_2 material coating the top and side of the pores of the AAO mask yielding a material transmission factor through the 10:1 aspect ratio pores of 24 %. The shape of the dots in this case is roughly spherical with a flat base. The average dot diameter as determined from AFM linescans was found to be 60 nm +/- 9 % with an average center-to-center dot spacing of 110 nm +/- 5 %. The diameter and spacing dimensions determined from AFM scans are slightly larger than those determined from the SEM micrographs and the known dimensions of the AAO mask (50 nm diameter pores spaced 100 nm apart). This difference in the lateral dimensions is most likely an AFM imaging artifact possibly due to the AFM tip radius of curvature (quoted to be about 10 nm) being roughly the same size as the nano-dots. In fact, other AFM scans show clear imaging artifacts and AFM tips were seen to clearly degrade through time while scanning these nano-dot arrays. However, the AFM scan does serve to indicate that all dimensions (height, diameter, and spacings) are extremely uniform with deviations of roughly 10% or less.

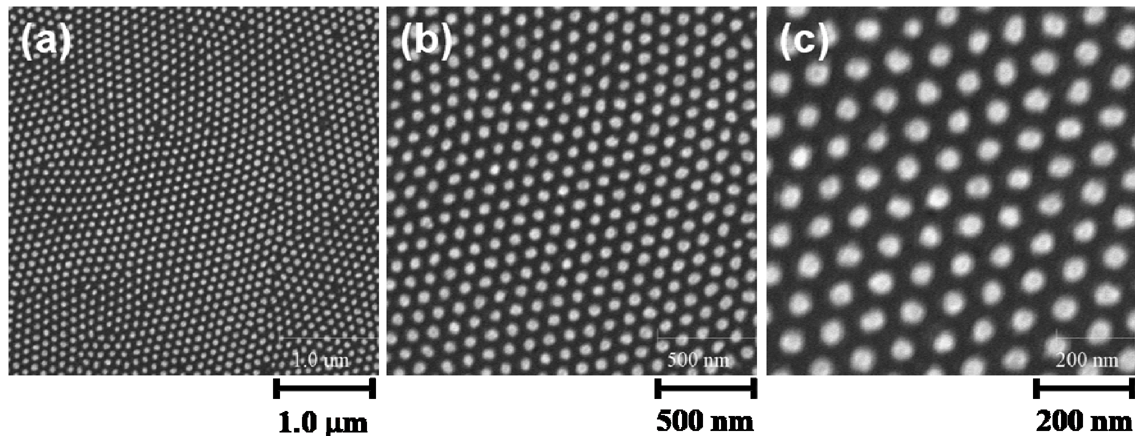

Figure 4.4. Top down SEM micrographs of array of Au nano-dots thermally evaporated through a porous AAO mask onto a Si substrate. (a) Low magnification SEM showing presence of grain boundaries and missing dots (b) Medium magnification SEM (c) High magnification showing a very well-ordered region.

4.3.2 Other Examples of Thermally Evaporated Nano-Dot Arrays using Oxalic Acid-Grown AAO Masks

As a general rule of thumb, utilizing this method essentially any material that can be thermally evaporated can be used to create a nano-dot array. Dot arrays of various materials including Au, Al, Cr, Fe, In, and Ni were fabricated during the course of this research. As an example, Figure 4.4 shows top down SEM micrographs of a Au array of nano-dots evaporated through an oxalic acid-grown AAO mask with 50 nm pore diameters spaced 100 nm apart. Once again, grain boundaries, point defects, and missing dots can be seen in Figures

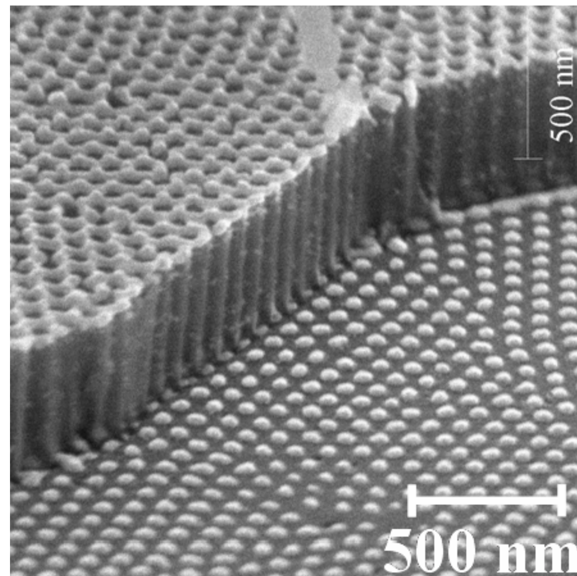

Figure 4.5. 60° oblique angle SEM micrograph of Au nano-dot array thermally evaporated through a porous AAO mask onto a Si substrate. Note the remaining porous AAO mask in the upper left part of the image.

4.4 (a) and (b) while Figure 4.4 (c) shows a region exhibiting a very well-ordered array of dots. In this case approximately 70 nm of Au was evaporated through a 500 nm thick mask yielding approximately 20 nm tall dots. Figure 4.5 shows a 60° oblique angle SEM micrograph of the Au nano-dot array where a piece of the AAO mask remains. Note the presence of a Au layer coating the top surface of the AAO and preferentially balling up or accumulating at higher positions around the pore walls. This effect along with decreasing pore diameters during evaporation as Au continues to coat the AAO pore walls can affect the dot transfer characteristics including the shape and height of the dots.

To illustrate this, Figure 4.6 shows 60° oblique angle SEM micrographs of Ni dot arrays for two different evaporation thicknesses demonstrating the dependence of dot height and shape on the amount of evaporation. Figures 4.6 (a) and (b) show low magnification and high magnification images, respectively, of 15 nm

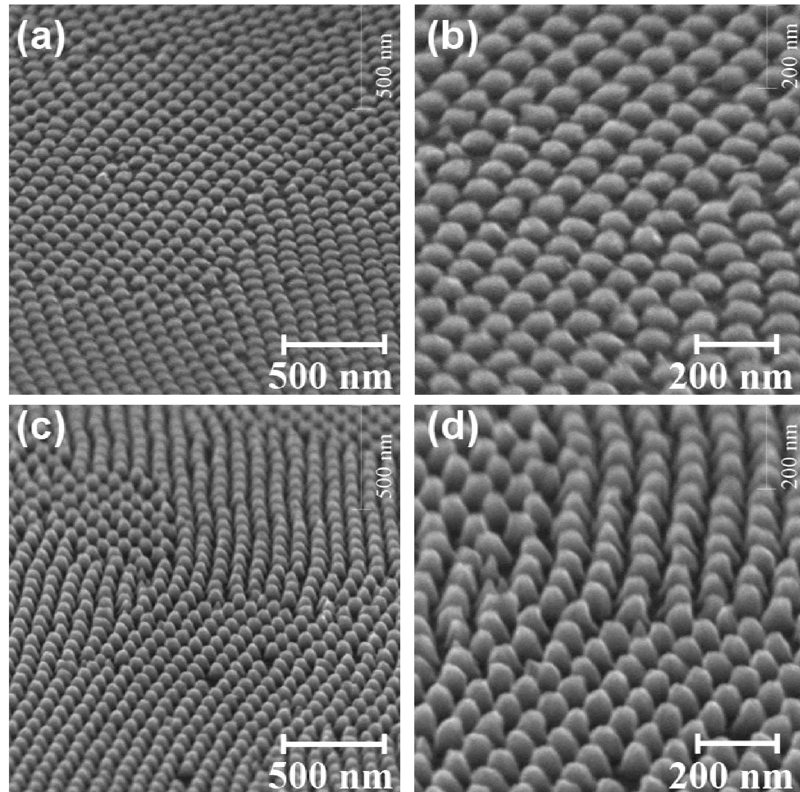

Figure 4.6. 60° oblique angle SEM micrographs of Ni dot arrays evaporated through an AAO mask illustrating dot height and shape differences controlled through the amount of evaporation. (a) and (b) show low magnification and high magnification SEM images, respectively of 15 nm tall spherical Ni dots. (c) and (d) show low mag. and high mag. SEM images, respectively of 45 nm tall conical Ni dots.

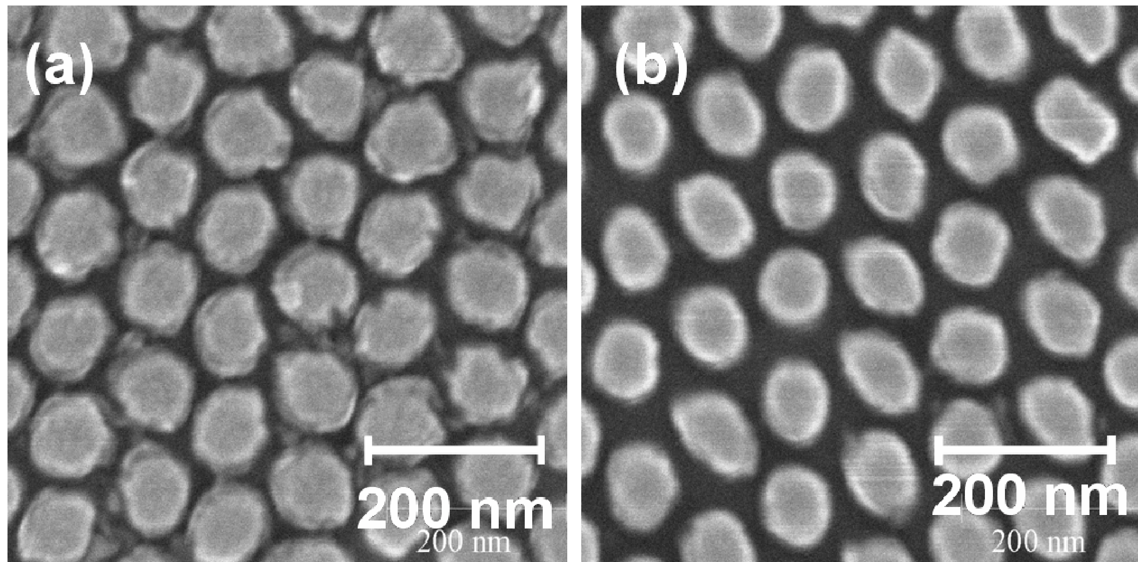

Figure 4.7. (a) SEM micrograph of Ni nano-dot array after removal of AAO mask. (b) SEM micrograph of same Ni nano-dot array after an O_2 plasma etching step to remove organic materials.

high dots (30 nm bulk Ni evaporated) while Figures 4.6 (c) and (d) shows low magnification and high magnification images, respectively, of 45 nm high dots (70 nm bulk Ni evaporated). In both cases, the dots have an average diameter of 75 nm (due to a pore widening step) and are spaced 100 nm apart. In both cases, a 350 nm thick, 75 nm pore diameter (aspect ratio ~ 4.6:1) AAO mask was used yielding material transmission factors of (15 nm/30 nm) ~ 50 % and (45 nm/70 nm) ~ 64 %, respectively. The transmission factors are in fairly good agreement with each other and as expected, are larger than those found using higher aspect ratio masks. Also, note that the taller dots appear more conical in shape than the smaller spheroid dots. This is thought to be due to the decreasing pore size during the evaporation as Ni started to close up the pores.

As a final concern in fabricating nano-dot arrays using this method, it should be noted that some nano-dot arrays showed the presence of remaining organic materials that could only be removed by plasma etching. The organic material was thought to be remnants of the collodion layer used during AAO mask processing. Figure 4.7 shows top

down SEM micrographs of a Ni nano-dot array before and after an oxygen plasma etching step to remove organic materials. Figure 4.7 (a) shows a Ni dot array directly after removal of the AAO mask while Figure 7 (b) shows the same Ni dot array after a 0.8 Torr, 70W O_2 plasma etching step for 30 minutes. Note the clear presence of debris around the dots shown in Figure 4.7 (a) which was successfully removed by plasma etching as shown in Figure 4.7 (b).

4.3.3 Thermally Evaporated Nano-Dot Arrays using Sulfuric Acid-Grown AAO Masks

The above examples of nano-dot arrays were all created using oxalic acid-grown porous AAO masks which yielded dots with diameters ranging anywhere from about 50-75 nm with dot-to-dot spacings of 100 nm. Some success in transferring dot array patterns was also obtained using sulfuric acid-grown AAO masks with smaller dimensions. In this case, the AAO film was anodized in 1.7 wt % sulfuric acid at 27 V and 2 ^{o}C for 15 hours, conditions appropriate to maximize the self-ordering. The AAO film was then stripped from the Al foil and a secondary anodization under identical conditions as the first was carried out for 3 minutes. This resulted in an AAO film approximately 200 nm thick with 20 nm pore diameters spaced 60 nm apart. The remaining processing steps were identical to that used above for oxalic acid-grown films except the barrier layer opening etch was done for 26 minutes instead of 34 minutes due to the thinner barrier layer resulting from the lower anodizing voltage. AAO masks were then lifted off onto Si and various materials were evaporated.

Figure 4.8 (a) shows a top down SEM image of a Ni nano-dot array thermally evaporated through a sulfuric acid-grown AAO mask. From this figure, it can be seen

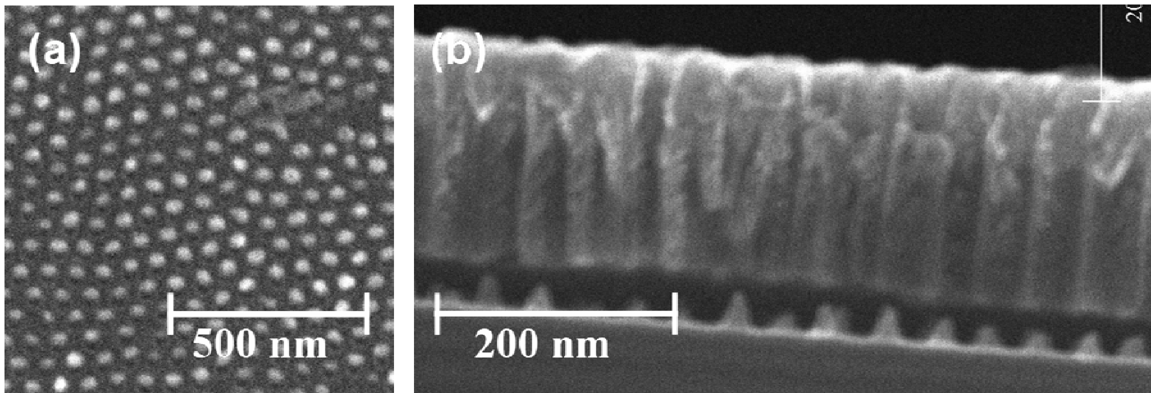

Figure 4.8. (a) Top down SEM micrograph of array of Ni nano-dots thermally evaporated onto a Si substrate through a sulfuric acid-grown porous AAO mask with 20 nm pore diameters spaced 60 nm apart. (b) Cross-sectional SEM image showing the sulfuric acid-grown porous AAO mask and Ni dot array.

that the transfer and the ordering of the dots are not as good as the ones fabricated using the oxalic acid-grown masks although the nano-dot dimensions are smaller. Figure 4.8 (b) shows a cross-sectional SEM image of the dots with the AAO still present although slightly off the surface of the silicon substrate, presumably due to cleaving the sample for SEM observation. Note the presence of Ni coating the top surface of the AAO film. From the two images in Figure 4.8, the diameter and spacing of the dots are around 25 nm and 60 nm, respectively showing good agreement with the AAO pore dimensions. In addition, the cross-sectional image shows the 30 nm tall dots to be extremely conical in shape due to Ni closing up the pore diameters during evaporation. 70 nm of Ni was evaporated in this case giving a material transmission factor through the 10:1 aspect ratio pores of 43 %.

Figure 4.9 (a) shows a 5 μm x 5 μm AFM image of MgF_2 dots evaporated through a sulfuric acid-grown AAO film onto a Si substrate while Figure 4.9 (b) shows a 2 μm x 2 μm AFM image of the same sample. (Note that an imaging artifact occurs about three quarters of the way down Figure 4.9 (b) which does not reflect the actual topography of the sample.) The color scale in these images is 40 nm and the average dot

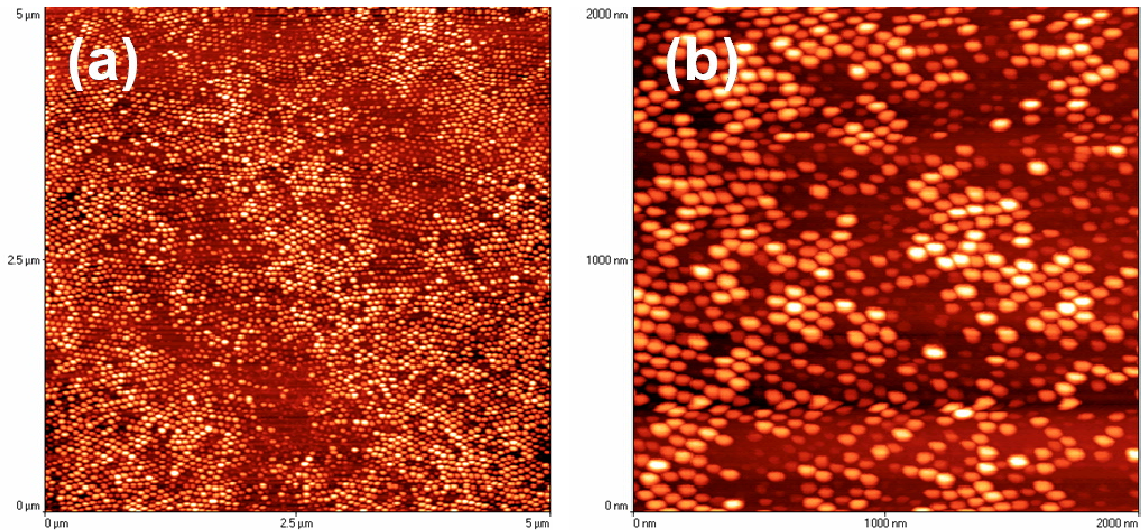

Figure 4.9. (a) 5 µm x 5 µm non-contact AFM image of MgF_2 nano-dot array thermally evaporated through a sulfuric acid-grown AAO mask. (b) 2 µm x 2 µm non-contact AFM image of the same array. The color scale is approximately 40 nm in both images.

height is roughly 30 nm. Once again, the transfer and ordering of the dots is not as good as the oxalic-acid grown films used to transfer dot arrays. Missing dots and greater variation in dot height, consistent with problems with material transmission through the mask, are presumably due to the smaller pore diameters (although the aspect ratio of the sulfuric acid and oxalic acid-grown AAO films are comparable) closing up more readily during the evaporation. Different evaporation parameters such as a longer source-to-sample distance, better vacuum, and slower evaporation rates would probably yield better results.

4.4. SPUTTER DEPOSITED NANO-DOT ARRAYS

In addition, to thermally evaporated nano-dot arrays, AAO films have also been used successfully to create sputtered nano-dot arrays. Carbon, cobalt, and molybdenum sputtered dot arrays on both silicon and gallium arsenide have been fabricated during the course of this research. As an example, Figure 4.10 (a) and (b) shows 5 µm x 5 µm and 1

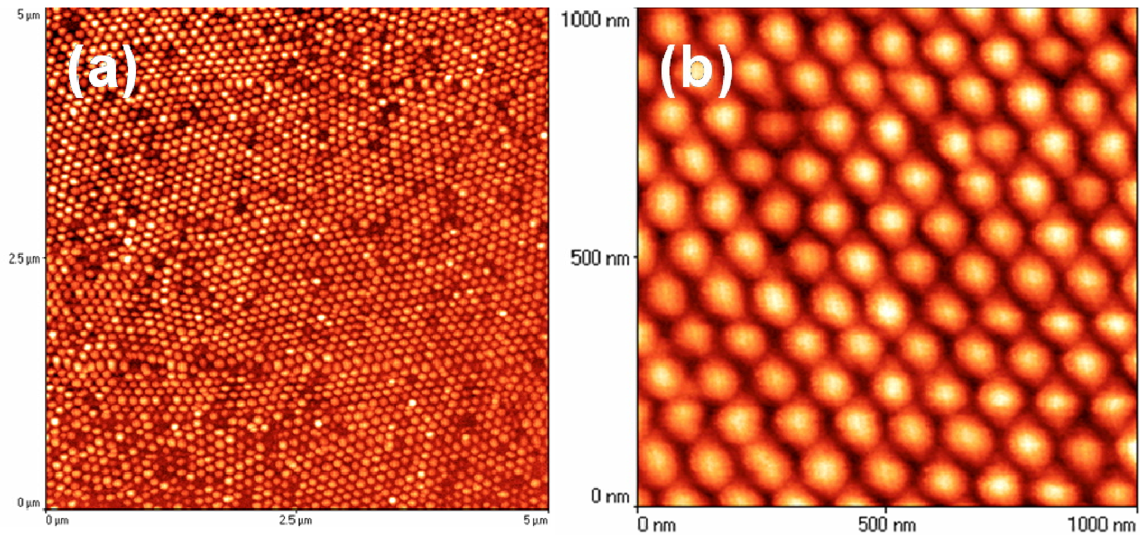

Figure 4.10. (a) 5 µm x 5 µm non-contact AFM image of Mo dots sputtered through an oxalic acid-grown AAO mask onto a Si substrate. (b) 2 µm x 2 µm non-contact AFM image of a well-ordered region. The color scale for both images is approximately 14 nm.

µm x 1 µm non-contact AFM images, respectively, of a Mo nano-dot array sputtered using a Torus 2C Sputter Deposition Source through a 500 nm thick oxalic acid-grown AAO mask. The color scale for both images is approximately 14 nm. The source material, consisting of a 2" diameter target of Mo, was positioned directly underneath the sample and the sample-to-source was approximately 12 cm. In addition, a 2 mm aperture was placed 2 cm away from the sample to limit the incoming divergence angle of the sputtered material and increase the chance of this material traveling down the pore channels to the substrate. This was done to counteract the broad flux distribution of the source (unlike thermal evaporation) and essentially created a point source with an angular dispersion of 20mm/2mm = 10:1 so as to be comparable to the 10:1 aspect ratio of the AAO mask. Mo was then RF-sputtered in an Ar plasma at a pressure of 10^{-3} Torr, and 100 W. 220 nm was evaporated onto a crystal monitor located closer (approximately 8mm) to the Mo source than the sample. Figure 4.10 (a) shows a typical region with grain boundaries and some missing dots while Figure 4.10 (b) shows a close-up of a well-

ordered region. The nano-dot array and nano-dot shape compares well with arrays created by thermal evaporation. From the AFM images in Figure 4.10, the average dot diameter is around 55 nm with a dot-to-dot spacing of 100 nm. The average dot height is 10 nm. The smaller height of the nano-dots reflects the fact that much of the sputtered material did not reach the sample due to the inclusion of the aperture that limited the high divergence angle particles.

4.5. UV-VIS SPECTROSCOPY OF AU NANO-DOT ARRAYS

4.5.1 Introduction

In an effort to further characterize these arrays of nano-dots, UV-Vis absorption spectroscopy was performed on ordered and unordered Au nano-dot arrays on fused silica substrates. These results were compared with results from a colloidal suspension of similarly sized monodisperse colloidal Au dots in an aqueous solution, as well as theoretical results using MiePlot v3.1.02, a computer program for the scattering of light from non-interacting, homogeneous spheres taking into account Mie scattering as well as absorption phenomena (e.g. plasmon resonances in metal nanoparticles).

4.5.2 Ordered and Unordered Au Nano-Dot Arrays

To start, an ordered Au nano-dot array on fused silica was prepared following the procedure discussed above using an oxalic acid-grown AAO mask. In addition, a disordered Au nano-dot array on fused silica was prepared by evaporating Au through an unordered oxalic acid-grown AAO mask. The unordered AAO mask was prepared by anodizing an Al foil once under identical conditions as the twice-anodized, ordered oxalic acid-grown AAO mask (i.e. the Al foil underwent a single 5 minute anodization in 0.3M

oxalic acid at 40 V and 2°C). Both the ordered and unordered AAO masks were lifted out onto both fused silica and Si witness samples that underwent Au thermal evaporations. The purpose of the witness samples was to allow convenient SEM observation to determine the dot dimensions. Figures 4.11 (a) and (b) show SEM images of the top surface of both the ordered and unordered AAO films after the gold evaporation, respectively. Figures 4.11 (c) and (d) show SEM images of the ordered Au nano-dot array and the and unordered Au nano-dot array on Si witness samples, respectively. Note that both AAO films clearly show Au closing up or blocking some of the pores which is most likely responsible for the missing dots that can be seen in both the ordered and unordered Au nano-dot arrays. Also note that the unordered array of dots is clearly smaller in diameter as compared to the ordered array of dots even though both were subjected to the same evaporation conditions. This is mostly likely a

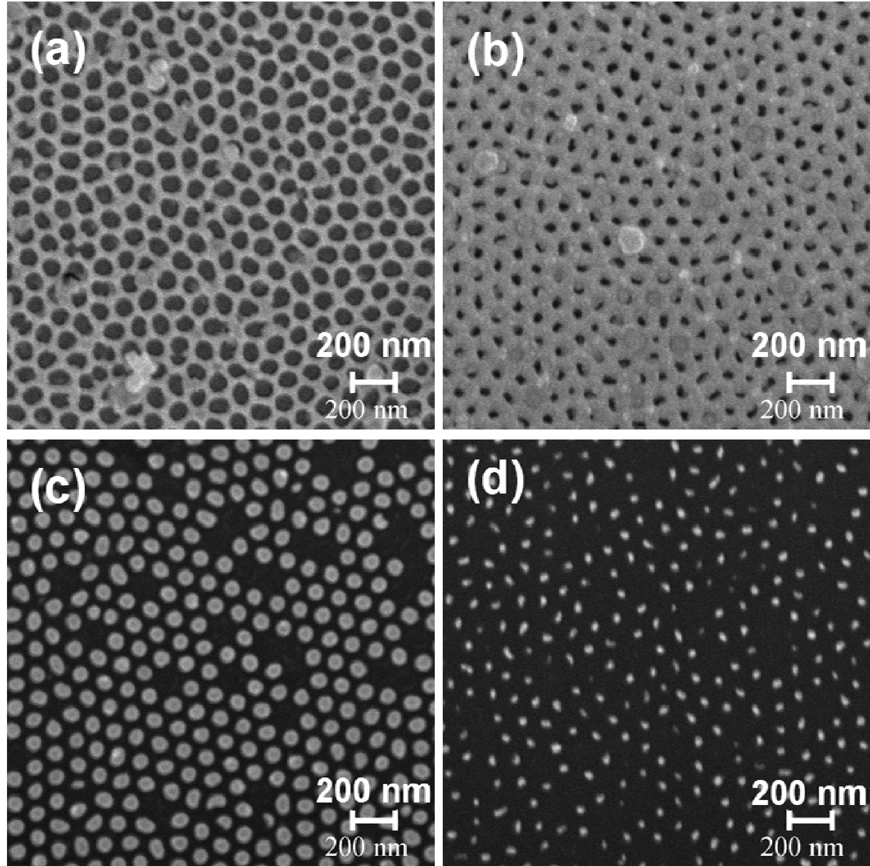

Figure 4.11. Top down SEM micrographs of: (a) Au covered, ordered AAO film. (b) Au covered, unordered AAO film. (c) Ordered Au nano-dot array. (d) Unordered Au nano-dot array.

consequence of the non-straight or kinked pore channels in the unordered AAO film limiting the amount of Au getting down the pores. From the SEM images, the average diameters and spacing of the ordered (unordered) nano-dots are 75 nm (37 nm) and 100 nm (100 nm). From AFM measurements on the nano-dot arrays on the quartz substrates, the average height of the ordered (unordered) dots are approximately 60 nm (50 nm).

4.5.3 Monodisperse Au Dots in Aqueous Solution

In addition to the Au nano-dot arrays prepared using AAO films, monodisperse Au dots in aqueous solutions were prepared by collaborators in Dr. Lloyd Bumm's group in the Physics Department at the University of Oklahoma following the standard procedure set out by Frens [64] involving the reduction of gold chloride with sodium citrate. The Au sphere diameters are controlled by the concentration of sodium citrate. In brief, a higher concentration of sodium citrate leads to more nucleation sites (i.e. more nano-particles) which leads to smaller diameter nano-particles. For this study, monodisperse Au spheres with diameters of 14 nm and 76 nm were prepared for UV-Vis absorption spectroscopy. Details of the growth procedure can be found in ref [64].

4.5.4 MiePlot

Both the 2D Au nano-dot arrays (ordered and unordered) and the Au spheres in aqueous solutions were compared with theoretical results using MiePlot v3.1.02. This computer program takes into account Mie scattering theory and absorption phenomena. Mie scattering theory uses classical electromagnetic theory to calculate the scattering cross-section for a plane wave light incident on a uniform dielectric sphere of arbitrary radius, r. Unlike the well known Rayleigh scattering result for atoms and molecules (i.e. particles with $r \leq$ *to* $1/10\lambda$) which only takes into account dipole scattering, Mie theory

looks at higher order excitations as well (i.e. quadrapoles, octopoles, etc.). As such, Mie scattering is a good model for particles $r \geq to\ 1/10\lambda$ where the scattering intensity is largely forward. This is in contrast to the Rayleigh result with dipole scatterers which scatter uniformly in all directions. As expected, Mie scattering reduces to the Rayleigh formula at small radii. For a concentration of uniformly-sized spheres such as found in a solution or an array, if the density is not too large, then the spheres can be treated as independent scatterers (i.e. no cross-talk, multiple scattering events, or collective phenomena). Within this single scattering regime assumption, the scattering curve is additive and the intensity is simply proportional to the scattering curve for a single sphere.

MiePlot was used to calculate the extinction spectrum intensity, Q_{ext}, in the forward direction due to both scattering and absorption effects to account for all loss of light. Thus,

$$Q_{ext} = Scattering\ Cross - Section\ /\ Geometric\ Cross - Section = Q_{scat} + Q_{abs} \qquad (4.1)$$

where Q_{scat} is the extinction spectrum intensity due to scattering and Q_{abs} is the extinction spectrum due to absorption. This allows a direct comparison with UV-Vis absorption spectroscopy since Q_{ext} is what is directly measured. For this particular case, MiePlot was used to calculate Q_{ext} versus λ for unpolarized light scattering off of monodisperse Au nano-spheres in a fused silica medium with diameters in the range of the Au nano-dot array.

4.5.5 UV-Vis Spectroscopy

The UV-Vis spectroscopy was carried out with a Varian Cary 50 consisting of a full spectrum Xe pulse lamp source and Si diode detectors. Scans were taken of the

ordered and unordered Au nano-dot arrays on fused silica substrates as well as the monodisperse Au dots in aqueous solution. All scans were taken at identical conditions consisting of a wavelength range of 350 nm-800 nm taken at a scan rate of 600 nm/min. The wavelength interval was 1 nm and the average collection time was 100 msec. In addition, a baseline correction for background subtraction was taken on a fused silica substrate.

4.5.6 Results and Discussion

Figure 4.12 (a) shows a UV-Vis spectrum in the 350-800 nm range for the ordered and unordered Au nano-dot array, while Figure 4.12 (b) shows the calculated MiePlot results in the same range for monodisperse Au spheres with diameters ranging from 40-80 nm in a fused silica medium. Finally, Figure 4.12 (c) shows a UV-Vis spectrum in the 350-800 nm range for the Au dots in an aqueous solution prepared by the reduction of gold chloride with sodium citrate. A MiePlot comparison (not shown) of the Au dots in an aqueous solution showed excellent agreement both qualitatively and quantitatively with the UV-Vis spectrum of Figure 4.12 (c). Comparing the UV-Vis spectrum of the 2D Au nano-dot arrays (Figure 4.12 (a)) with the UV-Vis spectrum of the Au dots in solution (Figure 4.12 (c)), it can be seen that the general shape of the curves agree well with each other. In this case, no quantitative agreement is necessarily expected since the nano-dots are in two different mediums (fused silica for the 2D nano-dot array and an aqueous environment for the Au dots in solution).

Comparing the UV-Vis spectrum of the 2D Au nano-dot arrays (Figure 4.12 (a)) with the MiePlot results (Figure 4.12 (b)), it can be seen that the spectrums show good qualitative agreement with each other. Specifically, all the curves show the same general

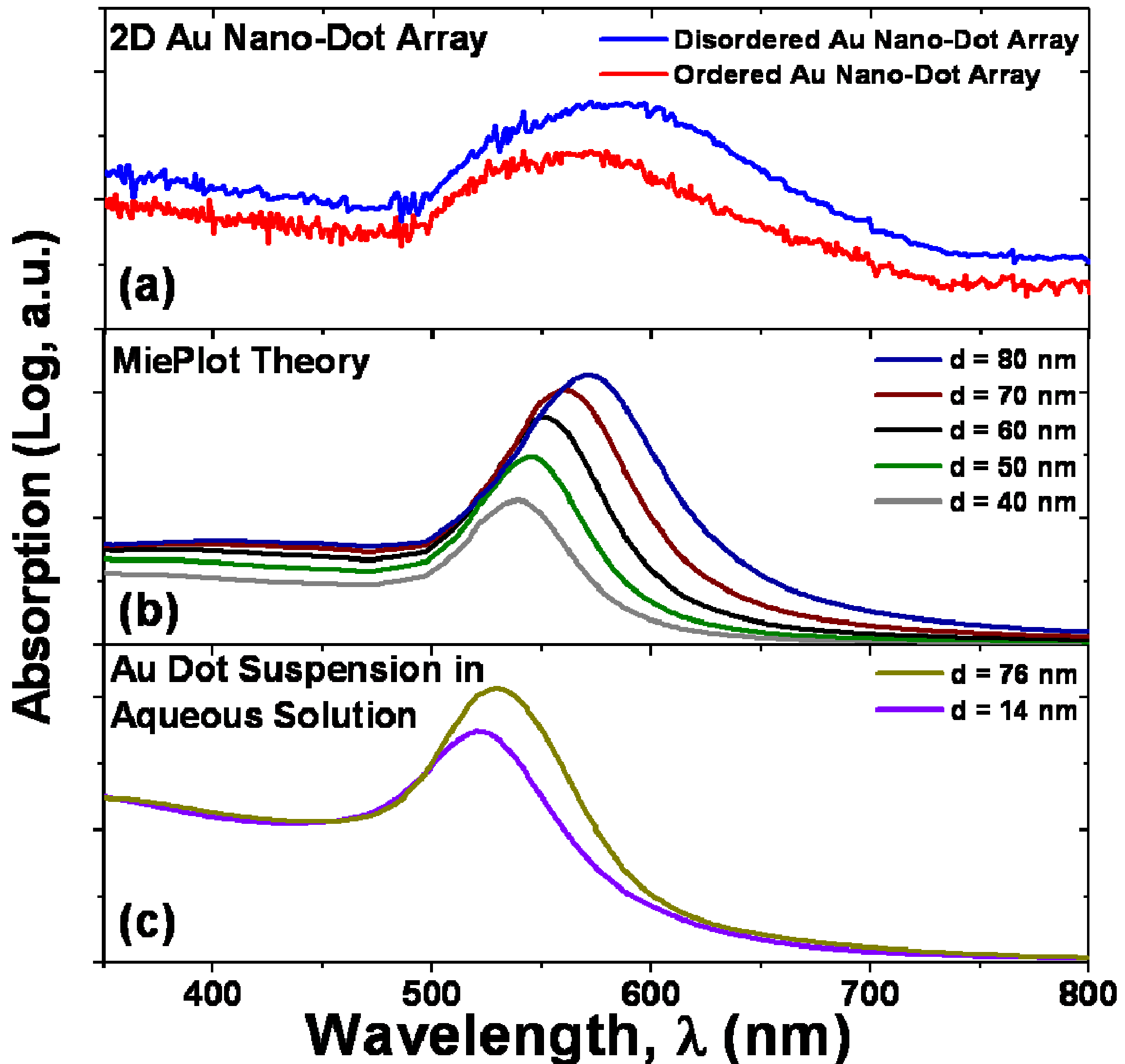

Figure 4.12. (a) UV-Vis spectrum of ordered and unordered Au nano-dot array. (b) MiePlot theoretical results of Au dots of varying diameters in a fused silica environment. (c) UV-Vis spectrum of 14 and 76 nm diameter Au dots in an aqueous solution.

trend exhibiting a peak in absorption (or Q_{ext}) in the 500-600 nm regime before dying out at higher wavelengths. However, the Au nano-dot array spectrums differ quantitatively from the MiePlot results. In particular, the UV-Vis spectrums are considerably broader than the MiePlot curves and the position of the absorption peaks suggests a dot diameter slightly larger than those measured directly via the SEM and AFM. In addition, the UV-Vis spectrum suggests that the diameter of the unordered nano-dots is larger than the

diameter of the ordered nano-dots. The cause for this disagreement in the Q_{ext} of the UV-Vis spectrum of the nano-dot arrays compared to the Q_{ext} calculated by MiePlot must result from a disagreement in either Q_{scat}, Q_{abs} or both.

The most likely cause for a discrepancy in Q_{scat} is due to the MiePlot assumption that the dots are spherical and monodisperse. In fact, both SEM and AFM observations show the Au nano-dot arrays have both a non-uniform size distribution and a non-spherical shape. The size distribution is fairly small (around 10 %) for the ordered array but becomes more of a factor (around 20 %) for the unordered array. In addition, the shape of the nano-dots in both the ordered and unordered arrays is basically conical in structure. Again, a larger variety of dot shapes can be observed for the unordered array most likely due to the non-circular pores from the unordered AAO mask as shown in Figures 4.11 (b). Another assumption made in MiePlot's calculation of the Q_{scat} term is that the concentration of dots is low enough so as to be in the single scattering regime. In this case, this is probably a good assumption given that the Au nano-dot array lies in a plane with a density of roughly 10^{10} dots/cm^2. For multiple scattering events to occur, the incident light would have to scatter parallel (90°) to the nano-dot array and subsequently re-scatter in the forward direction. These scattering events are expected to be minimal since light scattering from particles in this size regime is largely forward and thus the parallel scattering cross-section is small.

In addition, a discrepancy in the Q_{abs} term could come about in the MiePlot calculation since it does not take into account any collective phenomena involving the closely-spaced (~100 nm) dots. The wavelength dependence of both surface or bulk plasmon resonances could be altered by the high area density of possibly non-

independent dots. To resolve these discrepancies, a more involved theoretical model would need to be implemented taking into account both the non-uniform shape and sizes of these dots as well as their possible interactions via collective plasmon resonances.

4.6. CONCLUSION

Ordered nano-dot arrays of a wide range of materials (MgF_2, Au, Ni, etc.) were fabricated by evaporating or sputtering material through AAO shadow masks lifted off onto various substrates. Using this technique, nano-dot arrays with diameters ranging from 20 nm to 75 nm and dot spacings ranging from 60 nm to 100 nm were fabricated onto various substrates. UV-Vis absorption spectroscopy of Au nano-dot arrays fabricated using these methods onto fused silica substrates showed good qualitative agreement with expected Mie scattering and absorption results. Quantitative disagreement is likely due to a failure in the Mie scattering and absorption model to take into account the non-spherical, closely-spaced, and possibly collective or interacting behavior of these dots.

Chapter 5

Pattern Transfer with AAO: Nano-Hole Arrays

5.1. ABSTRACT

Nano-hole arrays have been fabricated onto various substrates by atomic or ion beam etching through AAO films. Such structures have a variety of applications in various fields such as waveguiding structures in photonic devices, building blocks in IC fabrication (*e.g.* nano-capacitors in Chapter 7), *etc.* As with the nano-dot arrays, large areas can be patterned with this technique which allows various characterization techniques to be used (*e.g.* Photoluminesence of Si in Chapter 6). The procedure involved in the growth and use of the AAO films as shadow masks is identical to that used to create nano-dot arrays as described in Chapter 4. As in the previous case, the Al foil and barrier layer are removed from AAO films and the films are placed directly onto various substrates. These films are then used as shadow masks or templates to directly transfer the AAO nano-hole array pattern into underlying substrates through the use of dry etching techniques. This chapter will present work on nano-hole arrays fabricated by

using three different dry etching techniques to transfer the AAO nano-pore pattern into underlying substrates. In particular, Ar^+ ion etching, Cl_2 reactive ion beam etching (RIBE), and neutral atomic fluorine beam etching were investigated for fabricating nano-hole arrays into Si, GaAs, and InSb substrates. After etching and upon removal of the AAO films, a well-ordered hexagonal array of nano-holes with lateral dimensions comparable to the pore dimensions of the AAO was obtained.

5.2. ION ETCHED NANO-HOLE ARRAYS

An AAO film was fabricated by a two step anodization process first laid out by Masuda *et al.* [59], described in detail in Chapters 3 and 4, and shown schematically in Chapter 4, Figure 1 (a)-(c). First, a high purity Al foil was anodized in 0.3 M oxalic acid at 40 V and 10 ^{o}C for 15 hours. The resulting AAO film was stripped from the Al foil and a secondary anodization in 0.3 M oxalic acid at 40 V and 10 ^{o}C for 5 minutes was carried out. This resulted in an approximately 500 nm thick AAO film on an Al foil with well-ordered, hexagonally close-packed pores with 50 nm diameters spaced 100 nm apart.. Next, the processing steps described in Chapter 4 and shown in detail in Chapter 4, Figure 1 (d)-(g) were carried out to make a through-hole AAO mask. As before, a thin layer of collodion was spun onto the AAO film and the film was separated from the Al foil in a saturated $HgCl_2$ solution. Next, the barrier layer was removed in a 5 wt % solution of H_3PO_4 at 30 ^{o}C for about 35 minutes. This was followed by lifting off the AAO film onto a GaAs substrate and allowing the film to dry before immersing the sample in acetone to remove the collodion layer. This resulted in a through-hole AAO mask approximately 3 mm x 3 mm in size weakly bonded by van der Waal forces to a

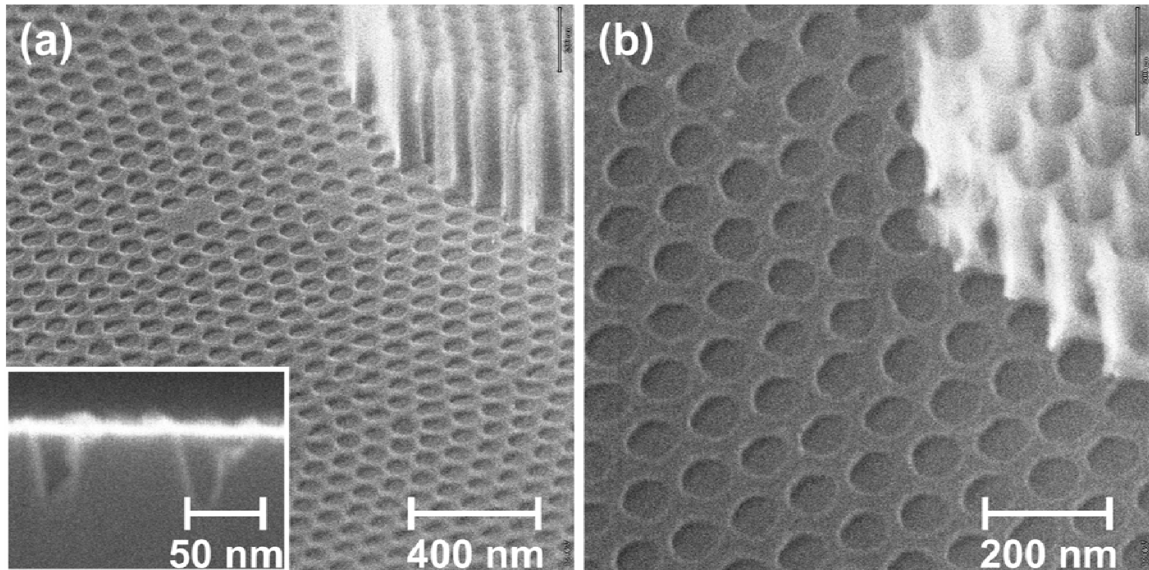

Figure 5.1. (a) 60° oblique angle SEM micrograph of nano-hole array in GaAs fabricated by Ar^+ ion etching through a porous AAO mask. Note piece of AAO mask remaining in upper right corner. Inset shows a cross-sectional SEM image of the nano-hole profile. (b) 20° oblique angle SEM micrograph showing a close-up view of the nano-hole array in GaAs. Again, note the piece of AAO remaining in the upper right corner.

GaAs substrate. The AAO on GaAs sample was then exposed to an Ar^+ ion beam (VG Microtech EX05) for 2 hours and 12 minutes in a vacuum environment (10^{-10} Torr with the beam off, 10^{-6} Torr with the beam on) with a source to sample distance of 50 mm and an angular divergence of about 0.1°. The beam had an energy of 500 eV and a current density of 0.02 ma/cm^2. After etching, the AAO film was removed from the GaAs substrate in select areas by mechanical means (i.e. double-sided carbon tape was used to peel off the AAO film).

Figure 5.1 (a) shows a 60° oblique angle SEM micrograph of the resulting well-ordered nano-hole array transferred into the GaAs substrate. A remaining piece of the AAO film used as the etching mask is still present in the upper right corner of the micrograph and shows good registry with the underlying nano-hole pattern in the GaAs. From the micrograph it can be seen that most of the hexagonal AAO pore pattern has been transferred into the GaAs substrate with the exception of a few missing holes or

defects possibly due to an obstruction blocking the AAO pores during etching. Figure 5.1 (b) shows a close up, 20° oblique angle SEM micrograph of the same region with the remaining AAO film in the upper right corner. From top down SEM micrographs (not shown), the resulting nano-hole array has similar dimensions to the AAO film with nano-hole diameters of approximately 50 nm spaced 100 nm apart. The depth of the nano-holes was determined by cross-sectional SEM (inset of Figure 5.1 (a)) to be about 50 nm. Referring to a standardized table of Ar^+ ion etch rates for various materials at 500 eV and 1 ma/cm^2 [65] and normalizing the results to our current density, the bulk etch rate was determined to be 1.3 nm/min which would give a bulk etch depth of about 170 nm for the 2 hours and 12 minute etching time. The 50 nm depth of the nano-holes indicates an etch rate through the AAO nano-pore mask of 0.4 nm/min, a factor of roughly 3 lower than the expected bulk etch rate. This retarded etch rate through the AAO nano-pores as compared to the bulk etch rate has been observed by other researchers as patterned feature sizes diminish [9]. In this case, it is most likely due to scattering events (both molecule/sidewall and molecule/molecule) which limit the ability to efficiently transport Ar^+ ions and etching products (sputtered GaAs) into and out of both the relatively high aspect ratio AAO nano-pores (~ 10:1) and the etched nano-holes themselves.

Using this technique, nano-hole arrays have been fabricated in various materials other than the GaAs sample shown above. As an example, Figures 5.2 (a) and (b) show SEM micrographs of nano-hole arrays in both Si and InSb, respectively, fabricated by Ar^+ ion etching through AAO masks similar to the conditions shown in Figure 1. Note that both Figures 5.2 (a) (a 20° oblique angle SEM micrograph) and (b) (an 11° oblique angle SEM micrograph) show remaining pieces of the AAO etching mask at the top of

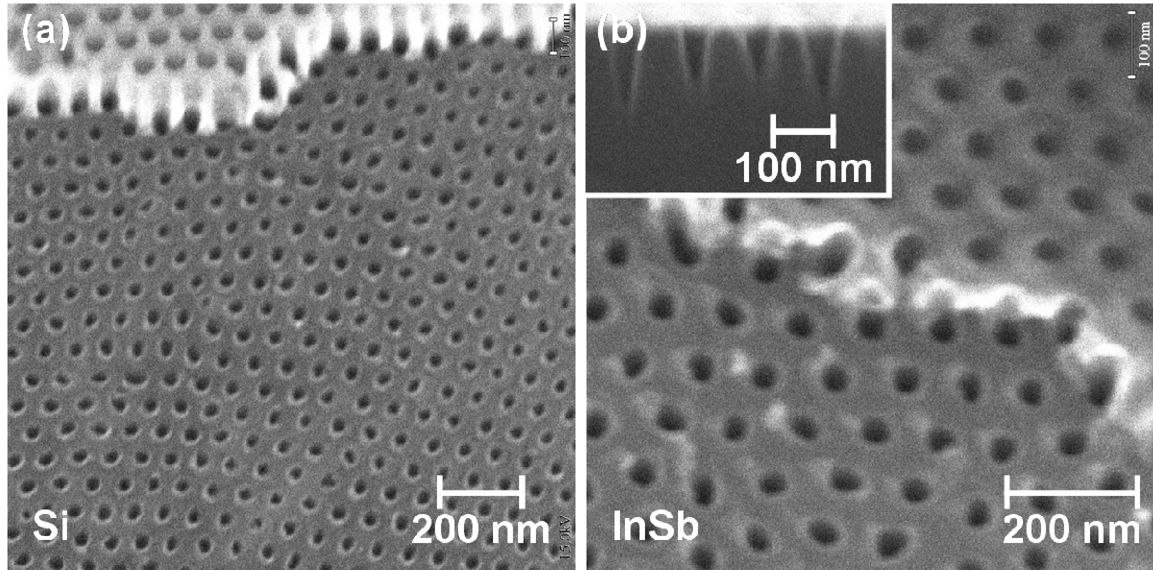

Figure 5.2. (a) 20° oblique angle SEM micrograph of nano-hole array in Si fabricated by Ar^+ ion etching through an oxalic acid-grown AAO mask. Note piece of AAO mask remains at the top of the image. (b) 11° oblique angle SEM micrograph of nano-hole array in InSb fabricated by Ar^+ ion etching through an oxalic acid-grown AAO mask. Again, a piece of the AAO mask remains at the top of the image. Inset shows a cross-sectional image of the InSb nano-hole profile.

the images. These nano-hole arrays have similar lateral dimensions as the GaAs nano-hole arrays (50 nm hole diameters spaced 100 nm apart) due to the nano-pore dimensions of the oxalic acid-grown AAO films.

The inset of Figure 5.2 (b) shows a cross-sectional SEM view of the hole profiles in the InSb substrate. In this case, the holes are roughly 100 nm deep and illustrate a conical or triangular cross-section typical of ion or sputter-etched holes. Physical sputtering effects such as the re-deposition of etched materials on the sidewalls limited the ultimate depth of the holes attainable in this setup to around 120 nm and also resulted in a significant tapering of the nano-hole sidewalls. As expected and shown later in this chapter and in Chapter 7, deeper holes with steeper sidewalls and flatter hole bottoms can be obtained by using other dry etching techniques (RIBE or atomic beam etching) rather than Ar^+ ion etching which relies on a purely physical bombardment of the Ar^+ ions with

the substrate to remove material by momentum transfer. It is also expected that damage due to charging and energetic ion bombardment will also be smaller using these other techniques.

5.3. REACTIVE ION BEAM ETCHED NANO-HOLE ARRAYS

Nano-hole arrays have also been fabricated using reactive ion beam etching (RIBE) instead of physical sputtering. Similar to the above, 500 nm thick, oxalic acid-grown AAO masks with 50 nm pores spaced 100 nm apart were lifted off onto GaAs substrates. These samples were then sent to researchers and collaboraters at Sandia National Labs who had convenient access to an RIBE chamber [66]. The samples were etched with an RIBE setup with a base pressure of $2x10^{-7}$ Torr using Cl_2 at a flow rate of 4 sccm, a forward power of 98 W, and a 40 mA beam current for 12 minutes. After etching, the samples were sent back to the University of Oklahoma and the AAO films were etched away in a dilute 10 wt% solution of HF, leaving behind the transferred nano-hole array in GaAs.

Figures 5.3 (a) and (b) shows top down SEM micrographs of the resulting nano-hole array in GaAs. The spacing of the nano-holes is approximately 100 nm, in good agreement with the nano-pore spacing in the AAO mask. The hole diameters, however, range from about 60-75 nm and are slightly larger and less uniform than the 50 nm AAO pore diameters. In addition, the nano-holes are not as circular as the pores in the AAO mask or the nano-holes fabricated by Ar^+ ion etching. These discrepancies are most likely due to a less collimated beam than the Ar^+ ion beam setup and to undercutting inherent in chemical etching techniques such as RIBE. In this case, etching takes place

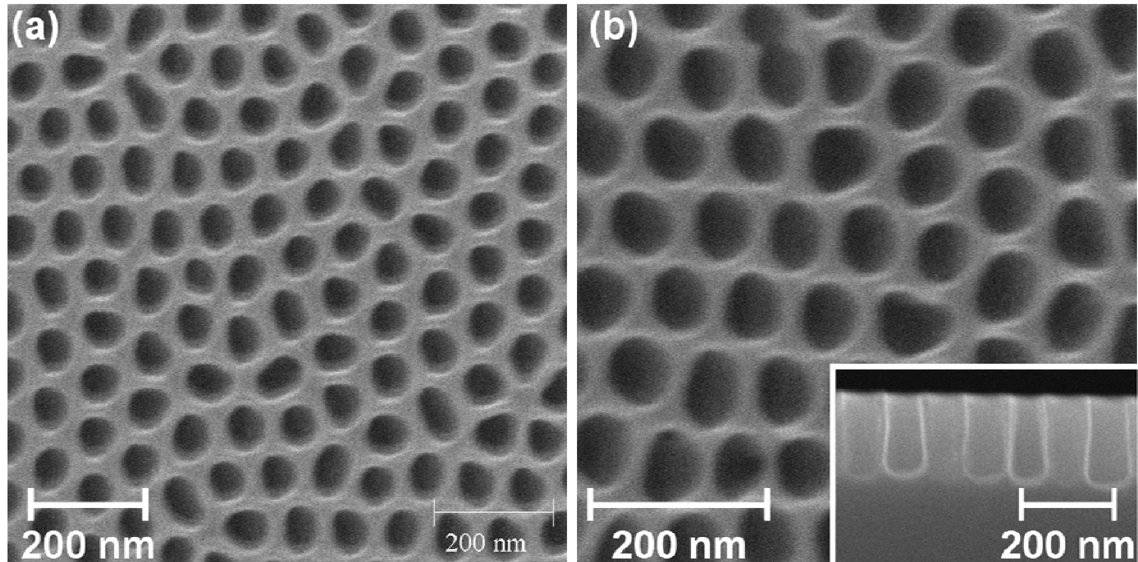

Figure 5.3. (a) Top down SEM micrograph of GaAs nano-hole array fabricated by RIBE through an oxalic acid-grown AAO mask. (b) Close up SEM micrograph of GaAs nano-hole array. Inset shows cross-sectional view of nano-hole profiles.

due to ion bombardment as well as chemical reactions between the incoming reactive ions and the GaAs substrate. While this results in steeper, smoother sidewalls and flatter hole bottoms as shown in the cross-sectional SEM micrograph (inset of Figure 5.3 (b)), it can also lead to undercutting due to reactive species scattering off the hole bottoms and subsequently striking and etching the hole sidewalls.

As mentioned above, the cross-sectional SEM view (inset of Figure 5.3 (b)) shows the nano-hole profiles to have much steeper sidewalls and flatter hole bottoms as compared to the Ar^+ ion etching case. However, the holes appear to be slightly bowed or widened towards the bottom of the hole. Again, this is mostly likely an effect due to beam collimation and the chemical nature of etching and has been seen by other researchers [9]. The depth of the holes in this case is about 180 nm, deeper than the holes that could be etched by Ar^+ ion etching which suffered from re-deposition of etched materials on the sidewalls affecting both the ultimate depth attainable and the nano-hole profile. In this case, the etch products are volatile and do not re-deposit onto the

sidewalls of the holes. From the etching conditions, the bulk etch rate was expected to be 35 nm/min leading to a bulk etch depth of 420 nm. The observed 180 nm hole depth gives an etch rate of 15 nm/min through the AAO nano-pores, approximately 2.3 times slower than the bulk etch rate and comparable to the retardation factor seen in the Ar^+ ion etched nano-holes. Although not verified, the damage to the GaAs material surrounding the RIBE nano-holes is expected to be less than the Ar^+ ion etched nano-holes since the charging and energetic ion bombardment is less severe.

5.4. ATOMIC FLUORINE BEAM ETCHED NANO-HOLE ARRAYS

5.4.1 Oxalic Acid-Grown AAO Masks

Nano-hole arrays have also been fabricated using the atomic fluorine beam etching apparatus discussed in Chapter 2. In this case, 500 nm thick, oxalic acid-grown AAO masks with 50 nm pores spaced 100 nm apart were lifted off onto both Si(100) and Si(111) substrates. The AAO/Si(100) sample was heated to 250 ^{o}C and exposed to the fluorine beam for 1 min. and 20 s. The AAO/Si(111) sample was heated to 350 ^{o}C and exposed to the 1 eV fluorine beam for 1 min. 15s. After exposure to the beam, the AAO masks were removed by mechanical means (i.e. carbon tape was used to peel the AAO masks off the Si substrates).

Figures 5.4 (a) and (b) shows top down SEM micrographs of the resulting Si(100) and Si(111) surfaces, respectively. In both (a) and (b), the insets show cross-sectional views of the nano-textured surfaces. In the case of the Si(100) surface, a hexagonally close-packed, square-shaped nano-hole array was created while in the case of the Si(111) surface, a hexagonally close-packed, triangular-shaped nano-hole array was created.

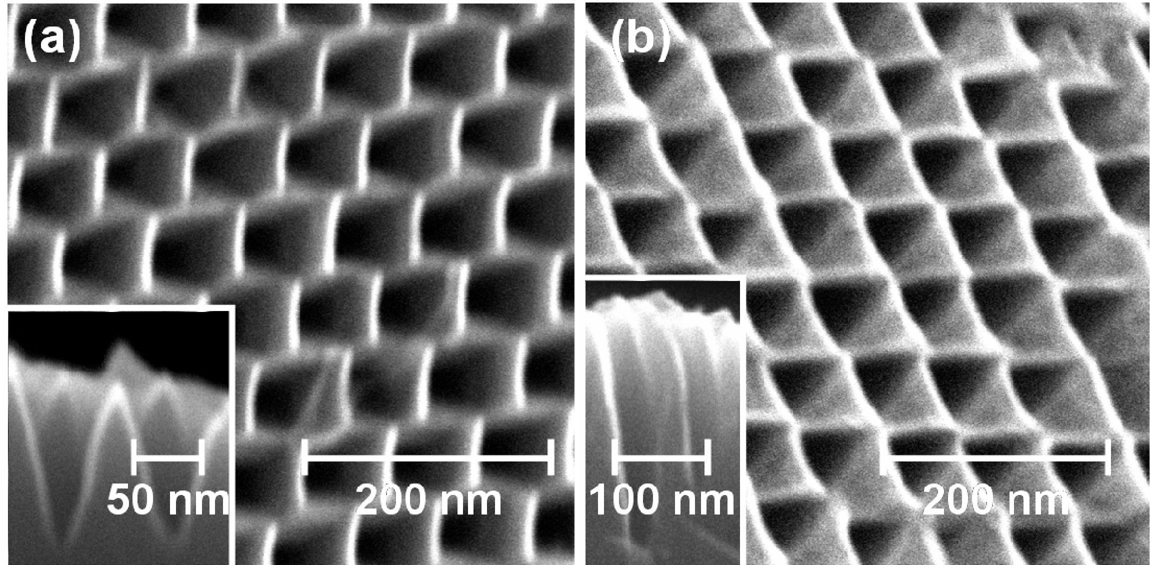

Figure 5.4. (a) Top down SEM micrograph of fluorine etched square-shaped nano-hole array in Si(100) fabricated using an oxalic acid-grown AAO mask. Inset shows cross-sectional view of the nano-holes. (b) Top down SEM micrograph of fluorine etched triangular-shaped nano-hole array in Si(111) fabricated using an oxalic acid-grown AAO mask. Inset shows cross-sectional view of the nano-holes.

These unique geometries are a consequence of the hexagonally close-packed nature of the AAO nano-pores combined with the purely chemical nature (rather than physical sputtering) of the F-Si etching mechanism which results in anisotropic etching that preferentially etches certain planes of Si faster than other planes. Figure 5.4 (a) should be compared directly to Chapter 2, Figure 3 which shows the square-shaped holes that naturally occur in bulk Si when etched by this atomic fluorine beam. The difference in this case is the square-shaped nano-holes were seeded into an ordered patterned by the AAO etching mask. A similar situation exists in the Si(111) sample but the Si(111) surface exposes a different orientation of the Si planes resulting in a triangular-shaped nano-hole array.

The spacing of both the square-shaped nano-holes and the triangular-shaped nano-holes is around 100 nm, consistent with the AAO nano-pore spacings. As discussed above, the anisotropic etching and undercutting lead to non-circular holes in the Si

substrates with dimensions comparable or slightly larger (~ 50 nm square sides, ~ 60 nm triangle sides) than the 50 nm pore diameters of the AAO mask. As determined by the cross-sectional SEM images (insets of Figure 5.4), the depth of the nano-holes for the square-shaped nano-hole array is about 120 nm while the depth of the nano-holes for the triangular-shaped nano-hole array is about 240 nm. From the etching conditions, the bulk etch rate was 350 nm/min (substrate temperature of 250 ^{o}C) for the square-shaped nano-hole array and 650 nm/min (substrate temperature of 350 ^{o}C) for the triangular-shaped nano-hole array. The observed etch depths give etch rates through the AAO nano-pore masks of 90 nm/min for the square-shaped nano-hole array (3.9 times slower than the bulk etch rate) and 192 nm/min (3.4 times slower than the bulk etch rate) for the triangular-shaped nano-hole array. The triangular-shaped nano-hole array has deeper nano-holes and steeper sidewall profiles, both consistent with the higher substrate temperature used to etch this sample as compared to the square-shaped nano-hole array. Similar Si nano-hole arrays are further investigated by photoluminescence in the Chapter 6.

5.4.2 Sulfuric Acid-Grown AAO Masks

In addition, some success in transferring nano-hole array patterns with the atomic fluorine beam was also obtained using sulfuric acid-grown AAO masks with smaller dimensions. In this case, the AAO film was anodized in 1.7 wt % sulfuric acid at 27 V and 2 ^{o}C for 15 hours, conditions appropriate to maximize the self-ordering. The AAO film was then stripped from the Al foil and a secondary anodization under identical conditions as the first was carried out for 3 minutes. This resulted in an AAO film approximately 200 nm thick with 20 nm pore diameters spaced 60 nm apart. The

remaining processing steps were identical to that used for oxalic acid-grown films except the barrier layer opening etch was done for 26 minutes instead of 34 minutes due to the thinner barrier layer resulting from the lower anodizing voltage. AAO masks were then lifted off onto Si(100) and Si(111) substrates. The AAO/Si(100) and AAO/Si(111) samples were heated to 300 ^{o}C and exposed to the fluorine beam for 30s and 1 min., respectively. After exposure to the beam, the AAO masks were removed by mechanical means (i.e. carbon tape was used to peel the AAO masks off the Si substrates).

Figures 5.5 (a) and (b) shows top down SEM micrographs of the resulting Si(100) and Si(111) surfaces, respectively. In both (a) and (b), the insets show cross-sectional views of the nano-textured surfaces. The geometries are similar to the previous examples using oxalic acid-grown AAO masks (i.e. a hexagonally close-packed, square-shaped nano-hole array for the Si(100) substrate and a hexagonally close-packed, triangular-shaped nano-hole array for the Si(111) substrate) but with smaller dimensions. In this

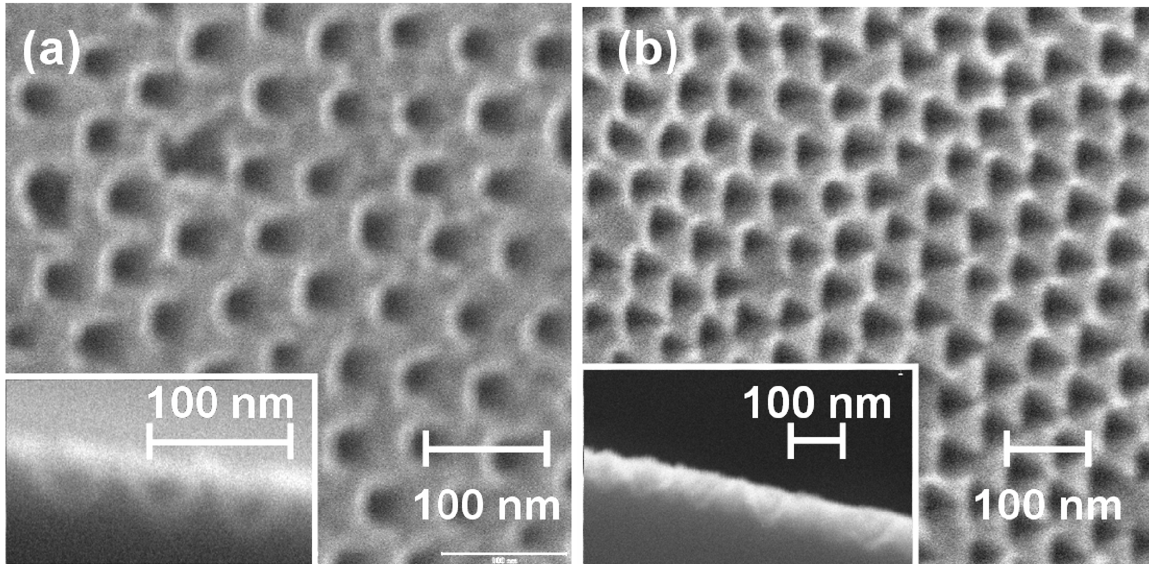

Figure 5.5. (a) Top down SEM micrograph of fluorine etched square-shaped nano-hole array in Si(100) fabricated using a sulfuric acid-grown AAO mask. Inset shows cross-sectional view of the nano-holes. (b) Top down SEM micrograph of fluorine etched triangular-shaped nano-hole array in Si(111) fabricated using a sulfuric acid-grown AAO mask. Inset shows cross-sectional view of the nano-holes.

case, the nano-hole array spacings are around 60 nm, in close agreement with the sulfuric acid-grown AAO nano-pore spacing while the other dimensions (~ 20 nm square sides, ~ 30 nm triangle sides) are again roughly the same or slightly larger than the nano-pore diameters of 20 nm. From the cross-sectional SEM views, the depth of the square-shaped nano-holes is 35 nm while the depth of the triangular-shaped nano-holes is 70 nm. The bulk etch rate of Si at a substrate temperature of 300 ^{o}C is about 550 nm/min. The etch rate through the sulfuric-acid grown AAO nano-pores was 70 nm/min. for both the square-shaped and triangular-shaped nano-holes, nearly 8 times slower than the bulk etch rate and over 2 times slower than the etch rate through the oxalic acid-grown AAO pores. It should be noted that the oxalic acid-grown AAO has pore diameters over 2 times larger than the sulfuric acid-grown AAO (50 nm compared to 20 nm), although both have similar aspect ratios of about 10:1. In short, regardless of the similar aspect ratios of the AAO shadow masks, the etch rate was seen to be a function of the feature size and decreases when etching through smaller holes.

5.4.3 Evaporated Al/Si AAO Masks

Finally, unordered nano-hole arrays were fabricated into Si by anodizing Al deposited onto Si(100) substrates directly and fluorine etching through the nano-pores of these unordered AAO masks. The growth of the AAO directly on Si is similar to the work described in Chapter 3 and follows the previous work of Crouse *et al.* [61]. First, a roughly 100 nm thick film (rather than the 2 μm thick film described in Chapter 3) of 99.99% Al was thermally evaporated in a vacuum of 8 x 10^{-7} Torr on 1-10 ohm cm n-type Si(100) substrates. The Si backsides and edges were coated in black wax and the Al films were anodized in 0.3 M oxalic acid at 40 V at 5 ^{o}C. After roughly 40 s, the current

decreased substantially and the anodization was complete. The films were then subjected to a pore widening and barrier layer removal etch consisting of a 5 wt % solution of phosphoric acid at 30 ^{o}C for 30 minutes. The unordered, as-grown AAO/Si samples were heated to 400°C and exposed to the fluorine beam for times between 2 to 4 minutes. In this case, the AAO films were not intentionally removed from the Si substrates but in some cases, the pieces of the AAO films peeled away (possibly due to stress) revealing the underlying Si beneath.

Figure 5.6 (a) shows a top down SEM micrograph of the results. The AAO film grown directly on Si is shown on the left hand side of the image, while the underlying nano-hole pattern transferred into the Si substrate is shown on the right hand side of the image. As expected, the AAO consists of an unordered array of nano-holes and is shown in more detail with the higher magnification, top down SEM image in Figure 5.6 (b). From the image, some of the nano-pores appear to be totally or partially blocked which is consistent with meandering or migrating pore growth during the single anodization step resulting in non-straight or "kinked" cross-sectional pore profiles. This situation would lead to less than ideal pattern transfer which can be seen in the Si substrate on the right hand side of Figure 5.6 (a) and verified in the SEM micrograph of Figure 5.6 (c) which shows a top down, close up view of the Si surface. In this image, it appears that the AAO nano-hole pattern only partially transferred into the Si substrate and some of nano-holes appear deeper than others. In addition, the nano-holes that did transfer into the Si(100) substrate are starting to merge together as a result of trench widening or undercutting during etching. It is also interesting to note that the nano-holes are partially square-shaped but still decidedly more circular than the previous examples of fluorine etching

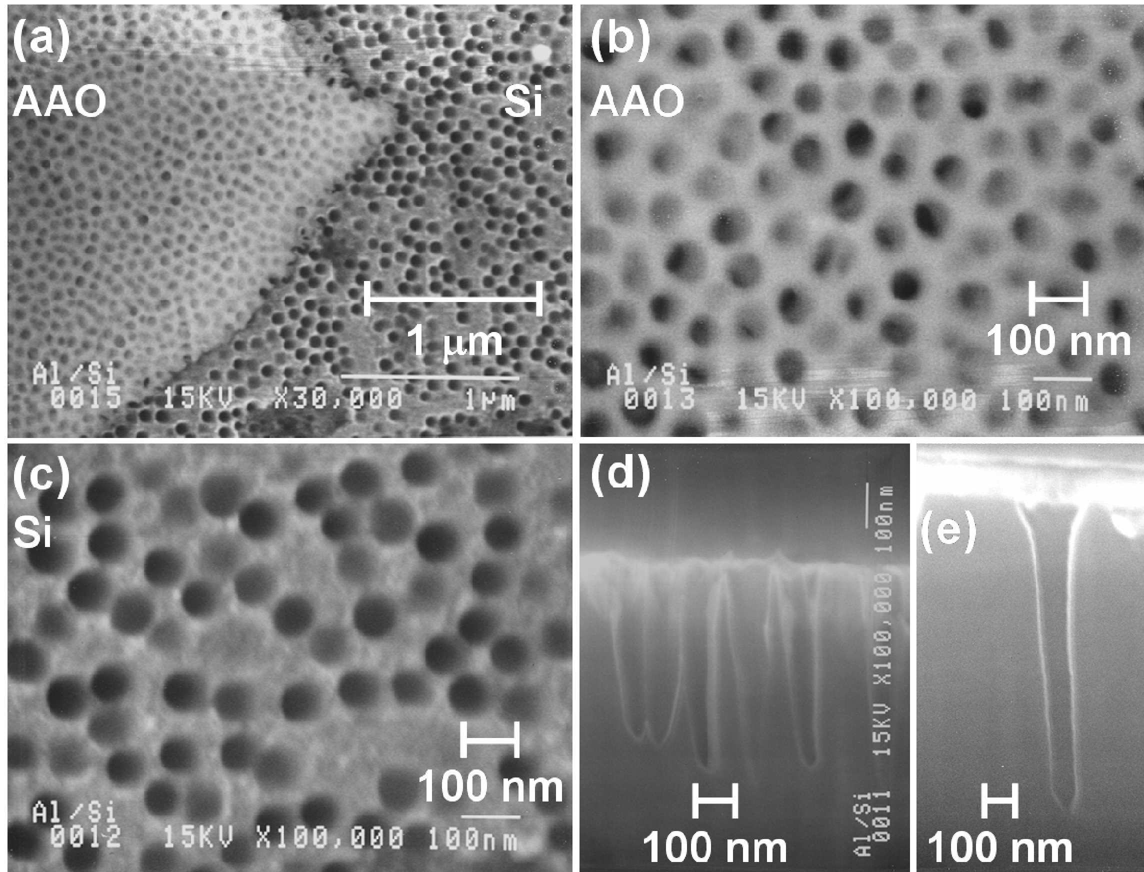

Figure 5.6. (a) Top down SEM micrograph of fluorine etched nano-hole array in Si(100) fabricated using an AAO mask grown directly onto Si. The left hand side of the image shows the unordered AAO mask while the right hand side of the image shows the exposed Si. (b) Top down close up SEM micrograph of the unordered AAO mask grown by anodizing deposited Al on Si(100). (c) Top down close up SEM micrograph of the unordered Si nano-hole array. (d) Cross-sectional SEM view of nano-hole profiles etched for 2 min. (e) Cross-sectional SEM view of nano-hole profile etched for 4 minutes. Note AAO film is still present.

through AAO masks into Si(100). This may be due to the fact that in this case the seeding pattern consisted of an unordered array of non-circular, elliptical-shaped pores. This anisotropy in the hole shape and position could tend to obscure the natural tendency of the F-Si(100) etching mechanism to produce square-shaped holes.

Figures 5.6 (d) and (e) show cross-sectional SEM micrographs of the resulting nano-hole profiles for similar samples, fluorine etched for 2 and 4 minutes, respectively. Figure 6 (d) shows roughly 50 nm wide, 400 nm deep holes (illustrating an aspect ratio of ~ 8:1) while Figure 6 (e) shows a single 100 nm wide, 700 nm deep hole (an aspect ratio

of ~ 7:1). Note that the nano-holes in Figure 5.6 (d) are touching and etching longer would have merged these holes together. This was observed in much of the 4 minute etched sample shown in Figure 5.6 (e) except for isolated examples of single nano-holes where the surrounding nano-hole pattern did not transfer through the unordered, kinked AAO mask. This allowed the hole in Figure 5.6 (e) to widen to roughly 100 nm since there were no surrounding holes to merge with. Both of these images illustrate that fairly high aspect ratio structures (compared to aspect ratios of ~ 2 for Ar^+ ion etching and ~ 3 for RIBE) with steep sidewalls could be etched using this method. There appears to be some widening at the top of the holes (particularly the one shown in Figure 6 (e)). This could be due to undercutting from the fluorine etch but may also have occurred prior to etching during the anodization step which in some instances has been observed to attack the highly doped Si [61].

5.5. CONCLUSION

Ordered and unordered nano-hole arrays were fabricated by utilizing dry etching techniques to etch through AAO masks lifted off onto various substrates (GaAs, InSb, and Si). The dry etching techniques investigated were Ar^+ ion etching, Cl_2 RIBE, and atomic fluorine beam etching. Combining these methods with sulfuric acid and oxalic acid-grown AAO films allowed the fabrication of ordered and unordered nano-hole arrays with diameters ranging from around 20 nm to 100 nm and hole-to-hole spacings ranging from roughly 60 nm to 100 nm. The best pattern transfer results in terms of replicating the circular pores of the AAO mask were achieved by Ar^+ ion etching, a purely physical etching method, but the cross-sectional profiles produced were triangular

with significant sidewall tapers. In addition, re-deposition effects limited the ultimate depth attainable using this technique to about 120 nm, or an aspect ratio of roughly 2:1. RIBE, combining both physical and chemical etching, produced nano-hole arrays that were not as circular as the AAO nano-pores, but the cross-sectional profiles produced had steeper sidewalls and flatter bottoms. In this case, slightly deeper holes could be etched and thus larger aspect ratios of around 3:1 were attainable. Finally, fluorine etching through AAO masks on Si produced hexagonally close-packed, square-shaped or triangular-shaped nano-hole arrays depending on the Si orientation (Si(100) or Si(111)). These shapes were a result of the anisotropic and purely chemical F-Si etching dynamics resulting in certain planes of Si being preferentially etched faster than other planes. Consistent with the results found in Chapter 2, the cross-sectional profiles produced were highly dependent on the Si substrate temperature with steeper sidewalls being produced at higher temperatures. Nano-hole arrays etched through AAO grown directly on Si produced profiles with fairly steep sidewalls and aspect ratios around 8:1, the highest aspect ratios attainable out of the three dry etching techniques investigated. However, the aspect ratio was ultimately limited by the nano-holes merging together due to a combination of undercutting during etching and the close-packed nature of the AAO nano-pores. Finally, these nano-hole arrays have potential applications in device structures (e.g. Chapter 7) and nano-meshes for filtration and sensor arrays (e.g. Chapter 6). In addition, the periodicity and diameter of these nano-hole arrays are in a size regime that make them promising candidates for use as 2D photonic crystals for enhanced light extraction from III-nitride UV LEDs [67, 68].

Chapter 6

Fabrication and Characterization of Si Nano-Meshes

6.1. ABSTRACT

Free-standing silicon nano-meshes have been fabricated on silicon-on-insulator (SOI) substrates using a combination of photolithography, wet-anisotropic etching, porous alumina templates, and dry etching techniques. Such nano-meshes could have possible uses for nano-filtration and sensor array applications. First, using a combination of photolithography and anisotropic wet etching, windows were patterned into the backside of the SOI substrates up to the thin SiO_2 layer. Next, AAO templates were used as contact or shadow masks to transfer a well-ordered nano-hole pattern into the top Si layer using an argon ion beam or an atomic fluorine beam etch. As shown in Chapter 5, depending on the dry etch used and the crystalline orientation of the silicon substrate, this leads to a hexagonal close packed array of either circular, square, or triangular holes with

dimensions on the order of 20-50 nm. After transferring the well-ordered, AAO nano-hole array pattern, the thin SiO_2 layer was removed in the open window regions by a wet etching step. The resulting structure consisted of a free standing, ultra-thin (50 nm thick) Si nano-mesh with an array of well-ordered nanometer-sized through-holes. Finally, these silicon nanostructures were further downshifted in size by the use of a pattern dependent and self-limiting oxidation step, which oxidizes the outer Si matrix, leaving behind sub-15nm silicon cores. Photoluminescence (PL) spectra taken on these structures at 77K reveal broad peaks in the 600-1000 nm wavelength range, indicative of quantum confinement effects in the nanostructured Si.

6.2. EXPERIMENTAL DETAILS

The SOI substrates used in this work consisted of a 50 nm thick layer of Si on top of a 50 nm thick layer of SiO_2 on a bulk Si substrate as shown schematically in Figure 6.1 (a). At the start, these SOI substrates underwent a combination of polishing, photolithography, and anisotropic Si wet etching to pattern roughly 40 μm square windows in the backside of the bulk Si substrates. These windows extended all the way to the 50 nm thin SiO_2 layer near the top surface as shown in Figure 6.1 (b). The processing steps involved in this procedure were developed in collaboration with another graduate student and details of this process will be described fully in his thesis [69]. The purpose of this step was two-fold: 1) it allowed for transmission electron microscopy (TEM) characterization of these structures and 2) was an essential step in isolating these Si nanostructures to create truly free-standing Si nano-meshes.

Next, AAO templates prepared by a two-step anodization technique [59] were lifted off onto the top Si surface following the same general steps discussed in previous chapters. In this case, both anodic oxidation steps were carried out in a 0.3 M solution of aqueous oxalic acid at 40 V and a temperature of 10 ^{o}C. This was designed to give well-ordered, hexagonally close-packed pores 50 nm in diameter spaced 100 nm apart. After the second 5 minute anodization, through-hole masks approximately 500 nm thick were prepared by separating the AAO films from the Al foils in a saturated $HgCl_2$ solution and removing the remaining alumina barrier layers at the bottom of the pores in a 5 wt% solution of H_3PO_4 at 30 ^{o}C for about 35 minutes. The resulting AAO masks, which were roughly 3 mm by 3 mm in size, were placed on the top Si surface of the specially prepared SOI substrates as shown in Figure 6.1 (c).

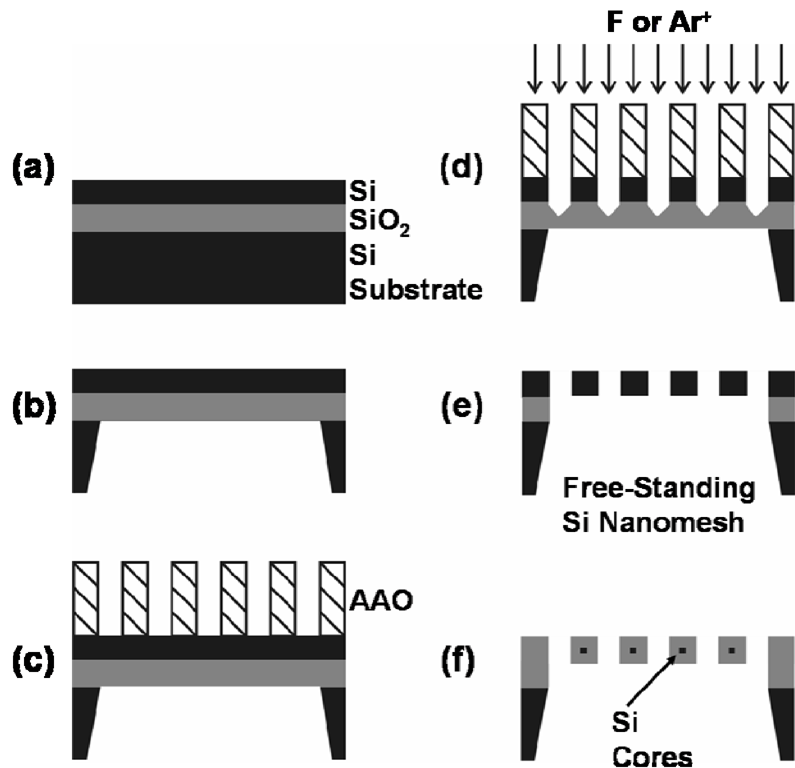

Figure 6.1. Schematic showing sample processing steps: (a) Sample consists of 50 nm Si on 50 nm SiO_2 on a Si wafer. (b) Photolithography and Si wet etching to open up ~ 40 μm windows in the back side of Si substrate up to the SiO_2 layer. (c) AAO mask placed on top surface of sample. (d) F-atom or Ar^+ etching to transfer pattern into top Si layer and etch into SiO_2 layer. (e) HF wet etching to remove AAO mask and etch away SiO_2 layer creating free-standing Si nano-mesh. (f) Self-limiting oxidation step done at 875°C for 2 hours to reduce the size of the remaining oxide-encased Si cores to a sub-15 nm range.

The AAO nano-hole array pattern was then transferred into the underlying Si layer using either a 500 eV Ar^+ ion beam (VG Microtech EX05 ion source) or a 1 eV neutral atomic fluorine beam to etch the exposed silicon. In both cases, the etching time was carefully controlled to etch completely through the 50 nm thick layer of Si and partially into the 50 nm thick SiO_2 layer as shown in Figure 6.1 (d). The samples exposed to the 500 eV Ar^+ beam were etched in a UHV environment (~5 x 10^{-10} Torr background, ~10^{-6} Torr with the beam on) with a source to sample distance of 50 mm and an angular divergence of about 0.1^o. The beam had a current density of 0.05 ma/cm^2 and the samples were etched for 90 minutes. The samples exposed to the 1 eV atomic fluorine beam were etched in an HV environment ($5x10^{-6}$ Torr background, $2x10^{-5}$ Torr with the beam) and were maintained at temperatures between 250 ^oC and 350 ^oC (the Si etch rate exhibits an Arrhenius-type dependence on the substrate temperature) and etched for times around 1 minute. For more details on the atomic fluorine source and etching of silicon related materials refer to Chapters 2 and 5.

After the dry etching steps to transfer a nano-hole array pattern into the top Si surfaces, the samples were placed in a 10:1 buffered oxide etch (BOE) for 15 minutes. This step, shown schematically in Figure 6.1 (e), served to etch away both the 50 nm thick SiO_2 layer as well as the AAO mask. Releasing the 50 nm thick nano-patterned Si layer from the SiO_2 layer was the final step in creating free-standing Si nano-meshes.

The resulting dimensions of the Si nano-meshes (50 nm thick with roughly 50 nm wide Si bars or wires surrounding the nano-holes), are too large to show any quantum mechanical size effects such as those argued to be seen in electro-chemically produced porous-Si [3, 4]. As discussed briefly in Chapter 1, porous-Si structures appear to show

size-dependent PL in the visible spectrum when feature sizes approach the sub-10nm range corresponding nicely with the expectation of the onset of quantum confinement effects in Si structures from the simplistic "particle-in-a-box" model presented in Chapter 1. In an effort to explore this size regime, techniques were investigated to further reduce the Si feature sizes in these Si nano-meshes. One such method, the oxidation of non-planar Si surfaces, has recently demonstrated the ability to reduce the size of a regularly-sized starting pattern of Si structures (dots, wires, etc.) in a highly uniform and reproducible manner [70-74].

As studied by others [73, 74], the oxidation of non-planar surfaces of Si show a self-limiting and pattern dependent oxidation effect below about 950 ^{o}C attributable to the stress resulting from the material expansion of the grown oxide (unit cell volume of SiO_2 is ~ 45 $Å^3$ while the unit cell volume of Si is ~ 20 $Å^3$). In the case of the oxidation of planar Si surfaces, the resulting stress exists in the plane parallel to the Si/SiO_2 interface and relaxes in the growth direction as the existing oxide layer is pushed away. With the introduction of curved Si surfaces, a component of stress exists perpendicular to the Si/SiO_2 interface. As a consequence, extra work is required to make room for the grown oxide. As the oxidation continues, the core Si structure continues to shrink, resulting in an increasing radius of curvature and increasing stress component perpendicular to the interface. Below an oxidation temperature of about 950°C, a critical stress is reached causing the oxidation reaction to stop before all of the Si is fully consumed. The final size of the oxide-encased Si structures depend both on the initial size of the Si structures as well as the initial geometry [73, 74].

For the Si nano-meshes fabricated in this work, the nano-mesh was viewed as a mesh of intertwining Si wires lying in a plane parallel to the surface. Taking the initial diameters of these Si wires as 40-50 nm and using the published data of Liu et.al. [71] for the self-limiting oxidation of Si nanowires (patterned and fabricated perpendicular to the surface), an initial estimate of the oxidation parameters were chosen to reduce the size of the Si wires to a sub-10 nm regime. In particular, the Si nano-mesh samples underwent an oxidation step in a dry O_2 environment at 875 ^oC for two hours. In addition to reducing the size of the Si nanostructures, encasing them in oxide also served to significantly reduce the number of Si dangling surface bonds (especially when compared to porous-Si), an important step for the optical characterization of these structures. The resulting final structure after the oxidation step is shown schematically in Figure 6.1 (f).

6.3. RESULTS AND DISCUSSION

6.3.1 Electron Microscopy Results

Top down SEM micrographs of nano-hole arrays on SOI substrates are shown in Figure 6.2. Figure 6.2 (a) shows an SEM micrograph of a fluorine etched SOI sample (with a bulk Si(100) substrate) after removal of the AAO mask. In this case, no windows were opened up in the backside of the substrate and the thin SiO_2 layer was not removed to allow for convenient SEM observation. The square-like grid array is the result of the anisotropic nature of the fluorine-silicon etching dynamics and is similar to the results shown in Chapter 5 for fluorine etched Si(100) nano-hole arrays. The cross-sectional SEM micrograph inset shows the Si nano-hole array with the 50 nm thick oxide layer still intact. Note that in this case, the fluorine etching time (1 min. 20 sec) was insufficient to

allow penetration into the underlying SiO_2 layer. Figure 6.2 (b) shows an SEM micrograph of an Ar^+ etched SOI substrate after removal of the AAO mask. Similar to the sample shown in Figure 6.2 (a), no windows were opened up in the backside of the substrate. However, the sample was subjected to the BOE step to remove the 50 nm oxide layer. In this case, the nano-holes are circular and are similar to the results of the Ar^+ etched Si nano-hole arrays shown in Chapter 5. The near cross-sectional SEM micrograph inset shows the 50 nm SiO_2 layer to have been completely removed by the BOE etch. Note that with the removal of this SiO_2 support layer, the top patterned Si layer has collapsed and touches the bottom Si substrate as the layer extends horizontally from its anchor position, i.e. from the unpatterned SOI region of the substrate. This illustrates the need to remove the back substrate to create truly free-standing nano-meshes.

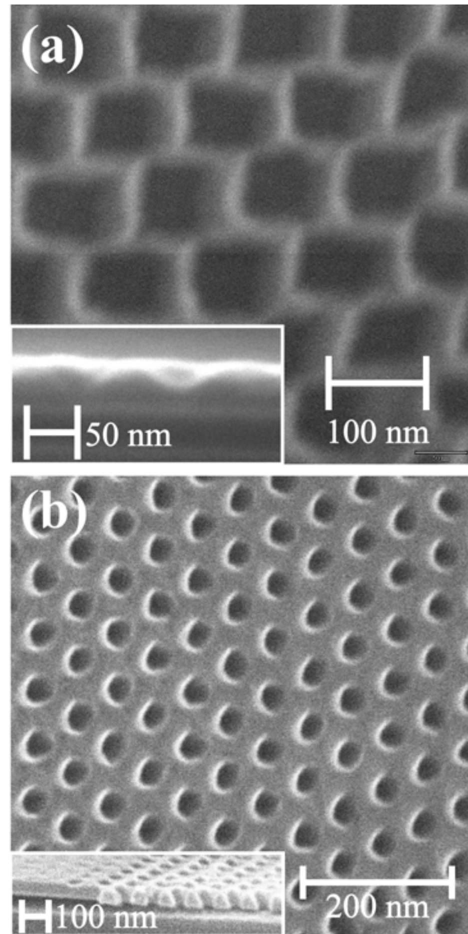

Figure 6.2. Top down SEM micrographs of nano-hole arrays in SOI substrates. (a) fluorine etched SOI nano-hole array. Inset shows cross-sectional view. (b) Ar^+ etched SOI nano-hole array after removal of the SiO_2 layer. Inset shows near cross-sectional view.

Figures 6.3 (a) and (b) show a scanning electron image (SEI) and transmitted electron image (TEI), respectively, taken at the same position on the sample of an Ar^+ ion etched free-standing Si nano-mesh processed up to the step shown in Figure 6.1 (e). The average nano-hole diameter from the SEI image (which takes into account the top surface

of the holes) is approximately 48 nm while the average nano-hole diameter from the TEI image (which takes into account the diameter from the other side of the holes) measure approximately 60 nm. This allows the calculation of the taper of the cross-sectional hole profile to be about 7° as measured from the plane perpendicular to the sample surface (inset of Figure 6.3 (b)), in good agreement with cross-sectional SEM results seen in Chapter 5 for Ar^+ etched Si hole profiles. Figures 6.3 (c) and (d) show SEI and TEI images, respectively, taken at the same position on the sample of an Ar^+ etched free-standing Si nano-mesh that has undergone a self-limiting oxidation step (Figure 6.1 (f)). The SEI image shows the nano-hole array with 100 nm hole-to-hole spacings but with indistinct, fuzzy holes, possibly due to oxide charging effects. In contrast, the TEI image clearly shows the presence of oxide rings surrounding the nano-holes with intertwining Si wires surrounding both the holes and oxide rings. The oxide rings are roughly 15 nm thick on average (in the plane dimensions) and are

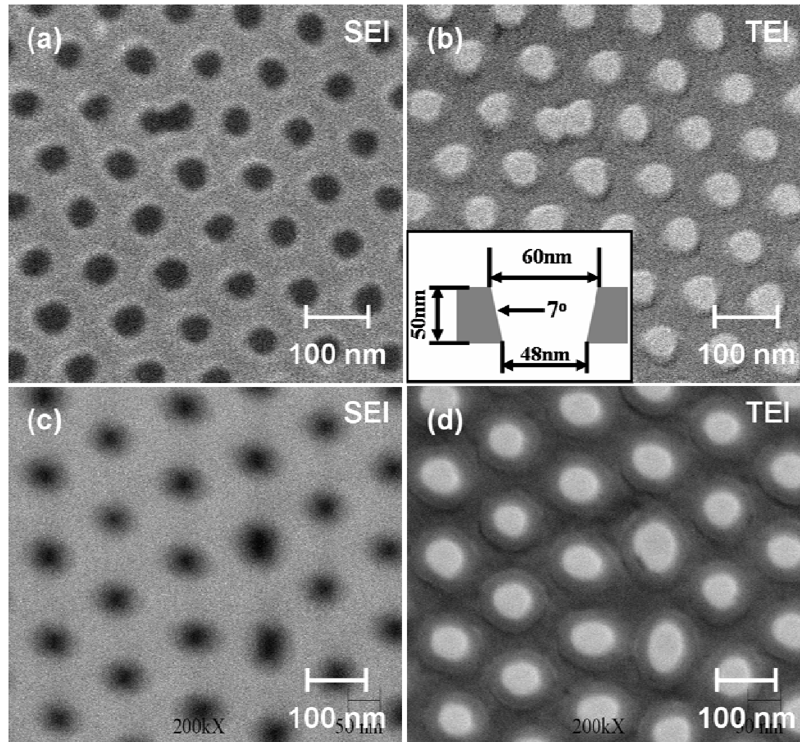

Figure 6.3. (a) SEI image of free-standing Ar^+ ion etched Si nano-mesh. (b) TEI image at the same position. Inset shows the taper angle of the nano-hole profiles calculated from the diameters of the SEI and TEI images. (c) SEI image of oxidized, free-standing Ar^+ etched Si nano-mesh. (d) TEI image at the same position. Note the presence of oxide rings surrounding the nano-holes.

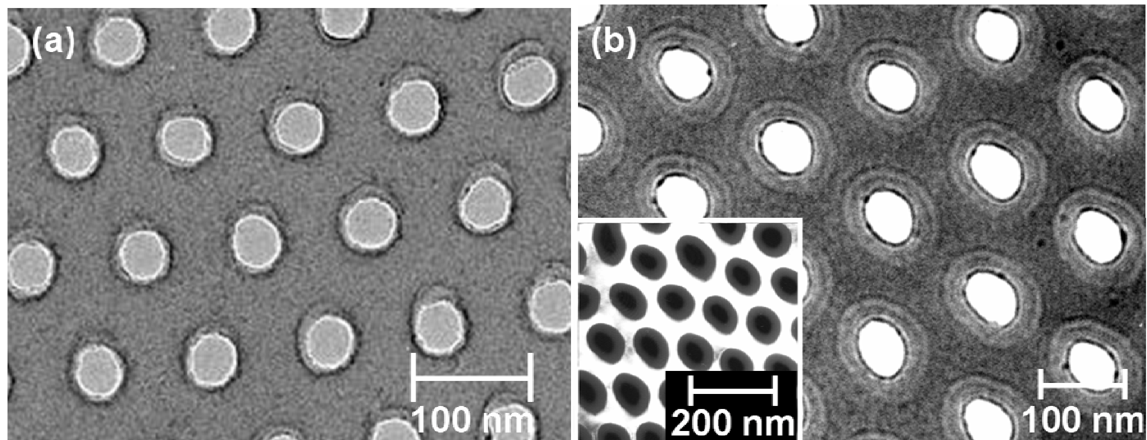

Figure 6.4. Bright field TEM images of: (a) free-standing, Ar^+ etched Si nano-mesh. (b) free-standing, Ar^+ etched, oxidized Si nano-mesh. Note the presence of oxide rings surrounding the nano-holes. Inset shows a dark field TEM image of the oxidized nano-mesh indicating the amorphous nature of the oxide rings.

close to touching each other in some spots. The lateral dimensions of the Si wires in between the oxide rings vary anywhere from close to zero (where the oxide rings touch) up to 30 nm in some regions.

Figures 6.4 (a) and (b) shows bright field TEM images of free-standing Ar^+ etched nano-meshes before and after the self-limiting oxidation step, respectively. Prior to the oxidation (Figure 6.4(a)), the free-standing Si nano-mesh consists of 40-50 nm diameter nano-holes spaced 100 nm apart, in fairly good agreement with the AAO shadow mask. The nano-mesh after oxidation, Figure 6.4 (b), again shows oxide rings roughly 15 nm in lateral thickness. The inset in Figure 6.4 (b) is a dark field TEM image of the oxidized nano-hole array confirming the amorphous nature of the oxide rings (dark contrast) and the crystalline nature of the surrounding Si mesh (bright contrast).

Figures 6.5 (a) and (b) shows high resolution TEM images near a single nano-hole of a free-standing, Ar^+ etched Si nano-mesh before and after the self-limiting oxidation step, respectively. In both images, the nano-hole is in the upper left hand corner. The un-oxidized nano-mesh shown in Figure 6.5 (a) shows very little amorphous Si or SiO_2

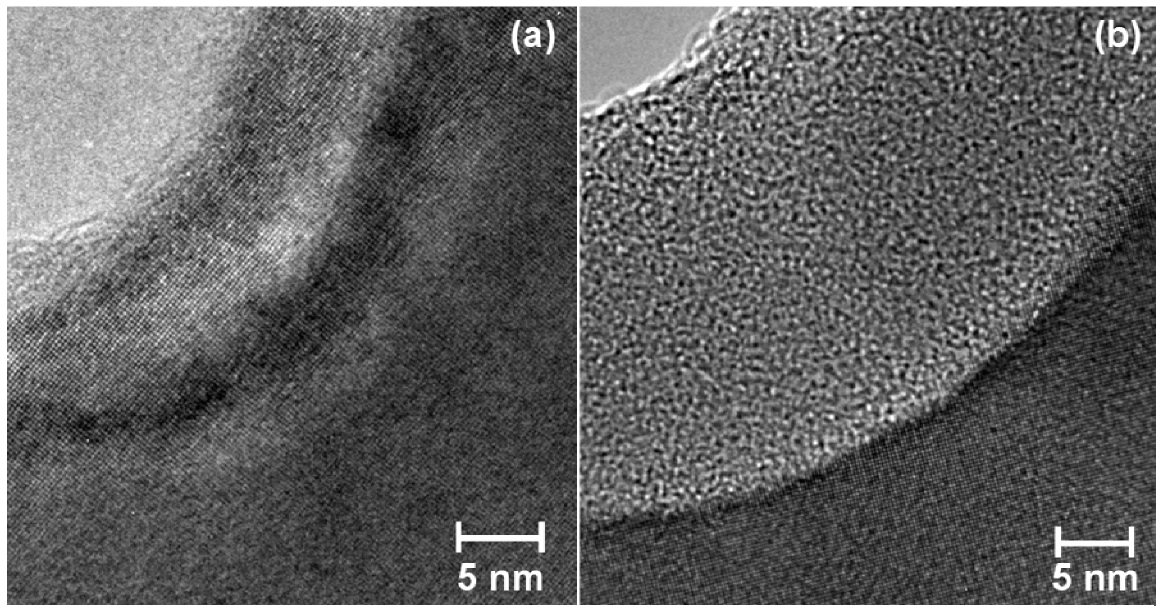

Figure 6.5. High resolution TEM images of: (a) free-standing, Ar^+ etched Si nano-mesh near a single nano-hole. (b) free-standing, Ar^+ etched, oxidized Si nano-mesh near a single nano-hole. The nano-hole is in the upper left corner in both images.

surrounding the nano-hole prior to the oxidation step. After the oxidation step, however, the nano-mesh shown in Figure 6.5 (b) has a clearly visible amorphous oxide ring surrounding the nano-hole with a lateral thickness around 28 nm.

The lateral dimensions of the oxide rings and Si wires (i.e. the dimensions in the plane of the nano-mesh) were determined from the TEM images above. The thickness (i.e. the dimension perpendicular to the plane of the nano-mesh) of the Si wires in the oxidized nano-meshes was determined using quantitative convergent beam electron diffraction (CBED). In CBED, the primary electron beam from a conventional TEM is focused to a small spot on the sample surface and the resultant thickness-dependent diffraction intensity from various crystal planes is analyzed. In this case, electrons were diffracted off of the amorphous oxide encased crystalline Si and the intensity of the diffraction spots from known Si crystal planes was measured. Using known parameters of Si and an initial assumption of the Si thickness, the diffraction intensity of the spots was calculated and compared to the experimental data. An iterative approach was then

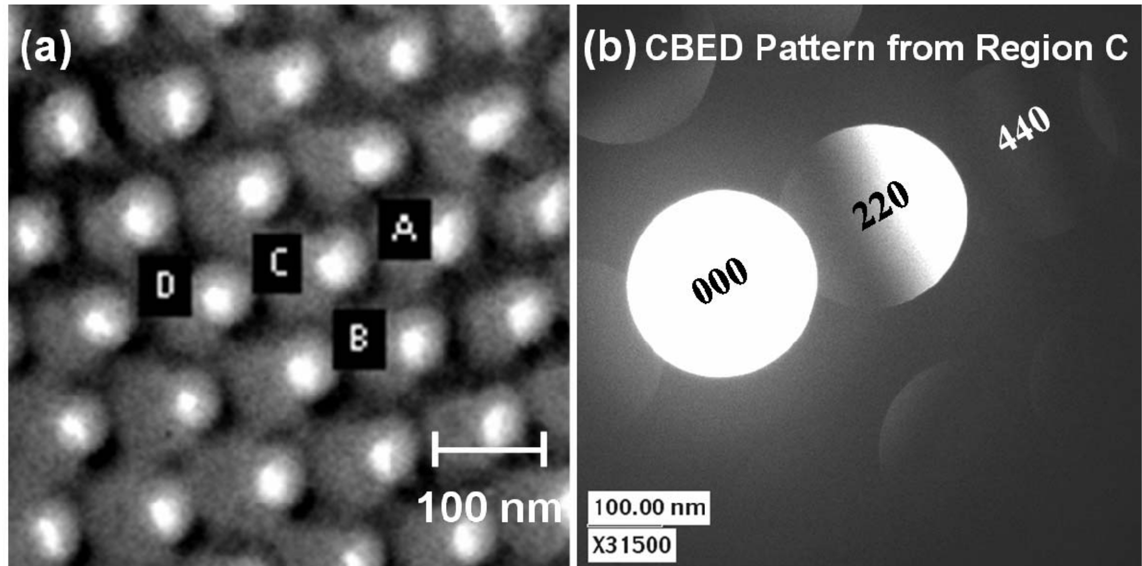

Figure 6.6. (a) TEM image of oxidized Si nano-mesh. Letters indicate spots where CBED took place. (b) Typical CBED pattern (from region C) used to calculate the thickness of the oxide encased Si wire mesh.

used to refine and fit the theory to the experimentally determined intensity to determine the thickness of the Si in the plane perpendicular to the electron beam. Figure 6.6 (a) shows a TEM image of an oxidized Si nano-mesh sample where the letters A, B, C, and D show the positions where the CBED took place. Figure 6.6 (b) shows a typical CBED image from region C where the diffraction spots from particular crystal planes are noted and the varying intensity of these diffraction spots are apparent. Using this technique, the thickness of the SiO_2 encased Si core wires in the regions indicated was found to be: 12.1 ± 0.4 nm (Region A), B 14.0 ± 1.0 nm (Region B), 13.7 ± 1.0 nm (Region C), and 15.3 ± 1.0 nm (Region D). The average Si thickness in the four spots where the CBED too place is 13.8 nm which is equivalent to 18 nm of oxide on both the top and bottom surfaces of the nano-mesh. This is similar to the lateral oxide ring thickness around the nano-holes.

6.3.2 Photoluminescence of Si Nano-meshes

In an effort to investigate any quantum confinement effects in the Si nano-crystals, PL measurements were obtained at 77K on both fluorine and Ar^+ etched, oxidized and un-oxidized Si nano-mesh samples using a 532 nm, 10 mW excitation source. PL spectra were also collected on control samples consisting of oxidized and unoxidized SOI substrates (i.e. no nano-hole array pattern). The 532 nm laser was focused to a spot size of roughly 100 μm and directed to the area of interest on the samples. Standard collection optics were used to direct the signal to a CCD spectrometer which collected the signal over a range of 550 to 1000 nm.

Figure 6.7 shows the normalized PL spectrums from the samples taken at 77K. The top axis indicates an estimate of the expected Si feature size from the PL output, culminated from both theoretical and experimental work involving nano-crystalline Si and porous-Si [4, 5]. Figures 6.7 (a) and 6.7 (b) show the PL spectra taken from oxidized, fluorine etched and Ar^+ etched Si nano-meshes, respectively. Both oxidized nano-meshes show very broad, weak peaks in the visible spectrum. The fluorine etched, oxidized nano-mesh exhibits a peak in the PL centered around 800 nm (1.5eV) with a full-width-half-maximum (FWHM) around 275 nm, while the Ar^+ etched oxidized nano-mesh has a peak near 600 nm (2eV) with a FWHM around 100 nm. In addition, there appears to be a smaller, secondary peak in the Ar^+ etched sample around 975 nm with a FWHM of around 125 nm. Neither the un-oxidized, fluorine etched Si nano-mesh (Figure 6.7(c)) or the un-oxidized, Ar^+ etched Si nano-mesh (not shown) show any PL emission. Finally, the oxidized SOI control sample (Figure 6.7(e)) and the un-oxidized SOI control sample (Figure 6.7 (e)) show no PL output as well. In each case, the spectrums were repeatable and multiple spectrums were taken on each sample.

The origin of the weak PL emission from the oxidized Si nano-meshes is assumed to come from a quantum confinement effect of the oxide encased silicon wire cores. Depending on the growth specifics, SiO_2 grown in dry oxidation steps can have a PL band around 620 nm-560nm [75] while oxygen excess silicon oxide (such as can

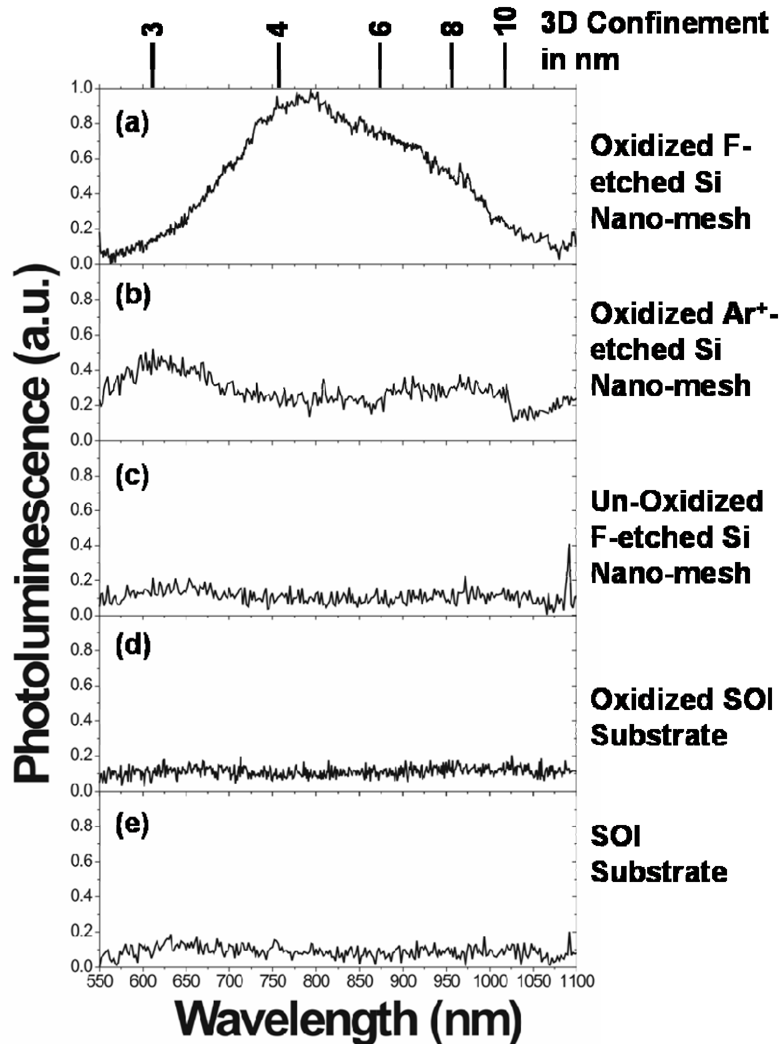

Figure 6.7. Photoluminescence spectra taken at 77K of: (a) oxidized, fluorine etched Si nano-mesh (b) oxidized, Ar^+ etched Si nano-mesh (c) Un-oxidized, fluorine etched Si nano-mesh (d) oxidized SOI substrate and (e) SOI substrate.

occur in ion implanted SOI) can have a PL band around 650 nm [75]. These bands are near the 600 nm peak seen in the Ar^+ etched Si nano-mesh, however, no similar peak or any PL emission at all is seen in the oxidized and un-oxidized SOI control samples. The argument for a possible quantum confinement effect is further strengthened by the lack of PL emission on the un-oxidized Si nano-mesh samples which have Si dimensions (on the order of 50 nm) that are still too large for quantum confinement effects to be apparent at

77K. Comparing with previous nano-crystalline and porous-Si work (top axis of Figure 7), the PL emissions would seem to indicate a broad size range centered around roughly 5 nm for the fluorine etched, oxidized nano-mesh and 3 nm (the 600 nm peak) for the Ar^+ etched, oxidized nano-mesh. The broad width of the PL peaks, which are comparable to porous-Si PL FWHM, [3] are most likely a result of the broad size distribution of the Si nano-wires. This is partially confirmed in the TEM images of the Ar^+ etched Si nano-meshes which indicate lateral dimensions of the Si wires vary between 0 (in regions where the oxide rings touch) and 30 nm. Although not confirmed by TEM, these non-uniformities could be even more pronounced in the fluorine etched oxidized nano-mesh due to the anisotropic nature of the fluorine-silicon etching dynamics leading to a possibly larger distribution of sizes in this nano-mesh as indicated by the PL spectra.

It is interesting to compare this work with that of Liu, et *al.* who also saw similar PL results after a self-limiting oxidation step of sub-50 nm Si pillars fabricated with electron beam lithography and reactive ion etching perpendicular to the sample surface [70]. After oxidation of these sub-50 nm Si columns, TEM micrographs indicated sub-5 nm Si cores encased in oxide. PL spectra taken on such a sample showed a broad peak around 650 nm with a FWHM around 100 nm, comparable to the Ar^+ etched, oxidized nano-mesh. As in this work they noted their low PL intensity (~ 400 times lower than strongly luminescent porous-Si) which was attributed to the relatively small pattern density (2.5×10^9 cm^{-2}) of Si columns in their two dimensional array as compared to porous-Si samples. The Si nano-mesh samples prepared in this work also consist of a two-dimensional array, differing from the Si columns fabricated by Liu et *al.* in that the samples consist of inter-meshing wires parallel to the substrate with a nano-hole density

of approximately 10^{10} cm^{-2}. Both of these cases, however, are significantly different from a three-dimensional porous-Si sample which has a much larger geometric cross section for absorbing the incident photons.

Finally, it should also be noted that the presence and role of intrinsic crystalline defects in the top Si layer, dangling bonds (which can act as centers for non-radiative recombinations), and surface effects (associated with from surface contaminants, etc.) on the PL spectra is unknown. Future work will focus on fabricating smaller nano-mesh samples (using sulfuric acid-grown AAO films) for further PL characterization as well as electron energy loss spectroscopy measurements.

6.4. CONCLUSION

Free-standing nanometer-sized silicon meshes have been fabricated on SOI substrates using a combination of photolithography, wet-anisotropic etching, porous alumina templates, and dry etching techniques. The resulting structure consists of an array of holes (square or circular) with approximately 50 nm diameters and 100 nm spacings. Such nano-meshes have possible applications for nano-filtration and chemical/molecular sensor arrays. These Si nano-meshes were further reduced in size by a pattern dependent and self-limiting oxidation step which left behind oxide-encased Si wires with sub-15 nm dimensions. PL spectra from these structures showed broad, weak peaks indicative of quantum confinement effects.

6.5 ACKNOWLEGMENTS

The author wishes to acknowledge Mr. M. Curtis, a graduate student in the department of Physics and Astronomy at the University of Oklahoma, for his help in developing the process for opening up the windows in the back side of the SOI substrates, Dr. G. Lian, a post-doc in the Department of Physics and Astronomy at the University of Oklahoma, for the TEM and CBED results of the Si nano-meshes (taken on a JEOL200FX at the University of Oklahoma and a LEO912 at Oak Ridge National Labs SHaRE User Center), and Drs. M. Xiao and X. Wang from the University of Arkansas for their help in obtaining the PL measurements. The author would also like to thank Shanghai SIMGUI Technology Co., Ltd., China for providing the SOI wafers used in this work.

Chapter 7

Fabrication and Characterization of Array of MOS-Type Nano-Capacitors

7.1. ABSTRACT

MOS-type nano-capacitor structures were fabricated by etching a highly ordered array of nano-holes through an AAO mask into a silicon oxide/silicon nitride on silicon substrate before growing a thermal oxide on the exposed silicon and using either a poly silicon gate or an electrolyte contact. This technique allowed good pattern transfer over a large area (~3mm by 3mm) which in principle could be scaled up to even larger dimensions. Room temperature *C-V* measurements on these structures showed little leakage. Moreover, capacitance values for the electrolyte contact indicated that only the exposed silicon area contributed to this capacitance.

7.2 INTRODUCTION

There is a growing interest in the fabrication of nanometer-sized structures due to their potential use in high-density memories, single electron devices, vertical transistors and optoelectronic devices. Conventional techniques used to fabricate such structures have generally used electron-beam lithography or scanning probe methods to transfer nanometer-sized patterns into various substrates. These methods suffer from a wide variety of problems that limit their use in practical applications, most notably because they are serial rather than parallel processes. Recently, anodized aluminum oxide (AAO) has received much attention due to its potential use in fabricating ordered arrays of nanometer-sized structures in combination with more conventional parallel processing techniques [49]. As discussed in previous chapters, the structure of AAO consists of ordered hexagonal arrays of pores with diameters that can range from about 20 nm to 0.25 μm, depending on the anodizing conditions. These properties make AAO films a promising candidate for the fabrication of many structures such as high-density magnetic memory elements, optoelectronic devices and quantum dot arrays [76-79]. Different methods using AAO films to transfer patterns into silicon based substrates have been reported in the literature [61-63, 80]. However, various issues arise leading to problems in pattern transfer and profiles at the bottom of etched holes or trenches as illustrated in Chapter 5 and investigated by other researchers. For example, on AAO films fabricated in aluminum deposited directly on silicon, there are problems due to the existence of the barrier layer at the bottom of the AAO [61, 62]; the introduction of an alloy layer between the aluminum and the substrate [61, 62]; and the problems with pattern transfer due to re-deposition effects [62]. Other problems result from a lack of

etch anisotropy, uniformity, and selectivity, leading to trenches or holes with rounded profiles and small aspect ratios [61-63, 80].

In this chapter, capacitance-voltage (*C-V*) characterization of a nano-array of metal-oxide-semiconductor (MOS) capacitors in Si was fabricated using AAO masks in collaboration with researchers at the University of North Carolina [81]. In particular, a reactive ion etching (RIE) step followed by a wet etch through a SiO_2/Si_3N_4 layer was used to achieve square nano-hole profiles at the silicon surface. This was followed by the growth of a thin gate oxide at the bottom of the holes leading to an array of nanometer-sized MOS-type structures. In this case, the conducting contact is achieved by using either poly-silicon or an electrolyte. In both cases room temperature C-V measurements indicated little leakage. In the electrolyte case, capacitance values indicate only the thin gate oxide at the bottom of the holes contributes to this capacitance.

7.3. EXPERIMENTAL DETAILS

Sample processing starts with an AAO film fabricated using a two-step anodization process on a pure (99.999%) Al foil (see Chapter 3 and Ref. 58 for details) [59]. Both anodic oxidation steps were carried out in a 0.3 M solution of aqueous oxalic acid at 40 V and a temperature of 10 ^{o}C which was designed to give pores with dimensions of 50 nm in diameter spaced 100 nm apart. After the second anodization, a through-hole mask approximately 500 nm thick was prepared by lifting the film off of the Al foil in a saturated $HgCl_2$ solution and removing the bottom alumina barrier layer in a 5 wt % solution of H_3PO_4 at 30 ^{o}C for about 30 min. The resulting mask, which was roughly 3 mm by 3 mm in size, was then placed on a sample, consisting of 100 nm SiO_2

on 20 nm of Si_3N_4 on a silicon substrate, as shown schematically in Figures 7.1 (a) and (b). The AAO nano-hole array pattern was then transferred into the underlying substrate using a Semigroup reactive ion etching (RIE) 1000TP tool. First, the sample was cleaned using an oxygen plasma to remove any organic contamination resulting from the AAO mask fabrication/transfer process (12.5 sccm flow of O_2 at100 W and 60 mTorr). This was followed by a CHF_3/O_2 reactive ion etch step (20 sccm flow of CHF_3, 5 sccm flow of O_2 at 100 W and 60 mTorr). The etch time was carefully controlled by monitoring the sample etching rate so that the RIE process completely etched away the silicon oxide layer but only partially etched the silicon nitride layer, as shown in Figure 7.1 (c). Next, the remaining exposed nitride was removed by a short (2 minutes, 40 seconds) 90 wt % H_3PO_4 wet etch at 180 ^{o}C that also removed almost all of the AAO mask, as shown in Figure 7.1 (d). The phosphoric acid etch has a high selectivity for etching silicon nitride versus silicon oxide and leaves the silicon layer itself un-etched. This combination of dry and wet etching of the sample served two purposes: 1) It allowed the thin nitride layer to protect the silicon surface from

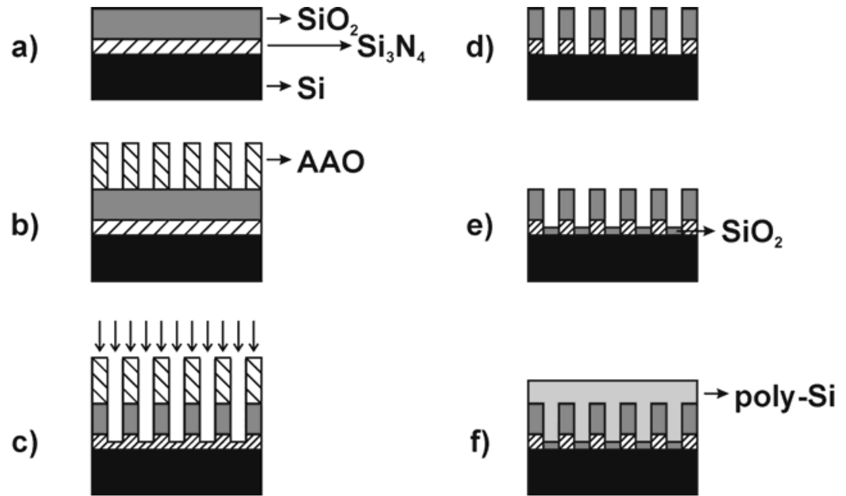

Figure 7.1. Cross-sectional schematic of processing steps: (a) Sample consisting of 100 nm SiO_2 on 20 nm Si_3N_4 on Si. (b) AAO mask lifted off onto the sample. (c) RIE etching through the SiO_2 and *into* the Si_3N_4 layer. (d) Removal of the Si_3N_4 layer (and the AAO mask) via a phosphoric acid wet etch. (e) 5 nm of SiO_2 thermally grown at base of holes. (f) Contacting of MOS-type structure with 100 nm of poly-Si or electrolyte.

the RIE step and 2) it leads to uniform side-wall profiles and flat bottoms after the wet etch. After the wet etch a 5 nm gate oxide was thermally grown on the exposed silicon hole bottoms at 800 ^{o}C for 15 minutes, as shown in Figure 7.1(e). Figure 7.1(f) shows the final MOS structure where a 100 nm thick layer of poly-Si was grown by chemical vapor deposition. Room temperature *C-V* measurements were made using an HP 4284A LCR meter on this poly-Si MOS structure and on the sample without poly-Si where an electrolyte was used to make the top contact. The electrolyte was a solution of 1.0 M tetrabutylammonium hexafluorophosphate in propylene carbonate and the electrolyte area was about 350 μm by 350 μm.

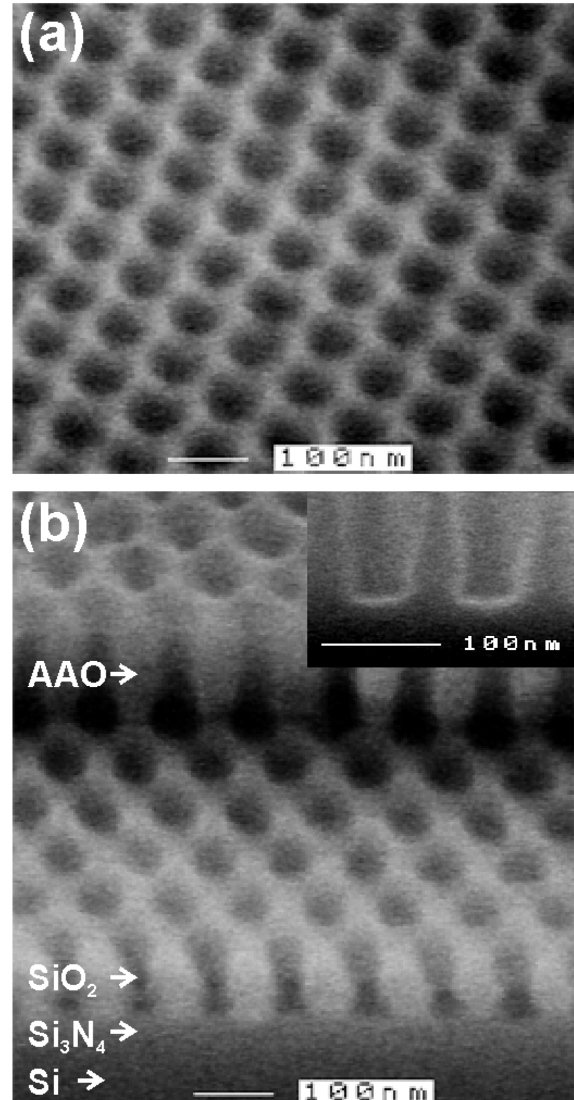

Figure 7.2. (a) Plan view SEM micrograph of nano-hole array in SiO_2/Si_3N_4/on Si (b) Oblique angle SEM micrograph showing the different material layers (after wet etch). Inset in upper right hand corner shows a cross-sectional image.

7.4. RESULTS AND DISCUSSION

Figure 7.2 shows SEM images of the ordered array of nano-holes on silicon oxide/nitride transferred by the AAO mask before the growth of the gate oxide.

Figure 7.2 (a) shows a plan-view micrograph of the hexagonal array of nano-holes in the SiO_2 layer with an average diameter and spacing of 50 nm and 100 nm, respectively. Note the high degree of size uniformity and ordering. Typically, such ordering can be achieved over 1 to 2 μm sized domains. It should be noted that comparable ordering over millimeters can be achieved using AAO films fabricated using a combination embossing/AAO technique [57, 58, 63]. Figure 7.2 (b) shows an oblique angle SEM micrograph with labels indicating the different layers present. In this case, part of the AAO film was intentionally left on the etched surface. Note these holes have straight side walls and flat bottoms at the silicon surface. Also the diameter of the nano-holes is consistent with the diameter of the AAO pores. The inset in Figure 7.2 (b) shows an expanded cross-sectional view of the bottom of two holes. It was found that the silicon

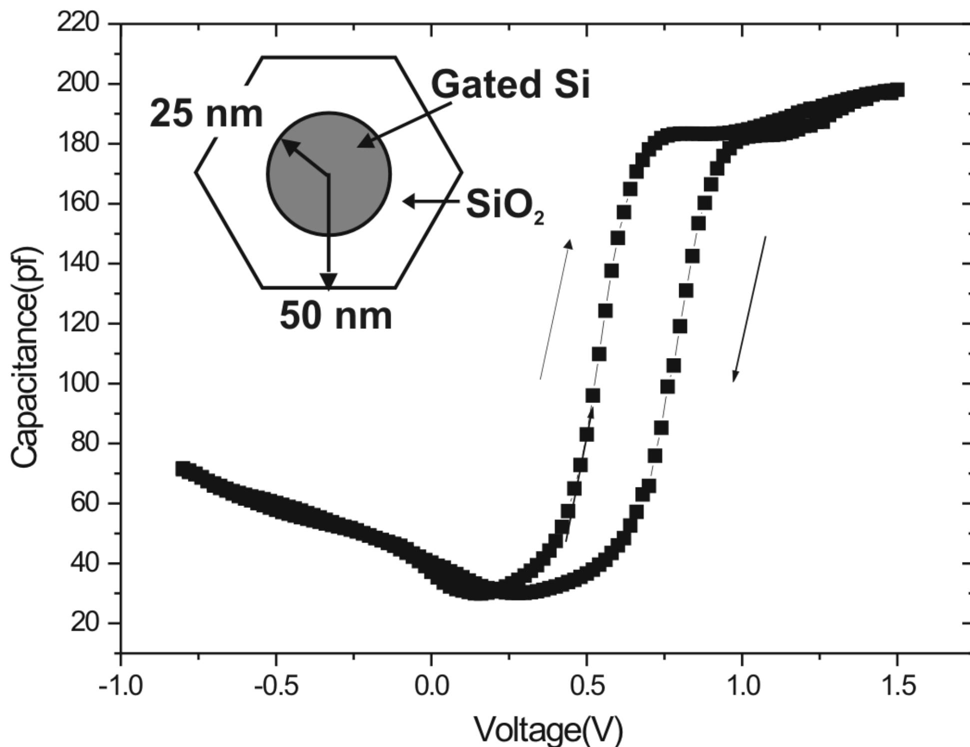

Figure 7.3. Room temperature Capacitance-Voltage curves taken at 100 kHz using the electrolyte contacting technique. Inset is a schematic of our nano-hole structure unit cell with dimensions.

nitride protective layer/selective wet etching step is necessary to achieve this geometry at the silicon surface. Similarly processed samples without the nitride layer resulted in rounded profiles as observed by others [62].

Room temperature capacitance-voltage measurements were made on both the poly-Si gate electrode configuration, and the electrolyte-contacted configuration. Both *C-V* measurements showed little leakage. Figure 7.3 shows *C-V* curves taken at 100 kHz for the electrolyte configuration. The hysteresis in the *C-V* curves is typical for electrolyte-contacted MOS structures as a result of their frequency response to the driving voltage [82]. However, the presence of interfacial states could also be partly responsible for causing the offset. The inset in Figure 7.3 shows the hexagonal unit cell of the structure based on the SEM micrographs. Based on this unit cell structure, the area fraction of gated Si area to unit cell area is 0.23. For an electrolyte area of 350 μm by 350 μm, an oxide capacitance of 850 pF is expected. Based on Figure 7.3, the related capacitance for our nano-array is 190 pF. The ratio of the nano-array to uniform capacitance is 0.22. This agrees well with the area fraction 0.23, above, indicating that the gated-Si area in the nano-array is the major contribution to the capacitance.

7.5. CONCLUSION

In conclusion, a highly ordered array of nano-holes has been formed in silicon oxide/silicon nitride on silicon using RIE and wet etching to transfer a pattern through an AAO mask. The presence of a thin silicon nitride layer between the oxide and the silicon served as a buffer layer allowing improved pattern transfer with uniform profiles and flat trench bottoms. This technique allowed good pattern transfer over a large area (~3mm by

3mm) which in principle could be scaled up to even larger dimensions. In addition, MOS-type device structures formed by growing a thermal oxide on the exposed silicon and using either a poly-Si gate or an electrolyte contact were fabricated. Room temperature *C-V* measurements on these structures showed little leakage. Moreover, capacitance values for the electrolyte contact indicated that only the exposed silicon area contributed to this capacitance. To my knowledge, this is the first reported electrical measurement made on nanostructured silicon devices fabricated using AAO films. Possible future work should involve the fabrication of similar structures to explore single electron effects via low temperature *C-V* measurements and scattering effects from textured channels via low temperature transport measurements.

Chapter 8

Fabrication and Characterization of Nano-Ring Arrays

8.1. ABSTRACT

Ordered arrays of Au, Ni, and Si nano-rings have been fabricated using Ar^+ sputter re-deposition of material in a porous alumina mask. Typical ring dimensions are 50 nm inner diameter, 10-15 nm wall thickness with heights ranging from 50-200 nm. Ring composition was confirmed by electron microscopy. Ring diameter, height and spacing are controllable by varying the process conditions. This process is scalable and parallel, so that highly ordered nano-rings over millimeter-sized regions are possible. Finally, much of this chapter was published with minor changes [83]:

K. L. Hobbs, P. R. Larson, G. D. Lian, J. C. Keay, and M. B. Johnson, "Fabrication of Nanoring Arrays by Sputter Redeposition using Porous Alumina Templates", *NanoLett.* **4**, 167 (2004).

8.2 INTRODUCTION

Currently there is a great deal of interest in nanometer-sized rings (nano-rings) from theoretical, experimental and device perspectives. Of interest are such properties as: persistent currents in metallic [84] or superconducting rings [85], tunable optical resonance in metal rings [86], novel magneto-optical behavior in semiconductor rings [87], magnetic response for application in patterned perpendicular recording media [88, 89] and novel ring-shaped MRAM [90]. In addition, collective properties of ordered arrays, involving coupling between adjacent rings, may exhibit new physical behavior. Such collective properties have also received attention. In particular, collective excitations in lattices have been theoretically investigated [91, 92].

In the past nano-rings have been fabricated using various methods including electron beam techniques [84, 93] and nano-sphere lithography [94]. The methods described here, involving AAO templates, have advantages over these othere techniques. In particular, these AAO template techniques are scalable and parallel providing a method to fabricate large, ordered nano-ring arrays. Moreover, these methods allow control over the nano-ring height independent of the ring diameter to produce high aspect ratio rings.

In this chapter, the fabrication and characterization of ordered arrays of Au, Ni and Si nano-rings fabricated using Ar^+ sputtering and porous AAO templates are described. Two methods are presented, both relying on the re-deposition of sputtered material inside the pores of an AAO mask. Typical nano-ring dimensions are 50 nm inner diameter with 10 to 15 nm wall thickness and heights ranging from 50 to 400 nm. Ring composition and phase was confirmed by energy dispersive (x-ray) spectroscopy

(EDS) and selected area electron diffraction (SAED). Ring diameter, height, and spacing are controllable by varying the process conditions. In addition, magnetization hysteresis curves were taken on both a Ni nano-ring array and compared with a Ni nano-dot array and a bulk thin film Ni layer.

8.3. EXPERIMENTAL DETAILS

Figure 8.1 schematically shows the two methods used to fabricate nano-rings. In Method I, Figures 8.1 (a)-(c), a through-hole AAO template is used as a sputter mask on 20 nm of SiO_2 on a thick layer of the desired ring material. In Figure 8.1 (a) the AAO template is lifted off onto the sample. Figure 8.1 (b) shows the results of ion etching through the AAO pores leading to the re-deposition of ring material around the pore walls. Finally, the AAO template is removed (Figure 8.1 (c)) leaving behind the sputter re-deposited rings on the SiO_2 layer. In Method II, Figures 8.1 (d)-(f), the

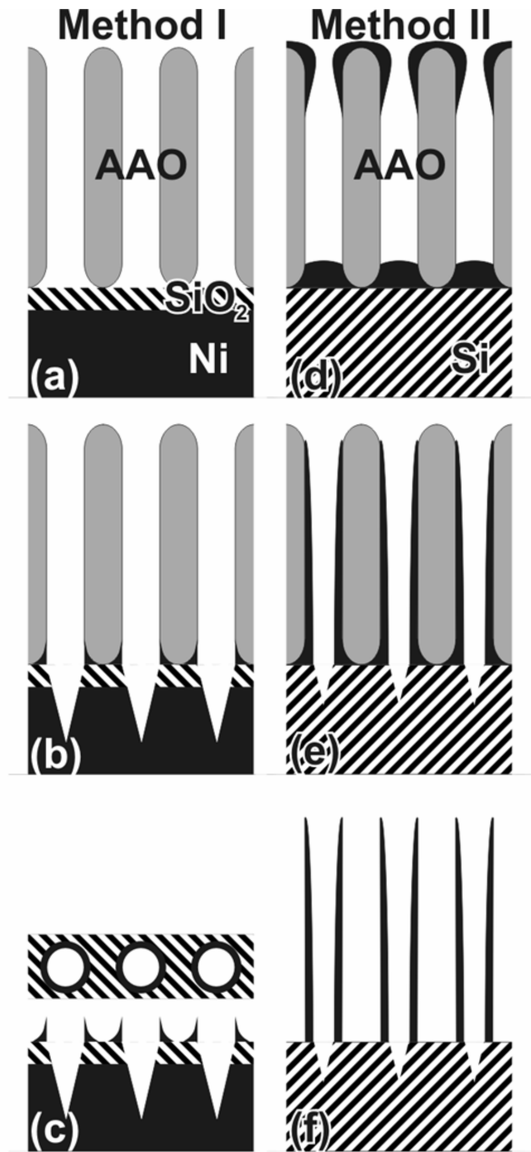

Figure 8.1. Schematic views of Method I and Method II. For Method I: (a) shows the AAO template on 20 nm of SiO_2 on the desired ring material, (b) shows sputter re-deposited material around the pore walls after sputter etching, (c) shows the rings after AAO mask is removed (with a plan-view added to guide the eye). For Method II: (d) shows AAO mask on a silicon substrate after ring material is evaporated down the mask, (e) shows sputter re-deposited material around the pore walls after sputter etching, (f) shows the rings after AAO mask is removed.

through-hole AAO template is used as an evaporation shadow mask to define an array of dots as shown in Figure 8.1 (d). This is followed by an ion-etching step that leaves behind sputter re-deposited dot material around the pore walls as shown in Figure 8.1 (e). After removal of the AAO template an array of nano-rings or tubes remain as shown in Figure 8.1 (f). In the paragraphs below, the growth and transfer of the alumina template, and the subsequent evaporation, sputtering, and processing steps are discussed in greater detail.

The AAO templates are fabricated using a two-step anodization process described in detail in previous chapters and elsewhere [49, 51, 52]. This two-step process starts with anodizing an aluminum foil for a long time (15 hr) to grow a thick porous layer. This is then chemically stripped off and followed by a second anodization step for a short time (5 min). Using this two-step technique, very good ordering over micron sized areas is obtained. More recently, a nano-imprinting technique designed to seed pore formation has achieved ordering over millimeter sized areas [57, 58]. In the work reported here, the anodization was performed either in 0.3 M oxalic acid at 40 V (producing 50 nm diameter pores spaced 100 nm apart) or 0.3 M sulfuric acid at 27 V (producing 20 nm diameter pores spaced 60 nm apart). All anodizations were carried out at 1 ^{o}C. After the second anodization, a through-hole mask about 300 nm thick was prepared by separating the AAO film from the Al foil in a saturated $HgCl_2$ solution and removing the remaining bottom alumina barrier layer in a solution of H_3PO_4 (5 wt %) at 30 ^{o}C for 35 minutes. The resulting mask was then placed on the substrate. Typical mask dimensions were 3 mm x 3 mm.

To evaporate appreciable material down the AAO template, it is crucial that the divergence of the evaporated material is lower than about 10° to accommodate the 6:1 aspect ratio of the alumina mask. All evaporations were carried out using an Edwards E306A thermal evaporator with a source-to-sample distance of 10 cm and a typical source size of 5 mm x 5 mm. Under these conditions evaporating a 60 nm thick layer on the top surface of the AAO yields 40 nm high nano-dots and coats the top portion of the side-walls of the AAO template as shown schematically in Figure 8.1 (d). This coated top portion is important as it contributes to the final nano-ring structure, specifically the height, because the sputter step is highly directional and does not remove much of this material.

As with the evaporation it is important to sputter with a low divergence ion beam. In this work, a VG Microtech EX05 ion source with a source to sample distance of 50 mm and an angular divergence of about 0.1^o was used. The samples were etched with Ar^+ beam at an energy of 500 eV and current density of 0.15 mA/cm^2. The low incoming energy of the Ar^+ results in an under-cosine (flatter) distribution of emitted sputtered particles [95]. This flat distribution is better for the sputter re-deposition leading to rings or tubes. The sputter time (typically 3 min.) was chosen to remove the entire bulk evaporated film from the alumina template surface.

After etching, the AAO templates were removed from the samples using an appropriate wet etch. In this work an equal parts chromic/phosphoric acid (1.8%/6% by weight) solution was used at 60 ^oC. Although removing the template is useful for characterization, it is not necessary, and rings left in the template have greater mechanical stability.

Samples were characterized with a JEOL 880 SEM; a JEOL 2000 FX TEM and a JEOL 1010F TEM. Secondary electron imaging (SEI), scanning transmission electron microscopy (STEM) dark field imaging, selected area electron diffraction (SAED), and electron dispersive spectroscopy (EDS) were performed with these instruments in addition to standard SEM and TEM imaging. Samples prepared for SEM analysis were fabricated on Si substrates with the AAO mask removed after the sputtering step. TEM samples were fabricated either on Si or directly on ultra-thin carbon film TEM grids [96]. TEM samples on Si were mechanically polished and then thinned with an Ar ion mill. Samples fabricated on TEM grids required no further processing and were examined with the AAO template intact.

Finally, magnetization hysteresis loops were taken at room temperature on a Ni nano-ring array on Si fabricated using Method II, a nano-dot array on Si, and a bulk thin film of Ni on Si using a superconducting quantum interference (SQUID) magnetometer (Quantum Designs MPMS XL) at the University of Nebraska.

8.4. RESULTS AND DISCUSSION

8.4.1 Electron Microscopy Results

Figure 8.2 shows Si rings on a SiO_2/Si substrate fabricated using Method I. Figure 8.2 (a) is a top-down SEM image showing well-ordered 50 nm inner diameter (ID), 10 nm thick rings with 100 nm center to center spacing. Size variations of these dimensions were about 20 % (typical for Method I). The inset shows a 45° view from which the ring height (Si plus SiO_2) was determined to be 50 nm. Figure 8.2 (b) is a TEM image of a thinned sample with a SAED pattern (inset). The sharp diffraction

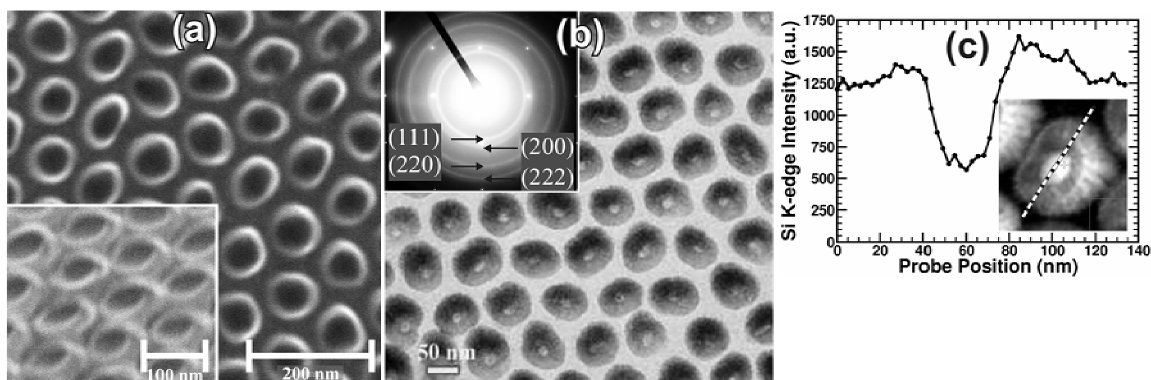

Figure 8.2. Electron microscopy results for Si nano-rings fabricated using Method I. (a) top down SEM micrograph of rings on a SiO_2/Si substrate. Inset is a 45° oblique view showing the 50 nm tall rings (same mag.). (b) TEM image of the Si rings and SAED pattern (inset). (c) EDS profile of Si K-edge across the dotted line shown on the STEM annular dark field image of a single Si ring (inset).

peaks are from the crystalline substrate (Si (100)), while diffuse rings indicate that the nano-rings are amorphous Si. The difference in SEM and TEM contrast is primarily the result of reduced secondary electron yield from the etched hole leading to the dark region in the SEM image. Finally, Figure 8.2 (c) is a plot of a Si K-edge EDS line scan across a single nano-ring, shown on the STEM annular dark field image (inset). This line scan clearly indicates reduced Si in the center of the ring as expected because the hole extends into the Si substrate (as seen directly in cross-sectional views). The line scan also shows reduced Si at either end outside the ring, although to a lesser extent than in the center. Ni rings were also produced by this method. Figure 8.3 shows Ni rings on a 20 nm thick SiO_2 layer on Ni on Si substrate (inset shows a

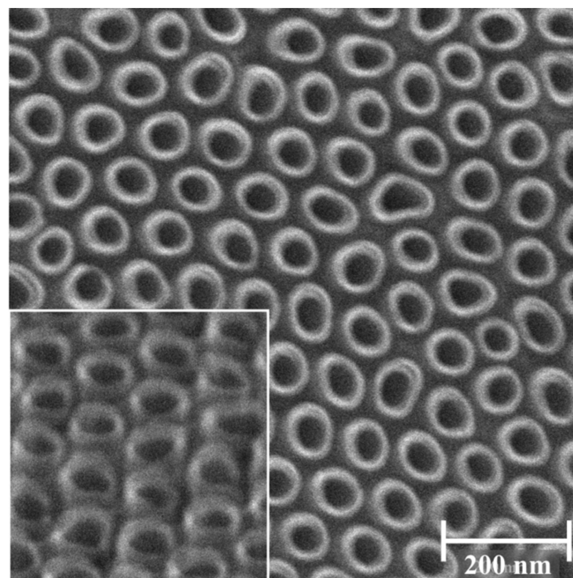

Figure 8.3. Top down SEM micrograph of Ni rings on SiO_2/Si substrate fabricated using Method I. Inset is a 45° oblique view showing the 50 nm tall rings (same mag.).

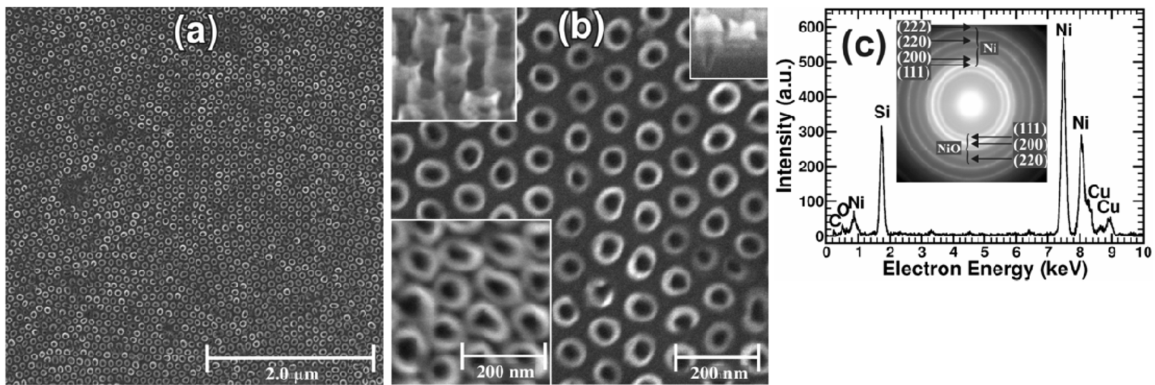

Figure 8.4. Electron microscopy results for Ni rings fabricated using Method II. (a) SEM image of a typical region. (b) SEM image of a well-ordered 1 μm x 1 μm region showing rings with inner diameters roughly 50 nm with wall thickness around 15 nm. All insets are the same scale. Top right: a cross-sectional view showing the sputtered hole in the Si substrate. Top left: a 55° oblique view showing the 200 nm tall rings. Bottom left: top down view of Ni rings fabricated in sulfuric anodized alumina, period is halved. (c) EDS spectrum of Ni rings on a Si substrate. Indexed SAED pattern (inset) and spectrum confirms the rings are Ni and NiO (Cu peak is due to the TEM grid).

45° view). These rings have similar dimensions to the Si rings described above.

Nickel rings have also been fabricated on Si using Method II. The electron microscopy results are summarized in Figure 8.4. Figure 8.4 (a) is a large-scale view showing the typical micron-sized, well-ordered domains. Figure 8.4 (b) is a close-up view showing a region of 50 nm ID, 10 nm thick rings separated by 100 nm. Size variations for these dimensions were about 10% (typical for Method II). Top-right inset is a cross-sectional image of a related sample showing that the sputter-etched holes continue into the Si substrate. The top left inset shows a 55° oblique angle SEM view from which a nano-ring height of 200 nm was determined. The bottom left inset shows nano-rings fabricated with a sulfuric acid-grown AAO template. In this case, the rings have an inner diameter of about 35 nm, an outer diameter of 60 nm and a center-to-center spacing of about 60 nm. Figure 8.4 (c) shows an EDS spectrum from a thinned sample prepared for STEM. The SAED pattern (shown inset) indicates the presence of Ni and NiO. Both results confirm the rings are Ni, (the small Cu signal is from the TEM grid).

Similar results have been obtained with Au rings on a Si substrate and on an ultra-thin carbon TEM grid using Method II. The electron microscopy results are shown in Figure 8.5. Figure 8.5 (a) is a close-up view showing a well-ordered region of 50 nm ID, 10 nm thick rings separated by 100 nm. Bottom-right inset shows a 45° view from which the nano-ring height was determined to be approximately 150 nm. Figure 8.5 (b) shows details from TEM analysis of the rings still in the alumina template. The TEM image is shown inset (top center) and a SAED pattern (top-right inset). The EDS spectrum shows the presence of gold (again the Cu signal is from the TEM grid). The electron diffraction image (top-right inset) indicates that the rings are polycrystalline gold.

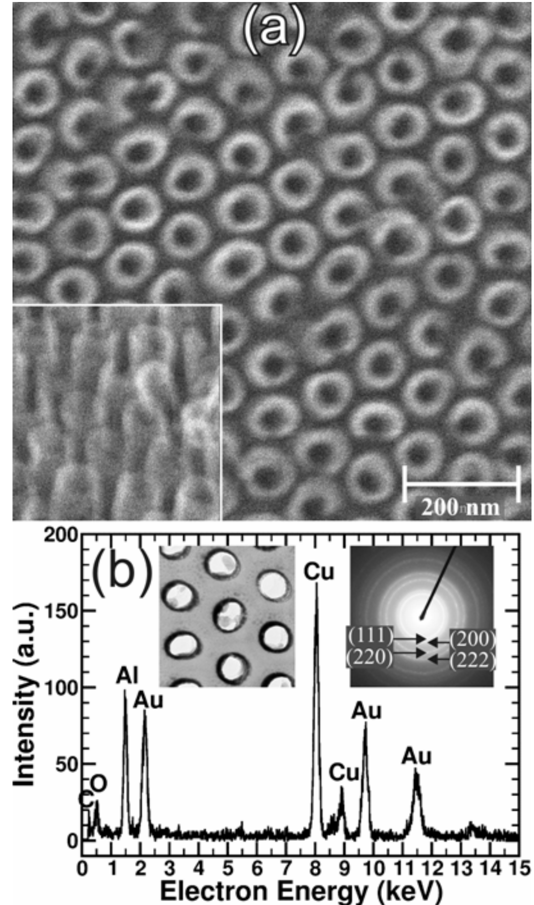

Figure 8.5. Electron microscopy results for Au rings fabricated using Method II. (a) top down SEM micrograph of Au rings on a Si substrate with 45° oblique view (inset) showing 150 nm tall rings. (b) EDS spectrum of Au rings still inside the AAO template. The spectrum and indexed SAED pattern (inset) confirm the rings are poly-crystalline gold.

Au nano-ring arrays have also been fabricated directly in AAO templates grown on Al foils using a modified version of Method II. In this case, a Au layer was evaporated directly on an approximately 300 nm thick AAO film still on the Al growth substrate. This was followed by an ion-etching step that left behind sputter re-deposited dot material around the AAO pore walls. Figure 8.6 shows an SEM image of the Au

rings fabricated directly in an AAO template on an Al foil. The Au rings are visible around the AAO pore walls and have similar lateral dimensions to the Au rings fabricated using Method II above (50 nm ID, 10 nm thick rings separated by 100 nm). The height of the nano-rings could not be determined from the SEM images but it is thought that they extend throughout the length of the AAO template which was around 300 nm. An advantage of fabricating rings directly into AAO templates (and not removing the AAO) is the mechanical stability provided by the AAO itself.

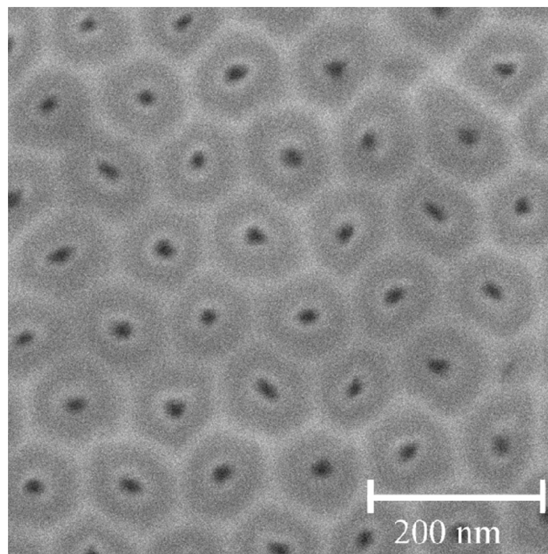

Figure 8.6. SEM micrograph of Au nano-ring array fabricated in an AAO film on an Al foil.

As described above well-ordered arrays of rings have been fabricated with some variation in ring geometry. The prospects for further controlling the ring and array geometry based on our results with Methods I and II are discussed in the paragraphs below. For both methods, the center-to-center nearest neighbor spacing of the rings is the same as the inter-pore spacing of the AAO template. As discussed in Chapter 3, this is controlled by the anodization growth conditions. The anodization voltage primarily controls the inter-pore spacing with the electrolyte concentration playing a significant role in the pore diameter and pore ordering. Inter-pore spacing of about 60 nm (sulfuric), 100 nm (oxalic), and 500 nm (phosphoric) are typically used to obtain well ordered pore arrays. However, using the proposed "10 % porosity rule" [56], inter-pore spacing between these values can be obtained while still maintaining a significant degree of

ordering. Again, it is worth noting that long range order extending over millimeters can be obtained using nano-indenting techniques to initiate pore formation [57, 58].

It can be seen that the rings produced by Method I are shorter than those produced by Method II. In Method I, the ring height is governed primarily by the incident ion energy. For the 500 eV Ar^+ incident energy used in this work, the resulting etched-material sputter distribution is an under-cosine profile resulting in short rings. Higher ion energy with a closer to cosine sputter distribution should result in taller rings. One disadvantage of Method I is that the rings are above a bulk layer of the same material. However, the SiO_2 separation layer can, in principal, be selectively removed to allow the rings to be transferred to another substrate. With Method II, nano-ring height is a combination of effects including the AAO template thickness, details of the evaporation, and the incident ion energy. As shown schematically in Figure 8.1, the final ring is a combination of material re-deposited from the dot and that coating the top-portion of the AAO pore. This has been confirmed by comparing dot (prior to sputtering) and ring (after sputtering) volumes. The final ring height is slightly smaller than the thickness of the template. Thus reducing or increasing the template thickness allows control over reducing or increasing the ring height. In this regime, it is expected that the height of the shortest rings will be close to the thickness of the thinnest AAO that can be used, around 100 nm for this work. On the other hand, much taller rings should result from using thicker templates, increasing the amount of evaporated material, and decreasing the evaporated materials' angular divergence. Under these circumstances, it should be possible to fabricate rings with aspect ratios even higher than the 4:1 ratio demonstrated here. For sufficiently thick templates it should be possible to have the rings formed only

from the sputtered dot material, with the top portion material not contributing. Under these circumstances, it should be possible to fabricate rings with heights less than 50 nm using Method II.

It is interesting to note that the outer diameters of freestanding rings often exceed the inner-diameter of the as grown AAO pore. For example in Figure 8.5 (a) the outer diameter is about 70 nm, while in the TEM image (inset of Figure 8.5(b)) the rings in the AAO matrix have an outer diameter of about 50 nm. A more dramatic example is shown in the SEM image of Ni rings fabricated using a sulfuric acid anodized template (lower-left inset Figure 8.4 (b)). For a sulfuric acid-grown AAO film, the pores are 20 nm in diameter with inter-pore spacing of 60 nm. The Ni rings have inner diameters of about 35 nm and outer diameters near 60 nm, while still maintaining the expected 60 nm period such that the rings are nearly touching. This discrepancy is attributed to the widening of the pores during the barrier-layer opening wet etch step. Thus there is some control over the outer diameter of the rings independent of the spacing. This is important for tailoring the coupling between neighboring rings. Currently, ways to improve the control of the barrier-layer removal step are being investigated. Recent developments of a dry-etching step to more controllably remove the barrier layer may improve this process [97].

8.4.2 Magnetization Hysteresis Loops of Ni Nano-Ring and Nano-Dot Arrays

Magnetization hysteresis loops were measured for a Ni nano-ring array on Si (fabricated using Method II), a Ni nano-dot array on Si, and a bulk Ni thin film on Si at room temperature by a superconducting quantum interference device (SQUID) magnetometer. Figure 8.7 (a) and (b) shows SEM micrographs of the Ni nano-ring and nano-dot arrays, respectively. As can be seen in Figure 8.7 (a) the nano-rings in this case

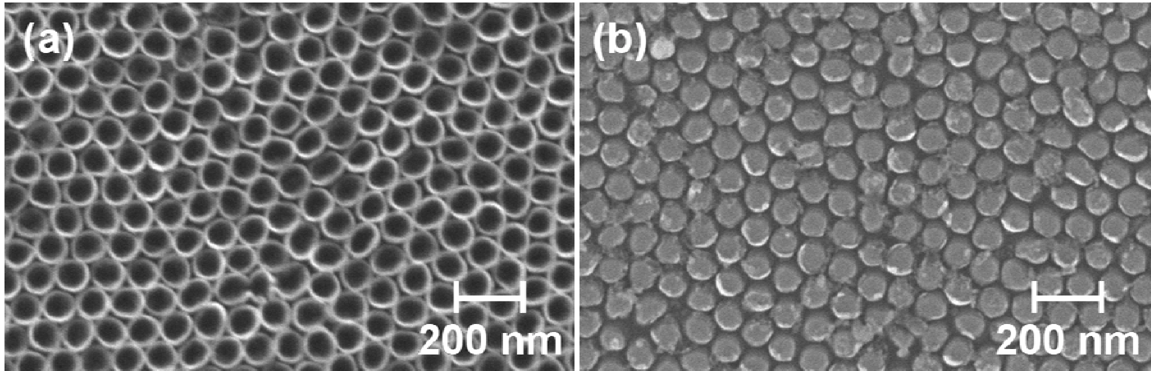

Figure 8.7 SEM micrographs of (a) Ni nano-ring sample that magnetization hysteresis loops were obtained on. (b) Ni nano-dot sample that magnetization hysteresis loops were obtained on.

are nearly touching with dimensions of ~ 80 nm ID, 10 nm ring thicknesses and spacings of 100 nm. Oblique angle SEM micrographs (not shown) were used to determine the ring height for this array to be 400 nm. This was not unexpected since in this case, a thicker (~ 500nm) AAO template was used in the fabrication process. From Figure 8.7 (b), the nano-dots have dimensions of approximately 70 nm diameters spaced 100 nm apart. The height of the dots was estimated from crystal monitor data taken during the thermal evaporation of the dots to be about 25 nm. Finally, the thickness of the bulk thin film of Ni on Si was estimated to be about 50 nm from crystal monitor measurements during the evaporation.

Figures 8.8 (a) and (b) show the hysteresis loops for the Ni nano-ring array with the external field applied parallel and perpendicular to the plane of the sample, respectively. These can be compared directly with the hysteresis loops for the Ni nano-dot array with the external field applied parallel and perpendicular to the plane of the sample (Figures 8.8 (c) and (d), respectively) as well as the hysteresis loops for the bulk Ni film with parallel and perpendicular applied external fields (Figures 8.8 (e) and (d), respectively). Table 8.1 summarizes the coercivities, remanences, and saturation fields for the curves.

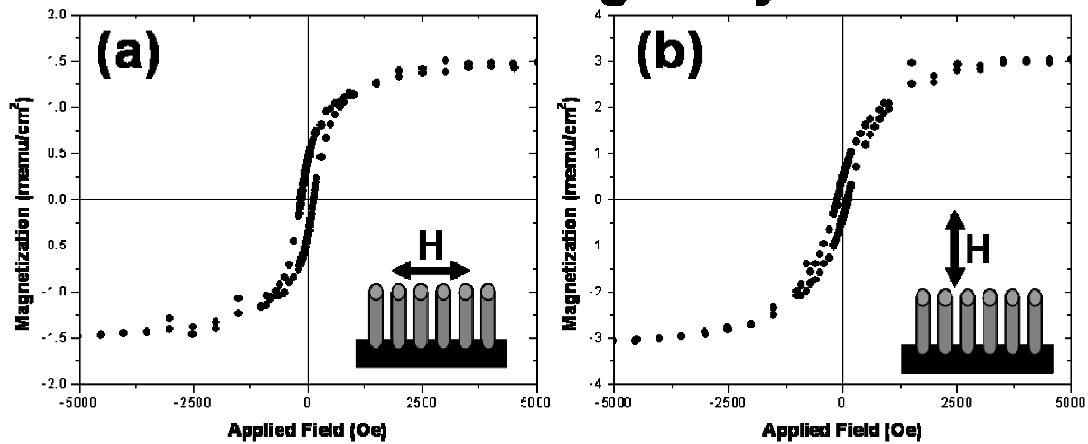

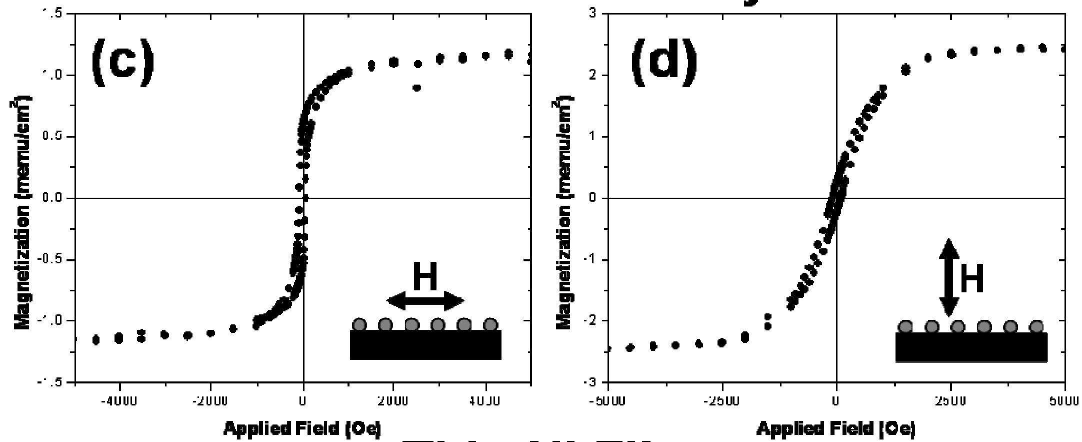

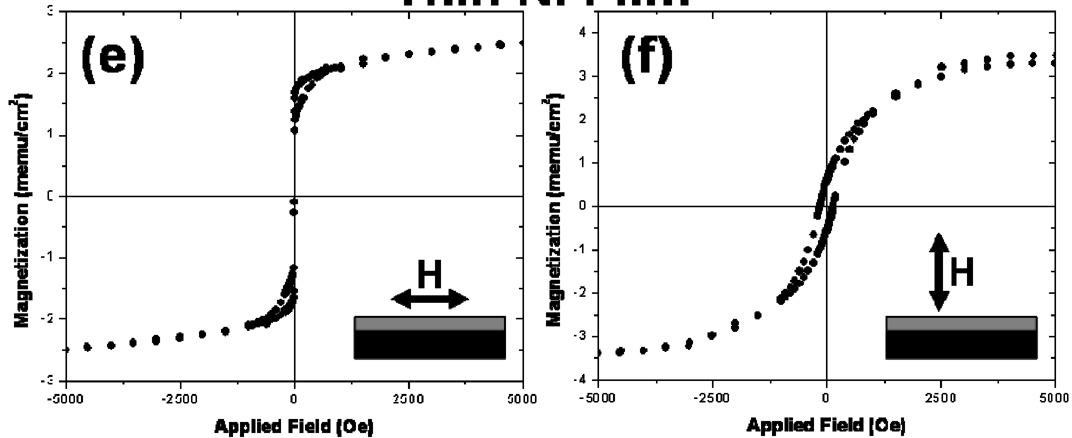

Figure 8.8 Magnetization hysteresis loops for (a) Ni nano-ring array with external field parallel to the plane of the sample. (b) Ni nano-ring array with external field perpendicular to the plane of the sample. (c) Ni nano-dot array with external field parallel to the plane of the sample. (d) Ni nano-dot array with external field perpendicular to the plane of the sample. (e) Thin Ni film with external field parallel to the plane of the sample. (b) Thin Ni film with external field perpendicular to the plane of the sample.

The nano-ring hysteresis curves for both parallel and perpendicular external field directions exhibit similar values for the coercivities, remanences, and saturation fields. In this case, the nano-ring array does not have a preferential magnetic orientation and shows no improvement over the Ni nano-dot array or Ni thin film. This is in contrast to work on high aspect ratio Ni nano-wire arrays electrodeposited into AAO on Al [98]. In this work, the electrodeposited Ni nano-wires were 1 μm long, spaced 100 nm apart with diameters that could be varied between 30 and 55 nm. In addition, TEM measurements indicated the electrodeposited Ni wires were polycrystalline with nano-crystallites between 20-100 nm. For the 55 nm diameter nano-wire array, there was no preferential magnetic orientation. However, improvements were seen as the nano-wire diameters were reduced culminating with a 30 nm diameter nano-wire array, which demonstrated a clear preferential magnetic orientation along the wire axis, a large remanance, and a high coercivity of 1200 Oe.

	Coercitvity (Oe)		Remanence (memu/cm^2)		Saturation Field (Oe)	
	Par.	Perp.	Par.	Perp.	Par.	Perp.
Nano-ring Array	140	120	0.4	0.4	4800	4800
Nano-dot Array	60	90	0.6	0.2	4800	4800
Thin Ni Film	10	150	1	1	4800	4800

Table 8.1 Summary of magnetization properties for the Ni nano-ring array, Ni nano-dot array and thin Ni film.

For this work, the low coercive fields, remanences, and poor squareness or shape of the curves make this particular Ni nano-ring array unsuitable for patterned perpendicular magnetic media applications. These results are most likely due to two reasons: 1) the Ni nano-ring arrays are amorphous rather than crystalline and 2). The nano-rings are nearly touching allowing macroscopic interactions between the rings to dominate. Improvements to the Ni nano-ring array might be seen by annealing the nano-wires to induce crystallization although the Ni rings would need to be fabricated on substrates other than Si as the formation of nickel silicides are seen at relatively low temperatures (~ 250 ^{o}C for N_2Si) [99]. In addition, larger ring separations would also help to eliminate "cross-talk" or interactions between the rings. Finally, higher aspect ratio rings or cylinders providing more Ni while maintaining the same pattern density would also help to improve the magnetization response.

8.4. CONCLUSION

In summary, two methods for producing nano-ring arrays through the sputter re-deposition of Ni, Au and Si in porous alumina templates have been presented. The composition and phase of the rings was verified by SAED and EDS. Rings fabricated using oxalic acid AAO templates produced rings of 50 nm inner diameter, 10 nm wall thickness and 100 nm center to center spacing. Deviations from these dimensions are about 20 and 10 % for Method I and Method II, respectively. Ring diameter, height, and spacing are controllable by varying the process conditions. In particular with Method II a large variation in ring height can be achieved, and for both methods outside ring diameter can be increased until the rings touch. In addition, these methods are scalable and

parallel which are important considerations for the development of nano-scale arrays for applications. Finally, magnetization measurements were made on Ni nano-ring and nano-dot arrays, and a thin film of Ni. These results showed that the nano-ring array exhibited little improvement over the nano-dot array or the thin film of Ni. This is likely due to the fact that the nano-rings were both amorphous (rather than polycrystalline) and nearly touching allowing interactions between the nano-rings to dominate.

8.5 ACKNOWLEDGMENTS

The SEM and TEM analysis was conducted in the Samuel Roberts Noble electron microscopy Laboratory at University of Oklahoma. Some sample preparation and characterization was performed by Kevin Hobbs. The magnetization hysteresis loops were collected by Dr. Joel Keay, a post-doc at the University of Oklahoma, using the facilities at the University of Nebraska. Finally, the author thanks Dr. Jinguo Wang at Penn State University for STEM ADF and EDS analysis.

Appendix 1

Pattern Transfer with AAO Films: Nano-Pillar Arrays

A1.1 ABSTRACT

GaAs and Si nano-pillar arrays have been fabricated by using AAO masks to define an array of dots that was subsequently used as a mask for a dry etching process. Such pillars could have applications in data storage, opto-electronics (as light emitting arrays) or nano-tribological coatings to improve surface characteristics. Two methods of fabrication were investigated: (1) Fe dots were evaporated through an AAO mask onto a GaAs substrate. The AAO mask was removed and the array of Fe dots were used as masks in an Ar^+ etching process to create an array of GaAs pillars. (2) An AAO mask was placed on a thin Si_3N_4 layer on a Si substrate. Reactive ion etching (RIE) was used to etch holes through the Si_3N_4 layer into the Si substrate. The exposed Si was oxidized leaving behind an array of SiO_2 dots. After removal of the AAO and Si_3N_4 layer, the

SiO_2 dot array was used as a mask in another RIE process to create an array of Si pillars. This second method for creating Si nano-pillars arrays was done in collaboration with researchers at the University of North Carolina [81].

A1.2 EXPERIMENTAL DETAILS AND RESULTS

A1.2.1 GaAs Nano-Pillar Array

A 500 nm thick oxalic acid-grown AAO film with 50 nm pore diameters spaced 100 nm apart was lifted off onto a GaAs substrate following the procedure outlined in Chapter 4 and shown schematically in Figure 4.1. Next, 70 nm of Fe was thermally evaporated onto the AAO/GaAs substrate following the general procedures outlined in Chapter 4. After removal of the AAO mask by mechanical means (i.e. double-sided tape), a well-ordered array of 20 nm tall Fe dots remained. The sample was then exposed to an Ar^+ ion beam (VG Microtech EX05) for 17 minutes in a vacuum environment (10^{-10} Torr with the beam off, 10^{-6} Torr with the beam on) with a source to sample distance of

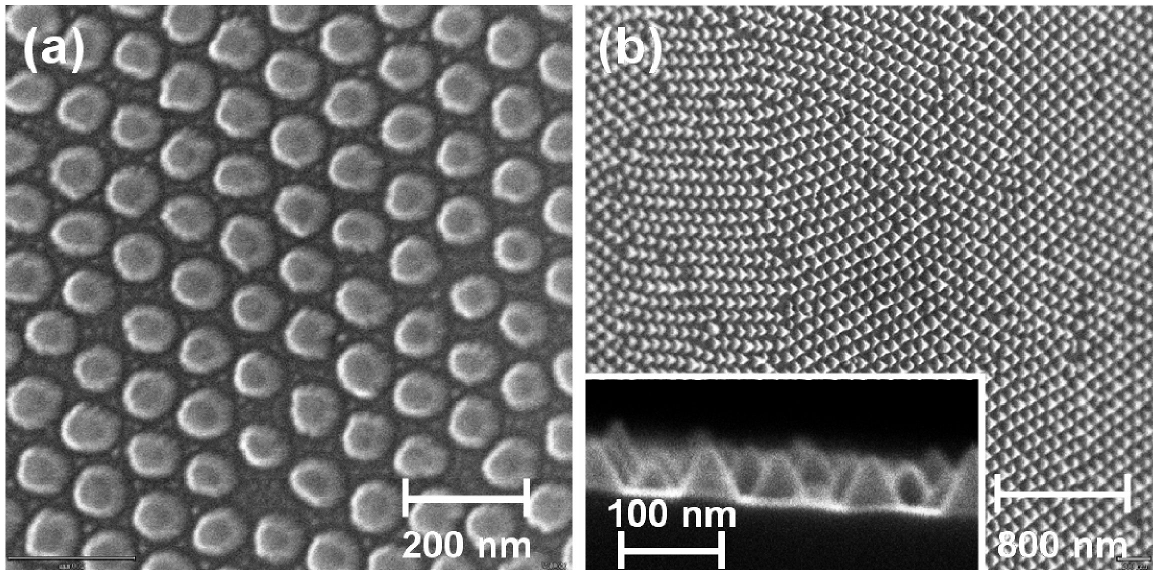

Figure A1.1 (a) Top down SEM micrograph of GaAs nano-pillar array. (b) 45° oblique angle SEM view of GaAs nano-pillar array. Inset shows cross-sectional SEM view.

50 mm and an angular divergence of about 0.1^o. The beam had an energy of 500 eV and a current density of 0.05 ma/cm^2. The etching time was chosen to etch away the 20 nm thick Fe dots, leaving behind GaAs pillars.

Figure A1.1 shows SEM micrographs of the resulting GaAs pillars. Figure A1.1 (a) shows a top down SEM micrograph of the GaAs nano-pillar array. From the SEM image, the nano-pillars are 80 nm in diameter, spaced 100 nm apart, in good agreement with the AAO pore spacing. Figure A1.1 (b) shows a 45° oblique angle SEM micrograph of the nano-pillar array. The inset in Figure A1.1 (b) shows a cross-sectional SEM view of the GaAs nano-pillar array. From the cross-sectional image the pillars are conical in shape and approximately 50 nm tall.

A1.2.2 Si Nano-Pillar Array

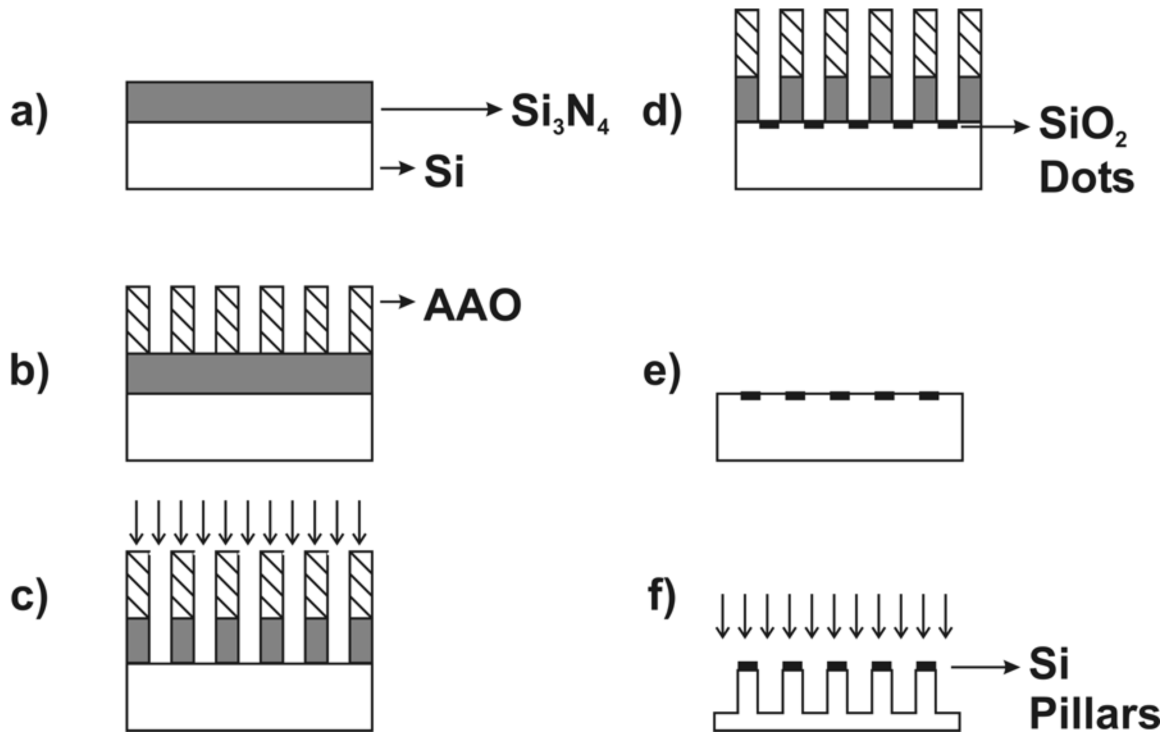

Figure A1.2 Cross-sectional schematic of processing steps: (a) Sample consisting of 20 nm Si_3N_4 on Si. (b) AAO mask lifted off onto the sample. (c) RIE etching through the Si_3N_4 and *into* the Si substrate. (d) 5 nm of SiO_2 thermally grown at base of holes. (e) Removal of AAO and Si_3N_4 layer. (f) Final RIE step to create Si pillars.

A 500 nm thick oxalic acid-grown AAO film with 50 nm pore diameters spaced 100 nm apart was lifted off onto a 20 nm thick layer of Si_3N_4 on a Si substrate shown schematically in Figure A1.2 (a) and (b). The AAO nano-hole array pattern was then transferred through the Si_3N_4 layer and into the underlying Si substrate using a Semigroup RIE 1000TP system. This is shown schematically in Figure A1.2 (c). After the RIE step, the exposed Si hole bottoms were thermally oxidized (Figure A1.2 (d)) at 800°C for 15 minutes, and the AAO and Si_3N_4 layers were etched away by a short (2 minutes, 40 seconds) 90 wt % H_3PO_4 wet etch at 180 °C. This left behind an array of roughly 5 nm tall, 50 nm diameter SiO_2 dots as shown schematically in Figure A1.2 (e). Finally, the SiO_2 dots served as a mask for a subsequent RIE etching step with a high selectivity for etching Si over SiO_2 using the Semigroup RIE 1000TP system to create an ordered array of Si pillars.

Figure A1.3 shows SEM micrographs of the resulting Si nano-pillar array. Figure A1.3 (a) shows an oblique angle SEM view of the resulting array. From the image, the pillars appear to be slightly less than 100 nm in diameter and almost touching. In

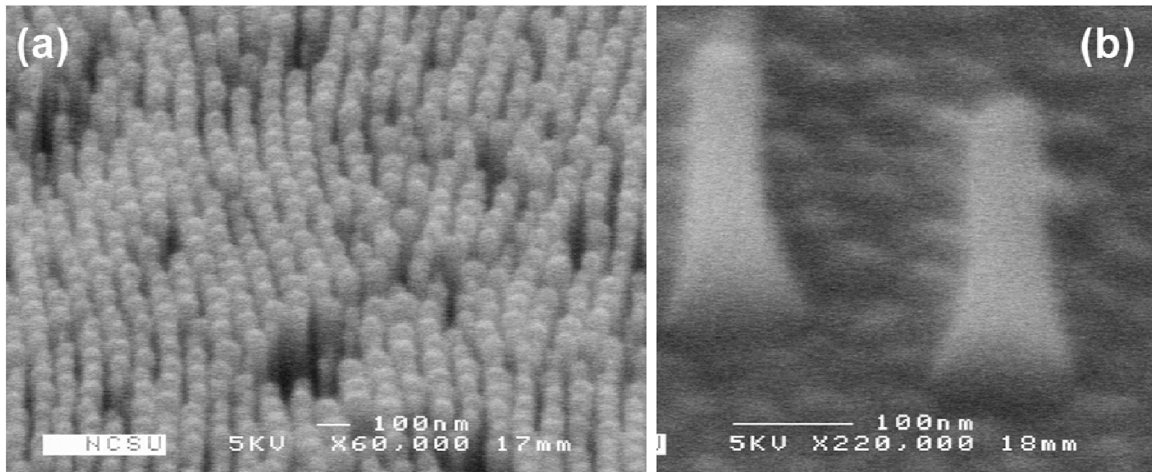

Figure A1.2..(a) Oblique angle SEM view of Si nano-pillar array. (b) Oblique angle SEM close-up view of two Si nano-pillars.

addition, there appears to be some non-uniformity in the height of the pillars as well as some regions of poor pattern transfer. Figure A1.3 (b) shows an oblique angle close-up SEM view of two pillars surrounded by a region of poor pattern transfer. From this image, the pillars are approximately 100 nm wide at the base, 50 nm tall at the top, and 280 nm tall.

A1.3 CONCLUSION

Arrays of nano-pillars were fabricated using two different methods. Both methods involved the use of AAO masks to define nano-dot arrays that were subsequently used as masks to define pillars in a dry etching step. The first method used thermally evaporated Fe dots on a GaAs substrate to fabricate GaAs pillars in an Ar^+ etching step. The second method involved an RIE and an oxidation step to create an array of SiO_2 dots in Si. This was followed by another RIE step using the SiO_2 dots as a mask to create an array of Si pillars.

Appendix 2

Carbon Nano-Tube Arrays

A2.1 ABSTRACT

A carbon nanotube array was fabricated upright on a SiO_2/Si substrate using an AAO template to seed an array of cobalt catalysts for a carbon nanotube growth step. Perpendicular arrays of high density, uniform nanotubes such as those presented here could have applications in data storage or field emission devices (*i.e.* displays or sensors). To start, an AAO template was used to transfer an array of nano-holes into the SiO_2 layer using an Ar^+ beam. Next, a cobalt nitrate solution was deposited into the nano-hole array and the AAO mask was removed. The cobalt nitrate was reduced, leaving behind an array of nano-sized cobalt catalysts in the SiO_2 nano-hole array. This was followed by a carbon nanotube growth step which resulted in an array of multi-walled carbon nanotubes perpendicular to the growth substrate. The nanotubes presented here were not as well ordered as multi-walled nanotubes grown directly in AAO templates [100, 101] but were

smaller in diameter. This work involved a collaboration with Dr. Melissa Reiger's group in the Department of Chemical Engineering at OU.

A2.2 EXPERIMENTAL DETAILS AND RESULTS

A 500 nm thick oxalic acid-grown AAO film with 50 nm pore diameters spaced 100 nm apart was lifted off onto a 900 nm thick SiO_2/Si substrate following the procedure outlined in Chapter 4 and shown schematically in Figure 4.1. The sample was then exposed to an Ar^+ ion beam (VG Microtech EX05) for 5 minutes in a vacuum environment (10^{-10} Torr with the beam off, 10^{-6} Torr with the beam on). The beam had an energy of 2 keV and a current density of 0.05 ma/cm^2. This step served to transfer a nano-hole array consisting of 50 nm diameter holes, approximately 5-10 nm deep with 100 nm spacings into the SiO_2 layer. The sample was then immersed in a 6 wt% cobalt nitrate solution and allowed to dry overnight before removing the AAO mask mechanically (i.e. double sided tape). Next, the cobalt nitrate in the nano-holes was reduced to cobalt by heating the sample to 500°C in an H_2 environment. Finally, the carbon nanotubes were grown by exposing the nano-particle cobalt catalysts in the nano-holes to a He:CO gas mixture (a flow rate of 50 sccm He: 50 sccm CO) at 700°C.

Figures A2.1 (a), (b), and (c), show top down SEM micrographs of the resulting carbon nanotube array. From these images, it appears that the nanotubes are not as well ordered as would be expected from the ordered nano-pores in the AAO mask. However, the density of the nanotubes calculated from the SEM images (~1.5×10^{10} cm^{-2}) is similar to the nano-hole array density (~ 10^{10} cm^{-2}). This would suggest that the cobalt nitrate was deposited into the nano-hole array initially and subsequently some of the cobalt

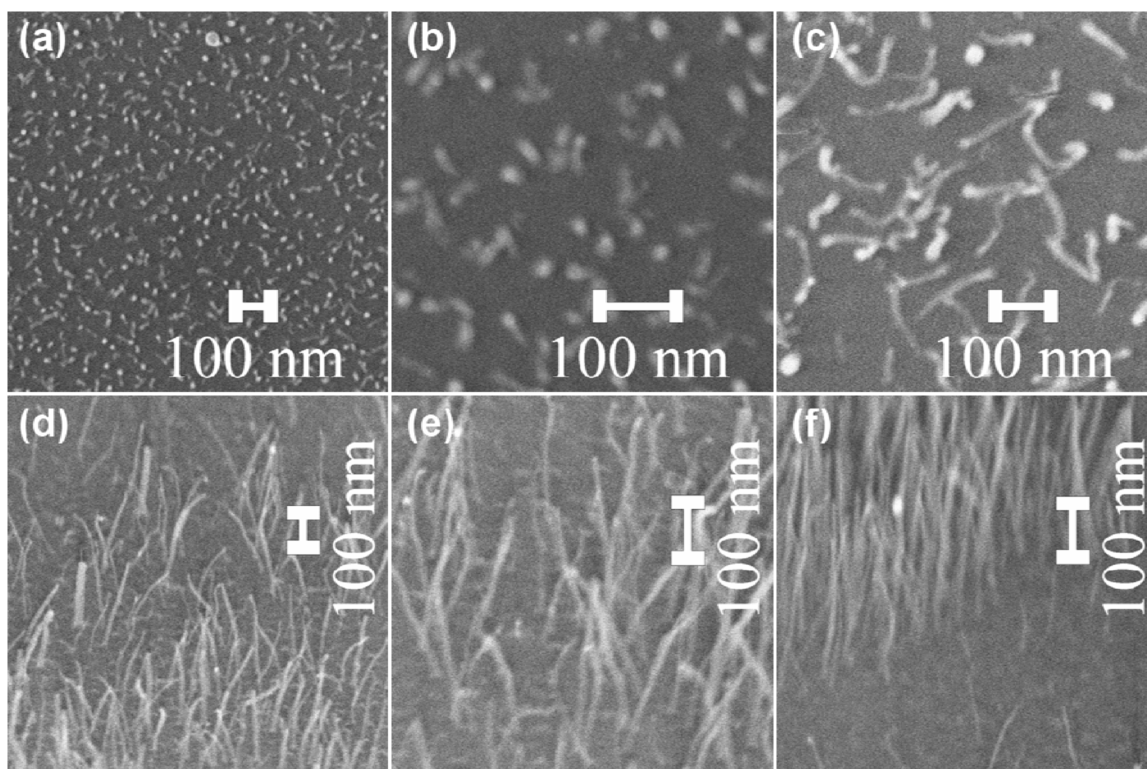

Figure A2.1. (a), (b), and (c) Top down SEM micrographs at different magnifications of a carbon nanotube array on an SiO_2/Si substrate grown using AAO pattern transfer methods and cobalt nano-particle catalysts. (e), (f), and (g) 60° oblique angle SEM micrographs of the carbon nanotube array. Note the presence of particles on the tops of some of the tubes. These are thought to be the Co nano-particle catalysts.

catalyst nano-particles migrated out of the nano-holes under the high temperature catalyst reduction or carbon nanotube growth step.

Figures A2.1 (c), (d), and (e) show 60° oblique angle SEM micrographs of the carbon nanotube array. From these images, the diameter and height of the nanotubes appear to be fairly uniform. The uniform diameter of the nanotubes is most likely a result of the uniform size of the catalyst nano-particles which was limited to the size of the nano-holes The diameter of the nanotubes is difficult to determine from the images but they are considerably smaller (~ 20 nm) than the 50 nm diameter hole array, while the height of the nanotubes is approximately 200 nm. In addition, it should be noted that there appears to be cobalt catalyst nano-particles visible on some of the tops of the

nanotubes, which is especially visible on Figures A2.1 (d) and (e). This type of growth mode, termed the "tip growth mode", where the metal catalyst resides at the tip of a growing nanotube, is a common mechanism for the growth of carbon nanotubes using metal catalysts deposited on substrates [102, 103]. This is distinct from the "base growth mode" where the catalyst particle resides at the base of the tube [104]. The type of growth mode of the nanotubes depends greatly on catalyst/substrate interactions, temperature gradients across the catalyst particles, and the nanotube growth technique.

A2.3 CONCLUSION

An array of carbon nano-tubes was grown perpendicular to the SiO_2/Si growth substrate by using AAO pattern transfer techniques with cobalt nano-particle catalysts. The AAO film was used to transfer a nano-hole array into the SiO_2 layer by Ar^+ etching. Next, a cobalt nitrate solution was deposited down the nano-hole array and the AAO was removed. Following the reduction of the cobalt nitrate solution, an array of cobalt nano-particle catalysts was left behind in the nano-hole array. Finally, a carbon nanotube growth step produced an array of carbon nanotubes standing upright on the substrate. The multi-walled nanotubes were smaller than the 50 nm diameter nano-holes and not as well ordered as the starting AAO film used to transfer the nano-hole array into the substrate. Due to the comparable nanotube and nano-hole density, it is believed that some of the cobalt nano-particle catalysts migrated out of the nano-holes under the high temperature catalyst reduction or nano-tube growth step, leading to an unordered array of carbon nano-tubes. In addition, from analysis of the SEM images, it appears that the

nanotubes were grown by the tip growth mechanism, where the catalyst nano-particles reside at the tips of the nanotubes.

Appendix 3

Fabrication and Characterization of Superconducting Nb Nano-Meshes

A3.1 ABSTRACT

Nb nano-meshes have been fabricated by a Nb sputter deposition directly onto AAO films. Preliminary characterization of these films using a scanning superconducting quantum interference device (SQUID) microscope shows the presence of vortices (whose position relative to the Nb mesh is limited by the SQUIDs ~ 8 μm spatial resolution) and indicates that the nano-meshes are superconducting. Future work will attempt to determine the location of these vortices when the magnetic field is commensurate with the diameter of the nano-holes.

A3.2 EXPERIMENTAL DETAILS

Nb was sputtered directly onto a 500 nm thick oxalic acid-grown AAO film on an Al foil with 50 nm diameter pores spaced 100 nm apart. The 2” diameter Nb target was positioned directly underneath the sample and the sample-to-source distance was approximately 12 cm. In addition, a 2 mm aperture was placed 2 cm away from the sample to limit the incoming divergence angle of the sputtered material and a 2 mm diameter shadow mask was placed directly on the AAO sample. Nb was DC sputtered using a Torus 2C Sputter Deposition Source in an Ar plasma at a pressure of 10^{-3} Torr,

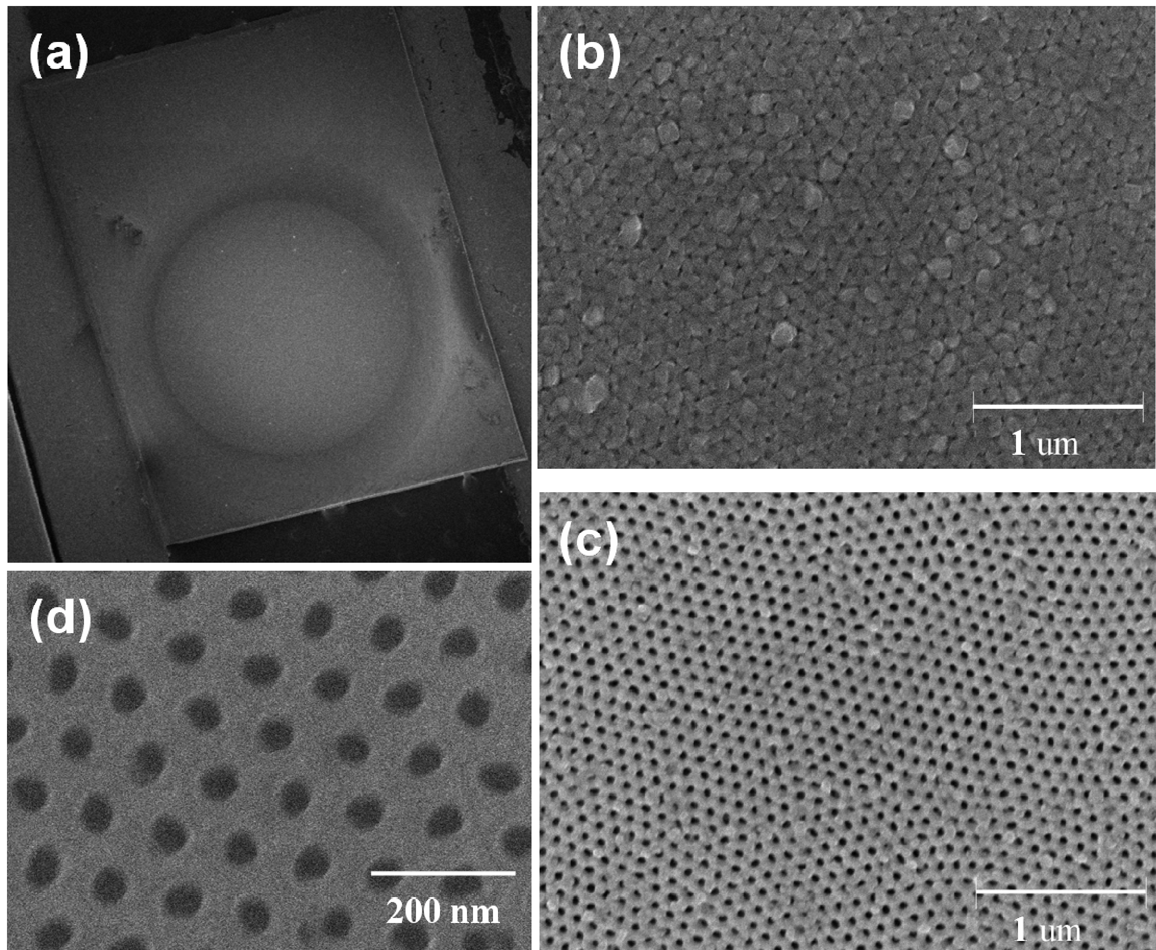

Figure A3.1 (a) Low magnification SEM image showing entire 2 mm diameter region of the Nb nano-mesh. (b) High magnification SEM image of the ~ 200 nm thick Nb nano-mesh taken in the center of the sample. (c) High magnification SEM of the ~ 75 nm thick Nb nano-mesh taken towards the edge of the sample. (d) High magnification SEM image of the AAO film prior to the Nb sputter deposition.

and a forward power of 200 W. Based on step height measurements taken on a control sample sputtered identically to the AAO sample, the thickness of the Nb was determined to be approximately 200 nm at the center of the sample and trailing off to around 75 nm towards the outer edge of the sample (around the edge of the 2mm diameter shadow mask). Figure A3.1 (a) shows a low magnification SEM image of the entire sample where the 2 mm diameter region of sputtered Nb can be clearly seen. Figure A3.1 (b) shows a high magnification SEM image taken from the center of the sample showing the roughly 200 nm thick Nb film almost covering up the AAO pores. Figure A3.1 (c) shows a high magnification SEM image taken toward the edge of the sample showing the roughly 75 nm thick Nb film with the AAO pores still clearly visible. Finally, Figure A3.1 (d) shows a high magnification SEM image of the AAO film prior to the Nb sputter deposition.

A3.3 RESULTS

The Nb nano-mesh sample was imaged using a scanning SQUID microscope built

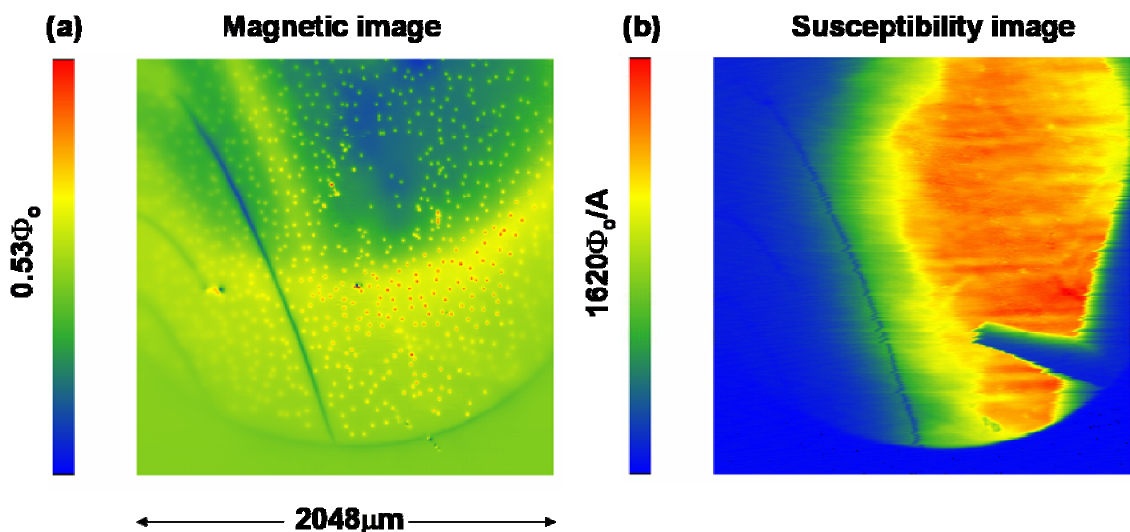

Figure A3.2 (a) Magnetic scanning SQUID microscope image of Nb nano-mesh sample. (b) Susceptibility scanning SQUID microscope image of Nb nano-mesh sample.

and operated by Dr. John Kirtley, a research staff member at IBM Research Division in Yorktown Heights, New York. The scanning SQUID microscope is used for measuring local magnetic fields with a magnetic field sensitivity of $<10^{-6}$ gauss $Hz^{-1/2}$ at a spatial resolution of ~ 8 μm [105]. Figure A3.2 (a) shows a standard magnetic scanning SQUID microscope image taken after the sample was cooled below the Nb superconducting transition temperature of 9.5 K in a field of about 3 mG. The dots present in the images are individual vortices, typically seen in Type II superconductors, confirming the superconducting nature of the sample. The vortices are resolution limited by the 8 μm square pickup loop and appear to have the standard quantum of magnetic flux. Figure A3.2 (b) shows a susceptibility image, a measure of the diamagnetic shielding, over the sample area. From this image, it was determined that the magnetic field penetration depth is consistent with a depth much less than 1 μm, as expected, and fairly uniform.

A3.4 CONCLUSION

Nb nano-meshes have been fabricated by sputter deposition onto AAO films. Preliminary characterization of these films using a scanning SQUID microscope with a spatial resolution of about 8 μm indicates that the nano-meshes are superconducting. Future work will involve characterization of these films by magnetization/susceptibility measurements as well as with a low temperature scanning magnetic force microscope with a spatial resolution comparable to the 50 nm hole diameters in these nano-meshes to determine the location of vortices when the magnetic field is commensurate with the diameter of the nano-holes.

Appendix 4

Malonic Acid-Grown AAO

A4.1 ABSTRACT

Porous AAO films have been fabricated using malonic acid electrolytes and characterized with transmission electron microscopy (TEM) and scanning electron microscopy (SEM). Previous results within our group have suggested that malonic acid electrolytes can produce porous AAO films with pore diameters and spacings in a size regime (~100 nm diameters and 300 nm spacings) that bridges a gap between the pore dimensions found in AAO films formed in other electrolytes. Towards this end, TEM and SEM were used to determine the dependence of the pore diameters and spacings on the growth conditions and to confirm that malonic acid-grown AAO films follow the same growth mechanism as other AAO films. In addition, a preliminary study was conducted to determine the feasibility of finding appropriate growth conditions for the self-ordering of the pores into a hexagonal close-packed array. Currently, this self-ordering condition has been found in AAO films formed in three different acid

electrolytes (sulfuric, oxalic, and phosphoric acids) [48-50]. This initial study proved inconclusive but suggests that malonic acid-grown films may self-order into a hexagonally close-packed array at higher anodization voltages than presented here. AAO films with these dimensions could have applications for the fabrication of ordered arrays of nanostructures as well as photonic crystal structures, where only light of specific wavelengths are allowed to travel through a given medium.

A4.2 EXPERIMENTAL DETAILS

To start, high purity (99.999%), 0.25 mm thick aluminum foils were degreased in tetrachloroethylene (TCE), acetone, methanol, and DI water, followed by a cleaning step consisting of a 1:10:20:69 mixed solution of hydrofluoric acid (HF), nitric acid (HNO_3), hydrochloric acid (HCl), and water (H_2O) at 25^oC for five minutes. Following the degreasing, the Al foils were annealed under forming gas (80% N_2, 20% H_2) at 550^oC for three hours and then electropolished in a 1:3 mixture of perchloric acid ($HClO_4$) and ethanol (C_2H_5OH) for three minutes at a constant current density of 100 mA/cm^2 and a temperature of 2^oC. After the Al foil pre-treatment, the Al foils were anodized in 10 wt% malonic acid ($C_3H_4O_4$) at 40^oC at voltages ranging between 65 to 105 V for two hours. Anodizations were carried out at 40^oC since anodizations carried out at room temperature or below did not result in appropriate current vs. time curves (e.g. Figure 3.15) that are the hallmark of porous AAO growth. The resulting anodic oxide films were then stripped in a 1:1 solution of 5 wt% phosphoric acid: 1.8wt% chromic acid for 1 hour. Finally, a second anodization was performed on the foils at the same voltages for times between one and two minutes. Finally, for comparison, a well-ordered AAO film was grown

utilizing a two-step anodization at 40 V in 0.3M oxalic acid ($C_2H_2O_4$). Table A4.1 summarizes the samples grown.

Sample	Voltage	Electrolyte	Temperature	1st Anodization Time	2nd Anodization Time
OAAO-1	40 V	0.3M Oxalic Acid	5°C	16 hr	5 min.
MAAO-1	65 V	10 wt% Malonic Acid	40°C	2 hr	1 min.
MAAO-2	75 V	10 wt% Malonic Acid	40°C	2 hr	1 min.
MAAO-3	85 V	10 wt% Malonic Acid	40°C	2 hr	1 min.
MAAO-4	95 V	10 wt% Malonic Acid	40°C	2 hr	2 min.
MAAO-5	105 V	10 wt% Malonic Acid	40°C	2 hr	2 min.

Table A4.1. Malonic acid-grown AAO sample growth conditions.

After growth, pieces of each film were prepared for SEM and TEM observation. SEM preparation simply involved mounting the samples on the copper SEM boat with conductive carbon tape. Figure A4.1 shows the TEM sample preparation steps. As described above, the AAO films were anodized on a 0.25 mm thick, high purity (99.995%) Al foil as depicted in Figure A4.1 (a). The second anodization time (between one and two minutes) was carefully chosen to yield a thin film suitable for TEM observation. Next, a polymer layer (collodion in amyl acetate) was spun on the film to give the film some rigidity and to protect the surface during subsequent processing steps, depicted in Figure A4.1 (b). This was followed by etching the Al foil away using a

saturated $HgCl_2$ solution, thereby releasing the anodic oxide film as shown in Figure A4.1 (c). Following this step, the barrier layer was removed in these films by etching in 5 wt% phosphoric acid for 40 minutes as shown in Figure A4.1 (d). Finally, the polymer layer was removed in acetone and the AAO films were lifted off onto a TEM grid as shown in Figure A4.1 (e).

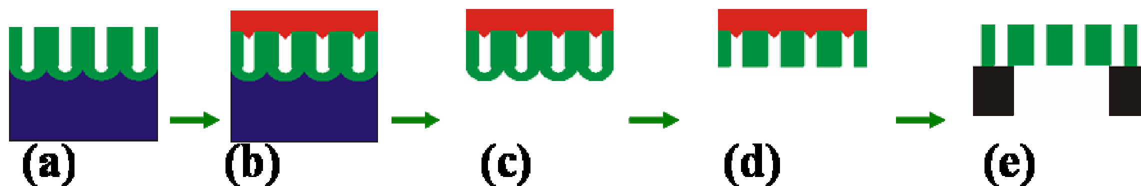

Figure A4.1. (a) AAO film grown on Al foil. (b) Polymer layer spun onto the surface of AAO to protect the top surface from further processing. (c) Al foil etched away to release AAO film. (d) AAO barrier layer etched away to create a through-hole film. (d) Polymer layer removed and AAO film lifted off onto TEM grid.

A4.3 RESULTS

Figure A4.2 shows TEM images of the oxalic acid and malonic acid-grown films. The images confirm that the malonic acid-grown films are porous. Based on the TEM contrast, the oxalic acid-grown film (Figure A4.2 (a)), the 95 V malonic acid-grown film (Figure A4.2 (e)), and the 105 V malonic acid-grown film (Figure A4.2 (f)) appear to be thicker which qualitatively agrees with the 2nd anodization growth times which were larger for these films. Also, except for the oxalic acid-grown film, none of the malonic acid-grown samples appear particularly well-ordered although qualitatively, the higher voltage samples appear to be more ordered than the lower voltage samples.

Figure A4.3 shows SEM images of the oxalic acid and malonic acid-grown films. Similar to the TEM images, the SEM images confirm the films are porous, however, none of the malonic acid-grown films appear to be well-ordered. Again, based on the

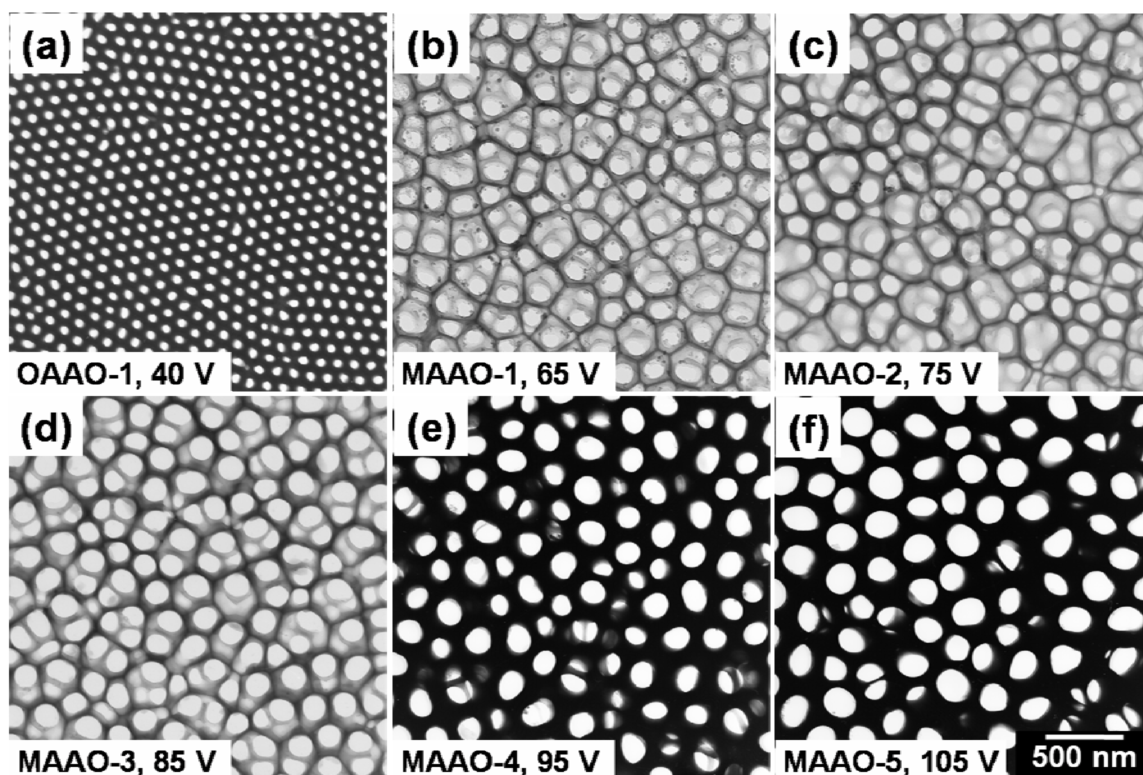

Figure A4.2 TEM images of: (a) 40V oxalic acid-grown AAO film (b) 65 V malonic acid-grown AAO film (c) 75V malonic acid-grown AAO film (d) 85V malonic acid-grown AAO film (e) 95V malonic acid-grown AAO film (f) 105V malonic acid-grown AAO film.

SEM contrast in the dark holes, the oxalic acid-grown film (Figure A4.2 (a)), the 95 V malonic acid-grown film (Figure A4.2 (e)), and the 105 V malonic acid-grown film (Figure A4.2 (f)) appear to be thicker which agrees qualitatively with the longer second anodization times and the TEM images. Finally, both the SEM and TEM images confirm that the average interpore spacings are larger for higher anodization voltages. However, the pore diameters in the SEM images appear smaller than the corresponding films in the TEM images. This is most likely a result of the barrier layer etch done in the TEM preparation (Figure A4.1 (d)) which also served to widen the pores.

Figure A4.4 (a) shows the average inter-pore spacings (error bars are given by the standard deviation) versus the anodization voltage calculated by taking forty measurements from each TEM image. The inter-pore spacings show a linear relationship

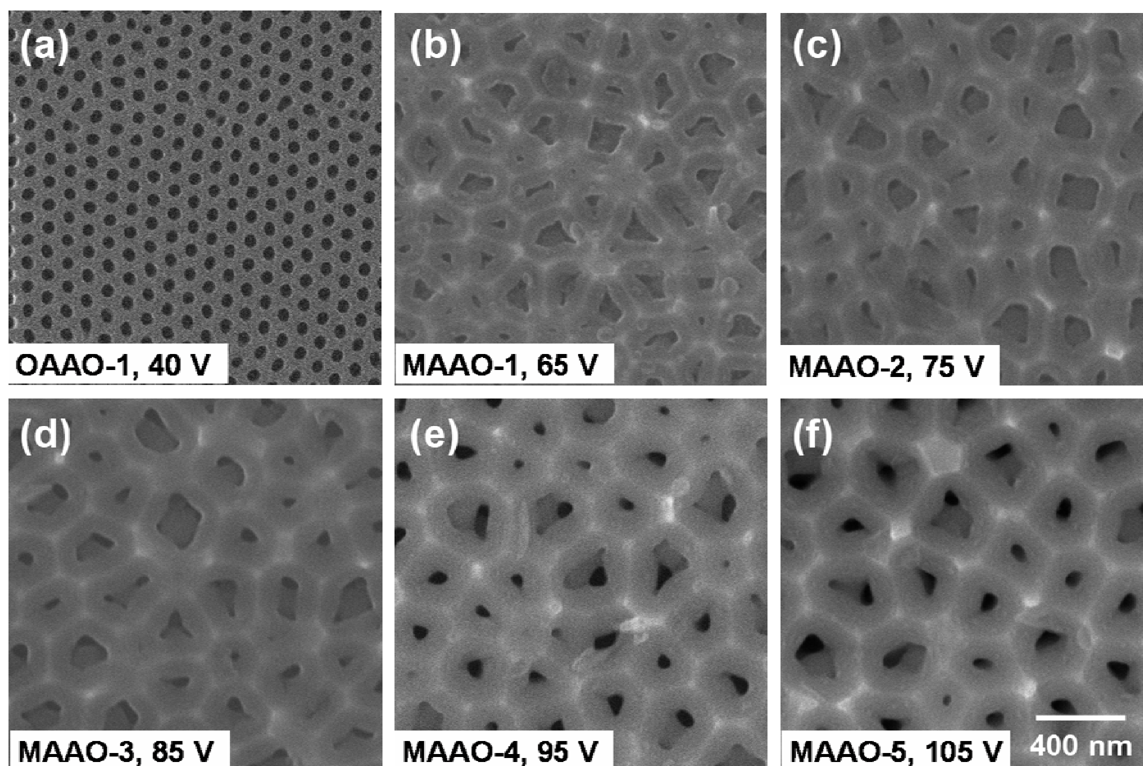

Figure A4.3 SEM images of: (a) 40V oxalic acid-grown AAO film (b) 65 V malonic acid-grown AAO film (c) 75V malonic-acid-grown AAO film (d) 85V malonic acid-grown AAO film (e) 95V malonic acid-grown AAO film (f) 105V malonic acid-grown AAO film.

with the anodization voltage, in good agreement with the relationship established with other AAO films grown in different electrolytes, shown in the straight line fit [52]. Also plotted is the first peak from the radial distribution function corresponding to the first nearest neighbor distance which is discussed below.

Figure A4.4 (b) shows the average pore diameters versus the anodization voltage for both the TEM (blue squares) and SEM (red squares) images calculated by taking twenty measurements each from the TEM and SEM images. The average pore diameters also vary linearly with the applied voltage as shown by the best line fits, although the TEM and SEM values do not agree with each other. Again, this is most likely a result of the barrier layer etch in the TEM preparation (Figure A4.1 (d)) which also served to widen the pores.

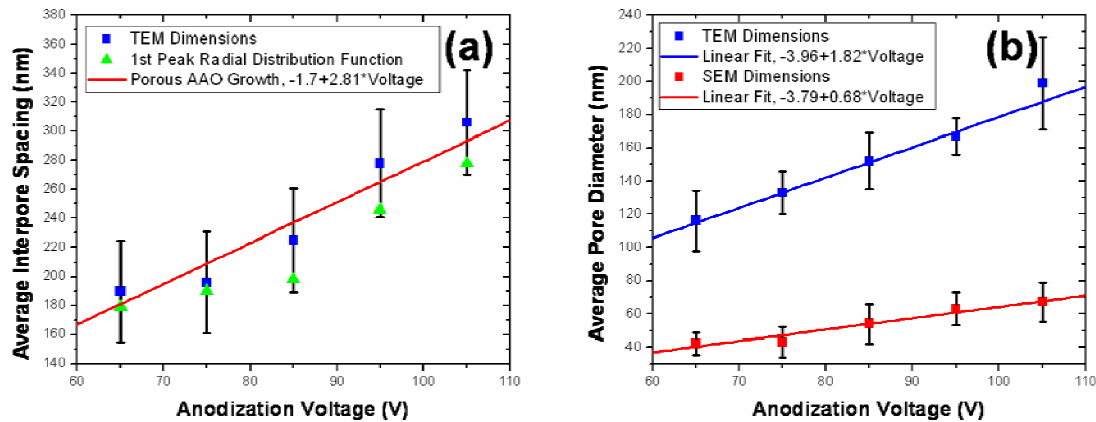

Figure A4.4 (a) Average interpore spacing versus the anodization voltage for the malonic acid-grown films taken from the TEM images. The red line is a best fit line seen in other porous AAO films. Also plotted is the 1st peak in the radial distribution function. (b) Average pore diameters taken from the TEM images (blue squares) and SEM images (red squares) as a function of the anodization voltage. The best line fits are also plotted.

Auto-correlation of the TEM images was used to determine the degree of ordering in the images. Auto-correlation is a useful technique in determining any periodic structures present within an image. In short, the image is overlaid on itself at different positions and the degree of correlation or overlap is determined. Figure A4.5 shows the auto-correlation of the TEM images. As expected, the oxalic acid-grown AAO film shows good ordering as seen by the well-ordered array of bright spots in the auto-correlation image. The malonic acid-grown films show very little ordering although a clear improvement is seen in the auto-correlation images as the anodization voltage increases.

The radial distribution function was also calculated on the TEM images as a means to determine the degree of order present. Given a repeating unit or structure (atoms, molecules, pores, etc.), the radial distribution function gives the probability of finding another structure a given distance away. Figure A4.6 shows the radial distribution function for the TEM images. The oxalic acid-grown film shows many peaks corresponding to the 1st, 2nd, 3rd, etc. nearest neighbor distances. All of the malonic

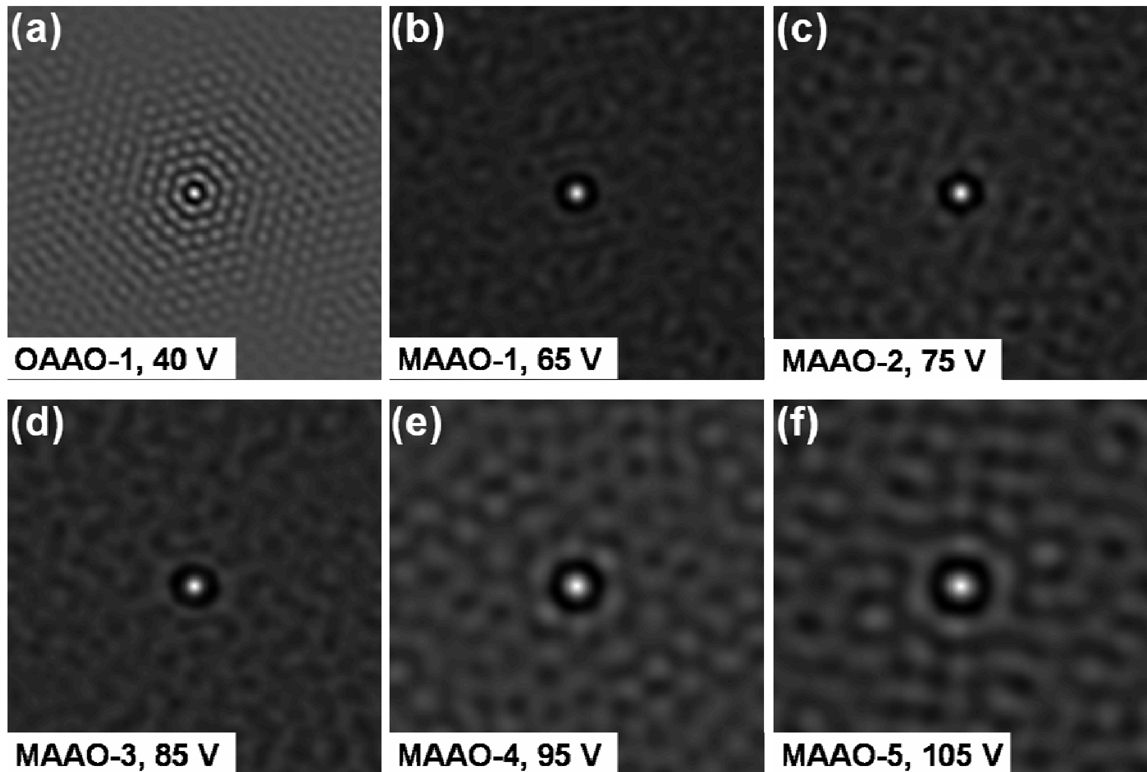

Figure A4.5 Auto-correlation images of: (a) 40V oxalic acid-grown AAO film (b) 65 V malonic acid-grown AAO film (c) 75V malonic acid-grown AAO film (d) 85V malonic acid grown AAO film (e) 95V malonic acid-grown AAO film (f) 105V malonic acid-grown AAO film.

acid-grown films show a small peak indicating the presence of an average nearest neighbor distance. However, starting with the 75V film and becoming more pronounced with the higher voltage films, other peaks can be seen indicating a higher degree of ordering as the voltage increases. Finally, it should also be noted that the 1st nearest neighbor peaks shift to the right as the voltage increases indicating that the inter-pore spacing is increasing.

A4.4 CONCLUSION

Porous malonic acid-grown AAO films were grown with interpore spacings ranging from around 180-300 nm and pore diameters from around 40-200 nm. The

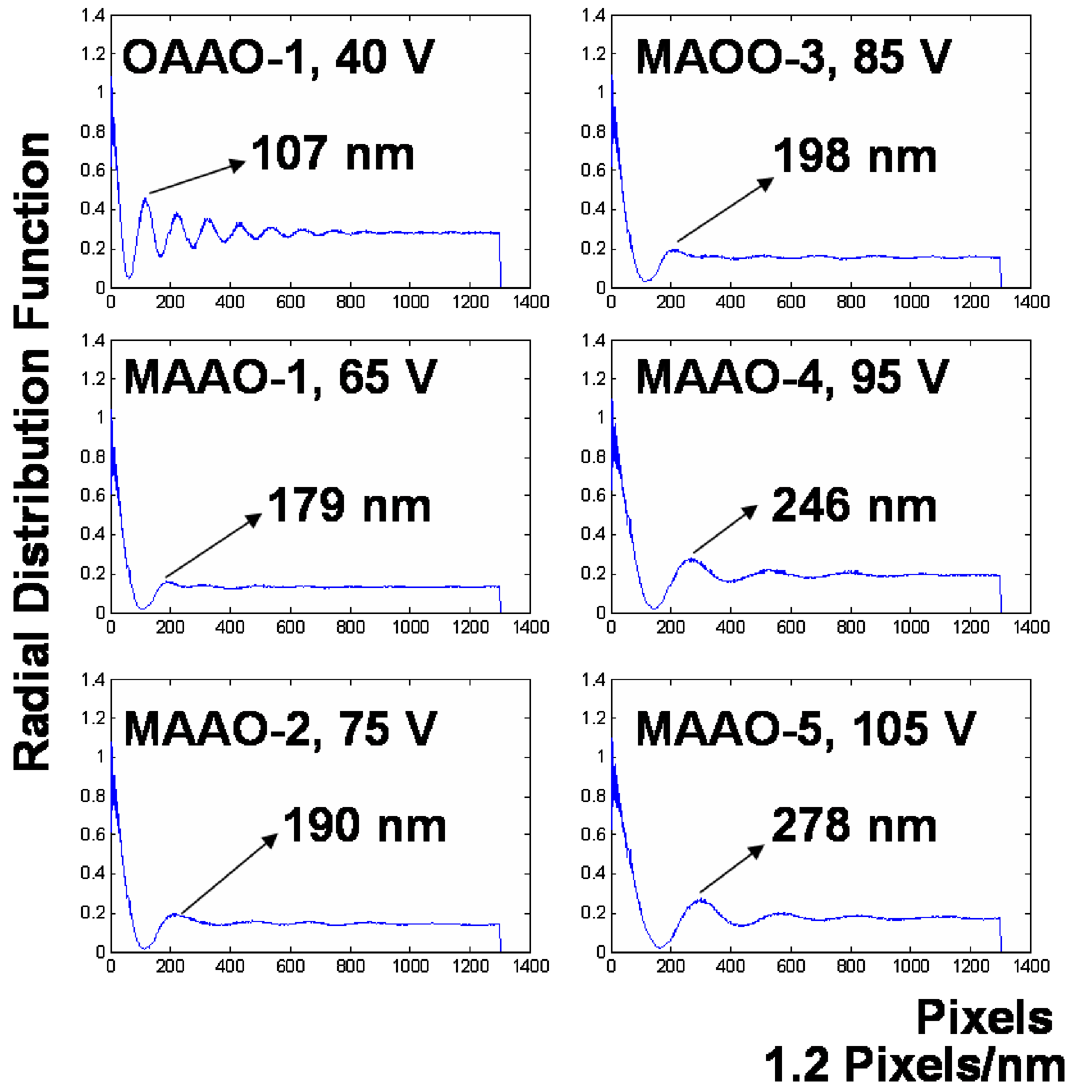

Figure A4.6 Radial distribution function for the oxalic acid-grown AAO film and the malonic acid-grown AAO films.

average inter-pore spacings follow a linear relationship with the anodization voltage. This linear relationship agrees well with the growth mechanisms established for porous AAO films grown in other electrolytes. The pore diameters obtained from SEM images of the films are smaller than the pore diameters obtained from the TEM images, probably due to the barrier layer etch in TEM preparation. Finally, the existence of a self-ordered state in these films is inconclusive but the degree of ordering was observed to be greater

at higher anodization voltages. In conclusion, self-ordering of malonic acid-grown AAO films may be possible at higher anodization voltages than presented here.

Bibliography

[1] R. Feynman's talk at the 1959 annual meeting of the American Physical Society. (http://www.zyvex.com/nanotech/feynman.html)

[2] See for example D. Cox in NSTC Report *Nanostructure Science and Technology*, Eds. R. W. Siegel, E. Hu, and M. C. Roco (Baltimore International Technology Research Institute, World Technology (WTEC) Division, http://www.wtec.org/loyola/nano/, 1999) Chp. 4. Also published by Kluwer Academic Publishers (1999).

[3] L. T. Canham, *Appl. Phys. Lett.* **57**, 1046 (1990).

[4] R. T. Collins, P. M. Fauchet, and M. A. Tischler, *Physics Today* **January**, 24 (1997).

[5] S. Schuppler, S. L. Friedman, M. A. Marcus, D. L. Adler, Y. H. Xie, F. M. Ross, T. D. Harris, W. L. Brown, Y. J. Chabal, L. E. Brus, and P. H. Citrin, *Phys. Rev. Lett.* **72**, 2648 (1994).

[6] M. K. Herndon, R. T. Collins, R. E. Hollingsworth, P. R. Larson, and M. B. Johnson, *Appl. Phys. Lett.* 74, 141 (1999).

[7] C. R. Martin, *Science* **266**, 1961 (1994).

[8] P. R. Larson, K. A. Copeland, G. Dharmasena, R. A. Lasell, M. Keil, and M. B. Johnson, *J. Vac. Sci. Technol. B* **18**, 307 (2000).

[9] R. A. Gottscho, C. W. Jurgensen, and D. J. Vitkavage, *J. Vac. Sci. Technol.* B **10**, 2133 (1992).

[10] T. Nozawa, T. Kinoshita, T. Nishizuka, A. Narai, T. Inoue, and A. Nakaue, *Jpn. J. Appl. Phys.* **34**, 2107 (1995).

[11] G. Dharmasena, K. Copeland, J. H. Young, R. A. Lasell, T. R. Phillips, G. A. Parker, and M. Keil, *J. Phys. Chem. A* **101**, 6429 (1997); M. Keil, J. H. Young, and K. Copeland, "Method and Apparatus for Etching Surfaces with Atomic Fluorine" *U. S. Patent #5,597,495*.

[12] M. Faubel, B. Martinez-Haya, L.Y. Rusin, U. Tuppe, and J. P. Toennies, *J. Phys. D: Appl. Phys.* **29**, 1885 (1996).

[13] K. P. Giapis, T. A. Moore, and T. K. Minton, *J. Vac. Sci. Technol. A* **13**, 959 (1995).

[14] R. J. Levis, C. J. Waltman, L. M. Cousins, R. G. Copeland, and S. R. Leone, *J. Vac. Sci. Tech. A*, 3118 (1990).

[15] A. Szabo, P. D. Farrall, and T. Engel, *J. Appl. Phys.*, 3623 (1994).

[16] M. Faubel, B. Martinez-Haya, L. Y. Rusin, U. Tappe, and J.P. Toennies, *J. Phys. Chem. A* **101**, 6415 (1997).

[17] J.F. O'Hanlon, in *A Users Guide to Vacuum Technology*, 2nd ed., (John Wiley & Sons, New York, 1989) p. 466.

[18] The Si samples were run longer than the Si_3N_4 and SiO_2 because the latter were only available as thin films.

[19] D. L. Flamm, V. M. Donnelly, and J. A. Mucha, *J. Appl. Phys.* **52**, 3633 (1981).

[20] R. Petri, P. Brault, O. Vatel, D. Henry, E. Andre, P Dumas, and F. Salvan, *J. Appl. Phys.* **75**, 7498 (1994).

[21] M. J. M. Vugts, M. F. A. Eurlings, L. J. F. Hermans, and H. C. W. Beijerinck, *J. Vac. Sci. Technol. A* **14**, 2780 (1996).

[22] Y. Hirose, S. Horng, A. Kahn, C. Wrenn, and R. Pfeffer, *J. Vac. Sci. Technol. A* **10**, 960 (1992).

[23] A. G. Nassiopoulos, S. Grigoropoulos, E. Gogolides, and D. Papadimitriou, *Appl. Phys. Lett.* **66**, 1114 (1995).

[24] J. K. Bhardwaj, H. Ashraf, *Proceedings of the SPIE* **2639**, 224 (1995).

[25] Due to the difficulty in measuring beam flux, etching efficiencies for beam techniques have much larger errors (*e.g.*, a factor of 2 for our results) than the data of Flamm *et al*. However, this factor of 2 error is much smaller than the ~10x enhancement observed over the data of Flamm *et al*.

[26] J. W. Coburn and H. F. Winters, *Appl. Phys. Lett.* **55**, 2730 (1989).

[27] G. S. Hwang, C. M. Anderson, M. J. Gordon, T. A. Moore, T. K. Minton, and K. P. Giapis, *Phys. Rev. Lett.* **77**, 3049 (1996).

[28] From Hwang *et al.* deconvolution of their scattering data suggests three distinct scattering processes: 1) direct inelastic scattering with a Gaussian angular distribution about the specular direction, 2) indirect inelastic scattering, and 3) trapping desorption, both with approximately cosine angular distributions.

[29] See for example A. Roth, in *Vacuum Technology*, (Elsevier Science Publishers, New York, 1990) p.80.

[30] *K* is an experimental correction factor that takes into account the asymmetry of the slot. Values of *K,* as a function of *b/a*, can be found in Table 3.5 of Ref. 21. In our work, $a>>b$ and by extrapolation we take $K\approx 2$. The value of Φ_{He} was measured by the method described in the Experimental Results Section.

[31] G. L. Weissler and R. W. Carlson, in *Vacuum Physics and Technology*, Volume 14, (Academic Press, New York, 1979) p.8.

[32] The He-F collision cross-section, $\sigma_{He\text{-}F}$, is determined using, $\sigma_{ij} = \frac{1}{4}\pi(D_i+D_j)^2$, with D_{He} and D_F equal to 2.2 and 3.0 Å, respectively. See Ref. 29 for details.

[33] V. F. Henley, in *Anodic Oxidation of Aluminum and its Alloys*, (Pergamon Press, New York, 1982), p. 1. and p. 51.

[34] J. W. Diggle, T. C. Downie, and C. W. Goulding, *Chem. Rev.* **69**, 365 (1968).

[35] G. C. Wood, in *Oxides and Oxide Films*, Ed. J.W. Diggle (Marcel Dekker Inc., New York, 1973), Vol. 2, p. 167.

[36] G. E. Thompson, *Thin Solid Films* **297**, 192 (1997).

[37] M. J. Dignam, in *Oxides and Oxide Films*, Ed. J. W. Diggle (Marcel Dekker Inc., New York, 1973), Vol. 1, p. 97.

[38] N. Cabrera, and N. F. Mott, *Rept. Prog. Phys.* **12**, 163 (1949).

[39] G. E. Thompson, and G. C. Wood, in *Treatise on Materials Science and Technology*, Ed. J. C. Scully (Academic Press, New York, 1983), Vol. 23, p. 250.

[40] J. P. O'Sullivan, and G. C. Wood, *Proc. Roy. Soc. Lond. A* **317**, 511 (1970).

[41] G. Bailey, and G. C. Wood, *Trans. Inst. Met. Fin.* **52**, 187, (1974).

[42] G. E. Thompson, R. C. Furneaux, J. S. Goode, and G. C. Wood, *Trans. Inst. Met. Fin.* **56**, 159 (1978).

[43] G. E. Thompson, G. C. Wood, and R. Hutchings, *Trans. Inst. Met. Fin.* **58**, 21 (1980).

[44] G. E. Thompson, R. C. Furneaux, G. C. Wood, J. A. Richardson, and J. S. Goode, *Nature* **272**, 433 (1978).

[45] G. E. Thompson, and G. C. Wood, *Nature* **290**, 230 (1981).

[46] K. Shimizu, K. Kobayashi, G. E. Thompson, and G. C. Wood, *Philosophical Magazine A* **66**, 643 (1992).

[47] V. P. Parkhutik and V. I. Shershulsky, *J. Phys. D: Appl. Phys.* **25**, 1258 (1992).

[48] H. Masuda, K. Yada, and A. Osaka, *Jpn. J. Appl. Phys.* **37**, L1340 (1998).

[49] H. Masuda, and K. Fukuda, *Science* **268**, 146 (1995)

[50] H. Masuda, F Hasegwa, and S Ono, *J. Electrochem. Soc.* **144**, L127 (1997).

[51] O. Jessensky, F. Müller, and U. Gösele, *J. Electrochem. Soc.* **145**, 3735 (1998).

[52] A. P. Li, F. Müller, A. Birner, K. Nielsch, and U. Gösele, *J. Appl. Phys.* **84**, 6023 (1998).

[53] A. P. Li, F. Müller, A. Birner, K. Nielsch, and U. Gösele, *J. Vac. Sci. Technol. A* **17**, 1428 (1999).

[54] J. Randon, P. P. Mardilovich, A. N. Govyadinov, and R. Paterson, *J. Coll. Int. Sci.* **169**, 335 (1995).

[55] O. Jessenky, F. Müller, and U. Gösele, *Appl. Phys. Lett.* **72**, 1173 (1998).

[56] K Nielsch, J. Choi, K Schwirn, R. B. Wehrspohn, and U. Gösele, *Nano Lett.* **2**, 677 (2002).

[57] H. Masuda, H. Yamada, M. Satoh, H. Asoh, M. Nakao, and T. Tamamura, *Appl. Phys. Lett.* **71**, 2770 (1997).

[58] H. Asoh, K. Nishio, M. Nakao, T. Tamamura, and H. Masuda, *J. Electrochem. Soc.* **148**, B152 (2001).

[59] H. Masuda, and M. Satoh, *Jpn. J. Appl. Phys.* **35**, L126 (1996).

[60] J. W. Chan, *Masters of Science Thesis*, Graduate Dept. of Chemistry, U. of Toronto (1997).

[61] D. Crouse, Y. Lo, A. E. Miller, and M. Crouse, *Appl. Phys. Lett.* **76**, 49 (2000).

[62] S. Shingubara, O. Okino, Y. Murakami, H. Sakaue, and T. Takahagi, *J. Vac. Sci. Technol. B* **19**, 1901 (2001).

[63] H. Masuda, K. Yasui, Y. Sakamoto, M. Nakao, T. Tamamura, and K. Nishio, *Jpn. J. Appl. Phys.* **40**, L1267 (2001).

[64] G. Frens, *Nat. Phys. Sci.* **241**, 20 (1973).

[65] Commonwealth Scientific Corporation, 500 Pendleton Street, Alexandria, VA, 22314, *Ion Beam Etch Rates and Sputter Yields*, Bulletin #308.

[66] D. Tibbetts and M. Lilly, Sandia National Laboratories, Albuquerque, NM 87185.

[67] T. N. Oder, K. H. Kim, J. Y. Lin, and H. X Jiang, *Appl. Phys. Lett.* **84**, 466 (2004).

[68] J. Shakya, K. H. Kim, J. Y. Lin, and H. X. Jiang, *Appl. Phys. Lett.* **85**, 142 (2004).

[69] M. Curtis, *unpublished.*

[70] H. I. Liu, N. I. Maluf, R. F. W. Pease, D. K. Biegelsen, N. M. Johnson, and F. A. Ponce, *J. Vac. Sci. Technol. B* **10**, 2846 (1992).

[71] H. I. Liu, D. K. Biegelsen, N. M. Johnson, F. A. Ponce, R. F. W. Pease, *J. Vac. Sci. Technol. B* **11**, 2532 (1993).

[72] H. I. Liu, D. K. Biegelsen, F. A. Ponce, N. M. Johnson, and R. F. W. Pease, *Appl. Phys. Lett.* **64**, 1383 (1994).

[73] C. Single, F. Zhou, H. Heidemeyer, F. E. Prins, D. P. Kern, and E. Plies, *J. Vac. Sci. Technol. B* **16**, 3938 (1998).

[74] H Heidemeyer, C. Single, F. Zhou, F. E. Prins, D. P. Kern, and E. Plies, *J. Appl. Phys.* **87**, 4580 (2000).

[75] M. Gotza, M. Dutoit, and M. Llegems, *J. Vac. Sci. Technol. B* **16**, 582 (1998).

[76] K. Nielsch, F. Müller, A. P. Li, and U. Gösele, *Adv. Mater.* **12**, 582 (2000).

[77] M. Saito, M. Kirahara, T. Taniguchi, M. Miyagi, *Appl. Phys. Lett.* **55**, 607 (1989).

[78] X. Mei, D. Kim, H. E. Ruda, and Q. X. Guo, *Appl. Phys. Lett.* **81**, 361 (2002).

[79] H. Masuda, M. Ohya, H. Asoh, M. Nakao, M. Nohtomi, and T. Tamamura, *Jpn. J. Appl. Phys.* **38**, L1403 (1999).

[80] H. Masuda, K. Yasui, Y. Sakamoto, M. Nakao, T. Tamamura, and K. Nishio, *Jpn. J. Appl. Phys.* **40**, L1267 (2001).

[81] Y. Luo, and V. Misra, Department of Electrical and Computer Engineering, North Carolina State University, Raleigh, NC 27695.

[82] Q. Li, G. Mathur, M. Homsi, Shyam, Surthi, V. Misra, V. Malinovski, K. H. Schweikart, L. Yu, J. S. Lindsey, Z. Liu, R. B. Dabke, A. Yasseri, D. F. Bocian, and W. G. Kuhr, *Appl. Phys. Lett.* **81**, 1494 (2002).

[83] K. L. Hobbs, P. R. Larson, G. D. Lian, J. C. Keay, and M. B. Johnson, *NanoLett.* **4**, 167 (2004).

[84] E. M. Q. Jariwala, P. Mohanty, M. B. Ketchen, and R. A. Webb, *Phys. Rev. Lett.* **86,** 1594 (2001).

[85] K. A. Matveev, A. I. Larkin, and L. I. Glazman, *Phys. Rev. Lett.* **89**, 096802 (2002).

[86] J. Aizpurua, P. Hanarp, D. S. Sutherland, M. Käll, W. G. Bryant, and F. J. Garcia de Abajo, *Phys. Rev. Lett.* **90**, 057401 (2003).

[87] A. Lorke, R. J. Luyken, A. O. Govorov, J. P. Kotthaus, J. M. Garcia, and P. M. Petroff, *Phys. Rev. Lett.* **84**, 2223 (2000).

[88] K. Nielsch, R. Hertel, R. B. Wehrspohn, J. Barthel, J. Kirscher, U. Gösele, S. F. Fischer, and H. Kronmüller, *IEEE Trans. Mag.* **38**, 2571 (2002).

[89] S. P. Li, D. Peyrade, M. Natali, A. Lebib, Y. Chen, U. Ebels, L. D. Buda, and K. Ounadjela, *Phys. Rev. Lett.* **86**, 1102 (2001).

[90] J. Zhu, Y. Zheng, and G. Prinz, *J. Appl. Phys.* **87**, 6668 (2000).

[91] D. Huang, and G. Gumbs, *Phys. Rev. B* **46**, 4147 (1992).

[92] B. Roostaei, and K. Mullen, *unpublished.*

[93] L. P. Lévy, G. Dolan, J. Dunsmuir, and H. Bouchiat, *Phys. Rev. Lett.* **64**, 2074 (1990).

[94] M. Winzer, M. Kleiber, N. Dix, and R. Wiesendanger, *Appl. Phys. A* **63**, 617 (1996).

[95] R. Smith, S. S. Makh, and J. M. Walls, *Philosophical Magazine A* **47**, 453 (1983).

[96] Ted Pella Type B carbon 300 TEM grid.

[97] T. Xu, G. Zangari, and R. M. Metzger, *Nano Lett.* **2**, 37 (2002).

[98] K. Nielsch, R. B. Wehrspohn, J. Barthel, J. Kirscner, U. Gösele, S. F. Fischer, and H. Kronmüller, *Appl. Phys. Lett.* **79**, 1360 (2001).

[99] S. P. Murarka in *Silicides for VLSI Applications*, (Academic Press, New York, 1983).

[100] J. Li, C. Papadopoulos, J. M. Xu, and M. Moskovits, *Appl. Phys. Lett.* **75**, 367 (1999).

[101] W. Hu, D. Gong, Z. Chen, L. Yuan, K. Saito, C. A. Grimes, P. Kichambare, *Appl. Phys. Lett.* **79**, 3083 (2001).

[102] J. Wan, Y. H. Luo, S. D. Choi, R. G. Li, G. Jin, J. L. Liu, and K. L. Wang, *J. Appl. Phys.* **89**, 1973 (2001).

[103] M. Yudasaka, R. Kikuchi, T. Matsui, Y. Ohki, S. Yoshimura, and E. Ota, *Appl. Phys Lett.* **67**, 2477 (1995).

[104] C. Bower, O. Zhou, W. Zhu, D. J. Werder, and S. Jin, *Appl. Phys. Lett.* **77**, 2767 (2000).

[105] J. R. Kirtley, M. B. Ketchen, K. G. Stawiasz, J. Z. Sun, W. J. Gallagher, S. H. Blanton, and S. J. Wind, *Appl. Phys. Lett.* **66**, 1138 (1995).